Department of Physics and Astronomy

University of Heidelberg

Master Thesis in Physics

submitted by

Noël Nicolai Cuadra Braatz

born in Germersheim, Germany

2025

Jones-Roberts solitary waves and other phenomena in a Bose-Einstein condensate on the surface of a sphere

This Master Thesis has been carried out by Noël Nicolai Cuadra Braatz

at the

Kirchhoff-Institut für Physik in Heidelberg

under the supervision of

Prof. Thomas Gasenzer

and

Dr. Davide Proment

School of Engineering, Mathematics and Physics, University of East Anglia

Abstract

In this thesis, we study a rotating, two-dimensional Bose gas on the surface of a sphere. Herein, the Gross-Pitaevskii equation in spherical coordinates constitutes the principal equation of investigation. Spectral methods based on the expansion of the wave function in spherical harmonics are introduced and utilized extensively to treat this system. A vortex dipole, which is the minimally allowed topological excitation in this geometry, is initialized by stereographically projecting the phase profile of a dipole in the infinite, flat plane. Its dynamics are investigated using the split-stepping formalism to evolve the Gross-Pitaevskii equation in time which reveals the vortex dipole to be a traveling wave solution. Subsequently, we find stationary solutions for incrementally decreasing, negative external rotation frequency. Eventually, the frequency reaches a critical value where the vortices overlap and annihilate, all vorticity vanishes from the system and only a rarefaction pulse remains. This transition is the primary characteristic of Jones-Roberts solitary waves which we have thus numerically proven to exist on the sphere. They form a continuous family of solutions in the energy-angular momentum plane. Lastly, critical properties such as the dynamics, stability and dispersion of the solitary waves are examined.

Zusammenfassung

In dieser Arbeit untersuchen wir ein rotierendes, zweidimensionales Bose-Gas auf einer Kugeloberfläche. Dabei stellt die Gross-Pitaevskii-Gleichung in Kugelkoordinaten die primäre zu untersuchende Gleichung dar. Spektrale Methoden basierend auf der Entwicklung der Wellenfunktion in Kugelflächenfunktionen werden eingeführt und umfangreich angewandt, um dieses System zu behandeln. Ein Vortex-Dipol, welcher den minimal erlaubten topologische Defekt in dieser Geometrie darstellt, wird initialisiert durch eine stereographische Projektion des Phasenprofils eines Dipols in der unendlich ausgedehnten, flachen Ebene. Seine Dynamik wird untersucht, indem die Gross-Pitaevskii-Gleichung mithilfe des Split-Stepping-Formalismus in der Zeit entwickelt wird, was aufzeigt, dass es sich bei dem Vortex-Dipol um eine laufende Welle handelt. Anschließend finden wir stationäre Lösungen für schrittweise abnehmende, negative externe Rotationsfrequenzen. Schließlich erreicht die Frequenz einen kritischen Wert, an dem die Vortizes überlappen und annihilieren, die gesamte Vortizität aus dem System verschwindet und nur eine Zone verringerter Dichte verbleibt. Dieser Übergang ist das Hauptmerkmal der solitären Jones-Roberts-Wellen, deren Existenz wir damit auf der Kugel numerisch nachgewiesen haben. Diese bilden eine kontinuierliche Familie von Lösungen in der Energie-Drehimpulsebene. Abschließend werden entscheidende Eigenschaften der solitären Wellen wie Dynamik, Stabilität und Dispersion untersucht.

Contents

List of Figures

List of Tables

Chapter 1

Introduction

When Satyendra Nath Bose penned a letter to Albert Einstein in 1924, enclosing his seminal article “Planck’s Law and the Hypothesis of Light Quanta,” he could not possibly have imagined the size of the ball he was about to get rolling [1]. Even though the existence of Bosons and Fermions was not yet established, Einstein understood the importance of Bose’s findings and followed up with two papers of his own suggesting the possible emergence of condensation [2, 3]. Over a century later, the study of ultracold bosonic gases has seen incredible progress in experiment and theory alike. The first experimental realization of a Bose-Einstein condensate (BEC) with novel laser and evaporative cooling techniques in 1995 was a massive milestone that ushered in a new age of probing a variety of phenomena present in these systems in labs around the world [4, 5]. Presently, the progress in experimental setups allows it to accurately adjust all the various terms of the many-body Hamiltonian: kinetic contributions, external potentials or interactions. It is thus possible to realize a variety of systems with differing parameters [6]. The readily available tunability of BECs has made them a renowned stage for quantum simulations [7, 8].

In this thesis, we will concern ourselves with a relatively novel geometry in the field of ultacold atomic gases: the sphere. Until now, most of the research in dimensions below three discusses infinite, flat geometries or 3D systems that are forced into a quasi-2D/1D regime by trapping potentials. The history of the spherical quantum gas begins in 2001, when the possibility of confinement into “matter-wave bubbles” was first elucidated by the interplay of a static and a radiofrequency magnetic field [9]. These techniques have been refined and nowadays it is possible to create quantum gases occupying thin, hollow, shell-shaped volumes. The primary roadblock for these experiments is gravitational sag which leads to an accumulation of atoms in the bottom of the trap. Various remedies have been suggested and successfully carried out. The Cold Atom Laboratory (CAL) onboard the International Space Station conducts experiments in microgravity and has been able to produce a BEC and quantum bubbles [10, 11, 12]. CAL will be superseded by the Bose-Einstein Condensate and Cold Atom Laboratory (BECCAL) which promises further experimental progress in the field [13]. Furthermore, counteracting gravity has also seen success in drop tower experiments [14], onboard a rocket [15] and on the ground using magnetic bubble traps [16].

The advances in experiment have been accompanied by a sizeable amount of theoretical research. We have a wealth of results concerning the quantum statistics and thermodynamics of spherical quantum gases. First and foremost, the phenomenon of Bose-Einstein condensation and its critical temperature has been discussed extensively [17, 18, 19]. The thermodynamical properties have been studied in Refs. [20, 21]. Additionally, the physics of vortices in shell-shaped BECs has been analyzed in great detail [22, 23]. For further background, please consult the introduction of Ref. [24].

In this work, we will make an effort to contribute to the ongoing research of spherically shaped quantum gases by studying the physics of specific traveling wave solutions of the Gross-Pitaevskii equation describing a BEC on the surface of a sphere.

We begin in Chapter 2 by introducing basic mathematical concepts needed to tackle the spherical geometry. Among other things, we stress the importance of spherical harmonics giving access to spectral methods which greatly facilitate the numerical treatment of the system.

In Chapter 3, we first give a general overview of the theory of Bose-Einstein condensation and then specify it to arrive at the mean-field Hamiltonian for a rotating, spherical BEC. From this, the equation of motion for the wave function of the BEC - the Gross-Piatevskii equation - is derived. Next, we discuss a range of theoretical results, some of which are mentioned above, pertaining to the properties of BECs on the sphere to gain a broader background knowledge.

Chapter 4 covers the basics of the numerical methods used throughout the thesis. Most importantly, a framework for the numerical spherical harmonics expansion based on the sampling theorem by Driscoll and Healy is presented [25]. Additionally, the split-stepping formalism to evolve the spherical Gross-Pitaevskii equation in time is introduced.

Next, we turn to the physics of vortex dipoles in Chapter 5. When it comes to topological defects, a single vortex-antivortex pair is the minimally allowed configuration on the spherical surface which will be the main object of study. First, the procedure to initialize the vortex dipole is established. Then, we collect evidence that the vortex dipole constitutes a traveling wave solution by examining its dynamics. Additionally, we observe the formation of vortex lattices in the ground state of a rotating spherical BEC where the number of dipoles in the lattice depends on the external rotation.

Finally, Chapter 6 deals with the main results of this thesis. The question of existence of a class of dark solitary waves, so-called Jones-Roberts solitary waves, in the spherical Gross-Pitaevskii equation is explored. We start off with the vortex dipole and find stationary solutions for specific vortex separations. A transition to a rarefaction pulse is observed as their angular velocity increases which is the principal identifier of Jones-Roberts solitary waves. Lastly, we examine properties of the solitary waves such as their dynamics and dispersion.

Chapter 2

The Sphere

In the present thesis, a physical system that lives on the surface of a sphere - a curved surface - will be studied. While mathematical methods to understand Bose-Einstein condensation in flat space are well-understood, the spherical geometry, specifically due to its curvature, presents its own, unique challenges. Before jumping into the physics, let us begin by having a look at the underlying mathematical concepts necessary to examine the sphere.

2.1. Geometry

The sphere is the only compact, simply-connected, Riemannian surface of constant positive curvature. It is a two-dimensional surface embedded into three-dimensional space $\mathbb{R}^3$. We will use the standard parametrization whereby the two coordinates are the polar angle $\theta \in [0, \pi]$ and the (periodic) azimuthal angle $\phi \in [0, 2\pi)$. Their relation to the coordinates of $\mathbb{R}^3$ is as follows:

$$\begin{aligned} x &= R \sin\theta \cos\phi \, , \\ y &= R \sin\theta \sin\phi \, , \\ z &= R \cos\phi \, , \end{aligned} \tag{2.1}$$

where R is the (fixed) radius of the sphere. Later on, it will often be useful to express lengths in units of the radius, the sphere thereby becoming a unit sphere $S^2 = \{\vec{x} \in \mathbb{R}^3 \big| |\vec{x}| = 1\}$. Inversely, spherical coordinates can be expressed as

$$\begin{aligned} \theta &= \arccos\left(\frac{z}{R}\right) \, , \\ \phi &= \operatorname{atan2}(y, x) \, , \end{aligned} \tag{2.2}$$

where atan2 is the two-argument arctangent. The metric γ on the sphere is

$$\gamma = \begin{pmatrix} R^2 & 0 \\ 0 & R^2 \sin^2\theta \end{pmatrix} \, , \tag{2.3}$$

from which follows the surface element

$$\sqrt{\det \gamma}\ \mathrm{d}\theta \mathrm{d}\phi = R^2 \sin\theta\ \mathrm{d}\theta\mathrm{d}\phi\,. \tag{2.4}$$

We will introduce here the shorthand

$$\int \mathrm{d}\Omega = \int_0^{2\pi} \mathrm{d}\phi \int_0^{\pi} \mathrm{d}\theta \sin\theta\,, \tag{2.5}$$

where Ω is the solid angle. Finally, the gradient and Laplacian transform as follows:

$$\nabla = \frac{\vec{e}_\theta}{R}\partial_\theta + \frac{\vec{e}_\phi}{R\sin\theta}\partial_\phi\,, \tag{2.6}$$

$$\Delta = \frac{1}{R^2\sin\theta}\partial_\theta(\sin\theta\ \partial_\theta) + \frac{1}{R^2\sin^2\theta}\partial_\phi^2 = \frac{1}{R^2}\Delta_\Omega\,. \tag{2.7}$$

2.2. Spherical harmonics

In spherical geometry, it is useful to employ the help of spherical harmonics $Y_l^m(\theta,\phi)$. These perform a very similar role and have similar properties to plane waves in flat space, where the method of expansion is a Fourier transform. Expansion in spherical harmonics gives access to spectral methods based on the manipulation of expansion coefficients which is an immensely powerful numerical tool. Spherical harmonics are complex-valued functions on the unit sphere S^2, defined as eigenfunctions of the angular Laplacian

$$\Delta_\Omega = \frac{1}{\sin\theta}\partial_\theta(\sin\theta\ \partial_\theta) + \frac{1}{\sin^2\theta}\partial_\phi^2\,. \tag{2.8}$$

From this, their form can be derived as

$$Y_l^m(\theta,\phi) = \sqrt{\frac{2l+1}{4\pi}\frac{(l-m)!}{(l+m)!}}P_l^m(\cos\theta)e^{\mathrm{i}m\phi}\,, \tag{2.9}$$

where l is the spherical harmonics degree and m the spherical harmonics order. These indices take the place of the wave vector $\vec{k}$ related to the plane waves in flat space. In quantum mechanics l is the angular momentum (or azimuthal) quantum number and m the magnetic quantum number. The associated Legendre Polynomials $P_l^m(x)$ are defined as follows:

$$P_l^m(x) = (1-x^2)^{\frac{m}{2}}\frac{d^m P_l(x)}{dx^m}\,, \tag{2.10}$$

and

$$P_l(x) = \frac{1}{2^l l!} \frac{d^l}{dx^l} (x^2 - 1)^l \tag{2.11}$$

are the standard Legendre Polynomials. The spherical harmonics form an orthonormal basis on the unit sphere with

$$\int \mathrm{d}\Omega \; Y_l^m(\theta, \phi) Y_{l'}^{m'*}(\theta, \phi) = \delta_{m,m'} \delta_{l,l'} \,, \tag{2.12}$$

where $\delta_{i,j}$ is the Kronecker-Delta. The completeness relation reads

$$\sum_{l=0}^{\infty} \sum_{m=-l}^{l} Y_l^m(\theta, \phi) Y_l^{m*}(\theta', \phi') = \delta(\cos\theta - \cos\theta') \delta(\phi - \phi') \,, \tag{2.13}$$

with the Dirac delta function $\delta(x)$. It follows that any square-integrable function $f : S^2 \longrightarrow \mathbb{C}$ can be expressed as a series of spherical harmonics:

$$f(\theta, \phi) = \sum_{l=0}^{\infty} \sum_{m=-l}^{l} f_l^m Y_l^m(\theta, \phi) \,. \tag{2.14}$$

From the relations above, one concludes that the spherical harmonics expansion coefficients f_l^m can be calculated via

$$f_l^m = \int d\Omega \; Y_l^{m*}(\theta, \phi) f(\theta, \phi) \,. \tag{2.15}$$

The orthogonality properties of the spherical harmonics suggests a generalization of Parseval's theorem on the sphere. Namely, for two functions $f(\theta, \phi) = \sum_{l,m} f_l^m Y_l^m(\theta, \phi)$ and $g(\theta, \phi) = \sum_{l,m} g_l^m Y_l^m(\theta, \phi)$, the integral of their product is given by

$$\int \mathrm{d}\Omega f(\theta, \phi) g^*(\theta, \phi) = \sum_{l=0}^{\infty} \sum_{m=-l}^{l} f_l^m g_l^{m*} \,. \tag{2.16}$$

This relation will be especially useful to write the conserved quantities in spectral representation. Furthermore, some useful expressions for the spherical harmonics are

$$\begin{aligned}
\int \mathrm{d}\Omega \; Y_l^m(\theta, \phi) &= \sqrt{4\pi} \delta_{m,0} \delta_{l,0} \,, \\
\Delta_\Omega Y_l^m(\theta, \phi) &= -l(l+1) Y_l^m(\theta, \phi) \,, \\
\partial_\phi Y_l^m(\theta, \phi) &= \mathrm{i} m Y_l^m(\theta, \phi) \,.
\end{aligned} \tag{2.17}$$

The derivative with respect to θ takes a slightly more complicated form, but can still be expressed with spherical harmonics.

$$\partial_\theta Y_l^m(\theta,\phi) = \begin{cases} m\cot\theta Y_l^m(\theta,\phi) + \sqrt{(l-m)(l+m+1)}e^{-\mathrm{i}\phi}Y_l^{m+1}(\theta,\phi) & \text{for } m \geq 0\,, \\ -m\cot\theta Y_l^m(\theta,\phi) - \sqrt{(l+m)(l-m+1)}e^{\mathrm{i}\phi}Y_l^{m-1}(\theta,\phi) & \text{for } m < 0\,. \end{cases} \tag{2.18}$$

It is occasionally expedient to break down a product of two spherical harmonics into an expansion of a single spherical harmonic, where the expansion coefficients are then given by the Clebsch-Gordan coefficients $C^{lm}_{l_1m_1l_2m_2}$:

$$Y_{l_1}^{m_1}Y_{l_2}^{m_2} = \sum_{l,m}\sqrt{\frac{(2l_1+1)(2l_2+1)}{4\pi(2l+1)}}C^{l0}_{l_10l_20}C^{lm}_{l_1m_1l_2m_2}Y_l^m\,. \tag{2.19}$$

This is a useful relation to reduce a product of many spherical harmonics into a (sometimes) more manageable expression. It is important to note that the properties of the Clebsch-Gordan coefficients demand that $m = m_1 + m_2$ and $|l_1 - l_2| \leq l \leq l_1 + l_2$, which simplifies the summation somewhat.

2.3. Real spherical harmonics

It is, in principle, possible to expand a purely real function in terms of the standard complex spherical harmonics. However, by doing so, one introduces redundancies in the expansion coefficients. Therefore, it is sometimes computationally advisable to use real spherical harmonics to expand real functions. Similarly to above, any real square-integrable function $f : S^2 \longrightarrow \mathbb{R}$ may be expressed as a series of the real spherical harmonics which are denoted here as $\mathcal{Y}_l^m$:

$$f(\theta,\phi) = \sum_{l=0}^{\infty}\sum_{m=-l}^{l} f_l^m\mathcal{Y}_l^m(\theta,\phi)\,. \tag{2.20}$$

The real spherical harmonics are defined as

$$\mathcal{Y}_l^m(\theta,\phi) = \begin{cases} \sqrt{\frac{(2l+1)(2-\delta_{m,0})}{4\pi}\frac{(l-m)!}{(l+m)!}}P_l^m(\cos\theta)\cos(m\phi) & \text{if } m \geq 0\,, \\ \sqrt{\frac{(2l+1)(2-\delta_{m,0})}{4\pi}\frac{(l+m)!}{(l-m)!}}P_l^{-m}(\cos\theta)\sin(-m\phi) & \text{if } m < 0\,. \end{cases} \tag{2.21}$$

Real spherical harmonics also obey the orthonormality relation

$$\int \mathrm{d}\Omega\ \mathcal{Y}_l^m(\theta,\phi)\mathcal{Y}_{l'}^{m'}(\theta,\phi) = \delta_{m,m'}\delta_{l,l'}\,, \tag{2.22}$$

and the expansion coefficients are computed via

$$f_l^m = \int \mathrm{d}\Omega \, \mathcal{Y}_l^m(\theta,\phi) f(\theta,\phi) \, . \tag{2.23}$$

Real spherical harmonics retain their defining feature of being eigenfunctions of the angular Laplacian. Unfortunately, they are no longer eigenfunctions of ∂_ϕ (compare with (2.17)), which may hinder their numerical applicability in some scenarios.

Chapter 3

The weakly-interacting Bose gas

In the following, the system of interest will be a Bose-Einstein condensate placed on the surface of a sphere. Before going over to the sphere, we will give a general outline of Bose-Einstein condensation itself. We start off by noting that we are dealing with a dilute gas of indistinguishable bosonic particles with mass M. Let $\hat{\Psi}^\dagger(\vec{x})$ be the field operator that creates such a particle and $\hat{\Psi}(\vec{x})$ the field operator that annihilates a particle at the position $\vec{x}$. Since these are Bosons, the field operators must follow the commutation relation

$$[\hat{\Psi}(\vec{x}), \hat{\Psi}^\dagger(\vec{x}')] = \delta(\vec{x} - \vec{x}')\,, \tag{3.1}$$

where $\delta(\vec{x})$ is the Dirac delta function. Creation and annihilation operators commute with themselves for any two arguments $\vec{x}$ and $\vec{x}'$. In addition, let the wave functions of the single-particle states available in the system be denoted by $\Psi_i(\vec{x})$, where the index i signifies the i-th state. Then, the field operator can be expanded as

$$\hat{\Psi}(\vec{x}) = \sum_{i=0}^{\infty} \Psi_i(\vec{x})\hat{a}_i\,. \tag{3.2}$$

Here, $\hat{a}_i$ is the annihilation and $\hat{a}_i^\dagger$ the creation operator for a particle in the state i. Similarly to above, they also follow the bosonic commutation relations

$$[\hat{a}_i, \hat{a}_j^\dagger] = \delta_{i,j} \tag{3.3}$$

and operators commute with themselves for any two states. The occurrence of condensation suggests that the single-particle ground state of the system is macroscopically occupied, meaning that the number of particles in the ground state $N_0 \gg 1$ and for all other states $N_i \ll N_0$. We now introduce the Bogoliubov theory which transforms the field theoretical approach into a mean-field description by the substitution [26]

$$\hat{a}_i, \hat{a}_i^\dagger \longrightarrow \sqrt{N_0}\,. \tag{3.4}$$

Then, the field operator takes the form

$$\hat{\Psi}(\vec{x}) = \sqrt{N_0}\Psi_0(\vec{x}) + \delta\hat{\Psi}(\vec{x})\,, \tag{3.5}$$

with a small perturbation $\delta\hat{\Psi}(\vec{x})$. In a dilute Bose gas at very small temperatures, one may now drop the remaining operator $\delta\hat{\Psi}(\vec{x})$ which represents the non-condensed particles. Then, the field operator is represented by a classical field only. In the following, we will therefore simply replace $\hat{\Psi}(\vec{x})$ by a complex-valued function $\Psi(\vec{x})$ which is then called order parameter or wave function of the condensate. The condensate density is straightforwardly obtained from this as $n(\vec{x}) = |\Psi(\vec{x})|^2$ and we may rewrite the wave function with the Madelung transformation

$$\Psi(\vec{x}) = \sqrt{n(\vec{x})}e^{\mathrm{i}S(\vec{x})}\,, \tag{3.6}$$

where $S(\vec{x})$ is the phase of the condensate. Note that one may always add a constant real number to the phase without impacting the physics which is a consequence of the fundamental gauge symmetry of the system.

Let us now take a step back and look at the weakly-interacting Bose gas. The dilute character of the gas implies that the average distance between particles is much larger than the range of the interaction. It follows that interactions involving more than two particles are exceedingly unlikely. Thus, it is adequate to only consider two-body interactions. The Hamiltonian in terms of the field operators $\hat{\Psi}(\vec{x},t)$ in d dimensions takes the generic form

$$\mathscr{H}(t) = \int \mathrm{d}^d x\ \hat{\Psi}^\dagger(\vec{x},t)\left(-\frac{\hbar^2}{2M}\Delta\right)\hat{\Psi}(\vec{x},t) + \frac{1}{2}\int \mathrm{d}^d x \mathrm{d}^d y\ \hat{\Psi}^\dagger(\vec{y},t)\hat{\Psi}^\dagger(\vec{x},t)V(\vec{y}-\vec{x})\hat{\Psi}(\vec{y},t)\hat{\Psi}(\vec{x},t)\,, \tag{3.7}$$

where the field operators now also change with time. In an ultracold, dilute Bose gases, the de Broglie wavelength of the particles is so large that the details of the two-body potential $V(\vec{y}-\vec{x})$ can no longer be resolved. Only low-energy scattering processes are relevant to the interactions. It is thus sufficient and customary to replace the potential by a contact interaction term $V(\vec{y}-\vec{x}) = g\delta(\vec{y}-\vec{x})$, where the contact interaction strength g is entirely characterized by the s-wave scattering length a. In flat space, g takes the form

$$g = \begin{cases} \frac{4\pi\hbar^2 a}{M} \text{ for } d = 3\,, \\ -\frac{4\pi\hbar^2}{M\ln(na^2)} \text{ for } d = 2\,. \end{cases} \tag{3.8}$$

The mean-field Bogoliubov theory introduced above suggests that the field operators can now be replaced by their classical field counterpart. The Hamilton operator thus becomes a mean-field energy functional of $\Psi(\vec{x}, t)$:

$$\mathscr{H}[\Psi] = \int \mathrm{d}^d x \left\{ \Psi^*(\vec{x}, t) \left(-\frac{\hbar^2}{2M} \Delta \right) \Psi(\vec{x}, t) + \frac{g}{2} |\Psi(\vec{x}, t)|^4 \right\} . \tag{3.9}$$

In order to specify the energy functional for spherical coordinates and to then find the equations of motion in these coordinates, we now examine these aspects in closer detail.

3.1. Gross-Pitaevskii equation in spherical coordinates

There are two approaches to the system at hand. The first one is to consider the full 3D Hamiltonian and add an external potential to it. The potential confines the wave function to a thin spherical shell around the radius R, in effect freezing out any degrees of freedom in radial direction. In the lab, this is the only possibility where the confining potential is usually achieved with the careful interplay of a static magnetic field and a time-dependent magnetic radiofrequency field. In theory, we have the luxury of choosing another option which is what we opt to do. That is to restrict oneself to the spherical geometry only and to profess no knowledge of the three-dimensional world around it, making the problem truly two-dimensional. The wave function is then a function of the angles, θ and ϕ, the Laplacian takes the form of (2.7) and the integral measure becomes

$$\int \mathrm{d}^d x \to \int \mathrm{d}\Omega R^2 . \tag{3.10}$$

In addition to the form of the energy functional in (3.9), it will be a goal to study the BEC under the effects of an external rotation with the frequency $\vec{\omega}$. To achieve that, the term

$$\int \mathrm{d}\Omega R^2 \vec{\omega} \cdot \left(\Psi^* \hat{L} \Psi \right) \tag{3.11}$$

is added to the Hamiltonian. The angular momentum operator is given by $\hat{L} = -\mathrm{i}\hbar(\vec{x} \times \nabla)$. Without loss of generality, one may set the axis of rotation to be the z-axis, i.e. $\vec{\omega} = \omega \vec{e}_z$. It then follows that the only relevant component of the angular momentum is in z direction, which is

$$\hat{L}_z = -\mathrm{i}\hbar(\vec{x} \times \nabla)_z = -\mathrm{i}\hbar(x\partial_y - y\partial_x) = -\mathrm{i}\hbar\partial_\phi \tag{3.12}$$

in spherical coordinates. The Hamiltonian without potential of a rotating BEC on a sphere is then

$$\mathscr{H} = \int \mathrm{d}\Omega R^2 \left\{ \frac{\hbar^2}{2M} |\nabla\Psi|^2 + \frac{g}{2}|\Psi|^4 - \mathrm{i}\hbar\omega\Psi^*\partial_\phi\Psi \right\} . \tag{3.13}$$

After obtaining the final form for the mean-field energy functional, one may now turn to the derivation of the equation of motion which is known as the Gross-Pitaevskii equation [27, 28]. Since we are working in spherical coordinates, it will henceforth be abbreviated as sGPE. The equation is derived via the variational principle, i.e.

$$\mathrm{i}\hbar\partial_t\Psi = \frac{\delta\mathscr{H}}{\delta\Psi^*} . \tag{3.14}$$

With the Hamiltonian (3.13), the sGPE takes the form

$$\begin{aligned} \mathrm{i}\hbar\partial_t\Psi &= -\frac{\hbar^2}{2MR^2}\Delta_\Omega\Psi + g|\Psi|^2\Psi - \mathrm{i}\hbar\omega\partial_\phi\Psi , & (3.15)\\ &= -\frac{\hbar^2}{2MR^2}\left(\frac{1}{\sin\theta}\partial_\theta(\sin\theta\ \partial_\theta\Psi) + \frac{1}{\sin^2\theta}\partial_\phi^2\Psi\right) + g|\Psi|^2\Psi - \mathrm{i}\hbar\omega\partial_\phi\Psi , & (3.16) \end{aligned}$$

in terms of the wave function $\Psi = \Psi(\theta,\phi,t)$. Additionally, one may impose the ansatz $\Psi(\theta,\phi,t) \to \Psi(\theta,\phi,t)e^{-\mathrm{i}\mu t/\hbar}$ with the chemical potential μ. Then, the sGPE is

$$\mathrm{i}\hbar\partial_t\Psi = -\frac{\hbar^2}{2MR^2}\Delta_\Omega\Psi + g|\Psi|^2\Psi - \mathrm{i}\hbar\omega\partial_\phi\Psi - \mu\Psi . \tag{3.17}$$

3.1.1. Non-dimensionalization

In order to numerically treat this system, it is necessary to cast the sGPE in a dimensionless form. In flat space a weakly-interacting Bose gas has one length scale given by the healing length

$$\xi = \sqrt{\frac{\hbar^2}{2\mu M}} . \tag{3.18}$$

On the sphere, we gain an additional length scale by the existence of the radius R which naturally suggests to measure distances in units of this radius. Thus, let us introduce the following relations to render the sGPE dimensionless:

$$t \longrightarrow t\frac{MR^2}{\hbar} , \qquad \Psi \longrightarrow \frac{\Psi}{R} . \tag{3.19}$$

Quantity	Unit	$R = 10\mu$m	$R = 50\mu$m
Length	R	10μm	50μm
Density	$\frac{1}{R^2}$	$0.01\mu\text{m}^{-2}$	$0.0004\mu\text{m}^{-2}$
Time	$\frac{MR^2}{\hbar}$	0.137s	3.42s
Frequency	$\frac{\hbar}{MR^2}$	7.31Hz	0.292Hz
Energy	$\frac{\hbar^2}{MR^2}$	4.81×10^{-15}eV	1.92×10^{-16} eV
Angular Momentum	$\hbar$	$\hbar$	$\hbar$

Table 1: Translation of dimensionless quantities to real units for differing radius.

Inserting this into (3.17) yields

$$\mathrm{i}\partial_t \Psi = -\frac{1}{2}\Delta_\Omega \Psi + \tilde{g}|\Psi|^2\Psi - \mathrm{i}\tilde{\omega}\partial_\phi \Psi - \tilde{\mu}\Psi\,, \tag{3.20}$$

with $\tilde{g} = g\frac{M}{\hbar^2}$, $\tilde{\omega} = \omega\frac{MR^2}{\hbar}$ and $\tilde{\mu} = \mu\frac{MR^2}{\hbar^2}$. We will later return to the discussion of the exact form of g, a result that is known from scattering theory on the sphere. These units are considerably different than the ones usually used in flat 2D. To gain some intuition, let us consider a BEC made out of Rb-87 atoms, i.e. $M = 1.443 \times 10^{-25}$kg, spread over a spherical surface with radius $R = 10\mu$m and $R = 50\mu$m, values that are reasonable in light of recent experiments [11, 12]. Then, the corresponding unit values are given by Table 1.

3.1.2. Conserved quantities

The Gross-Pitaevskii equation conserves a number of quantities. It will be required to evaluate these a number of times throughout the thesis for various reasons and often it is useful to rewrite them in spectral representation. Let

$$\Psi = \sum_{l=0}^{\infty}\sum_{m=-l}^{l} \psi_l^m Y_l^m \tag{3.21}$$

be the wave function of the system in terms of spherical harmonics and expansion coefficients ψ_l^m and the units are as in section 3.1.1. Then, the particle number takes the form

$$N = \int \mathrm{d}\Omega \ |\Psi|^2 = \sum_{l=0}^{\infty} \sum_{m=-l}^{l} |\psi_l^m|^2 \, , \tag{3.22}$$

which follows from Parseval's theorem (2.16). Similarly, the angular momentum in z-direction is

$$L_z = -\mathrm{i} \int \mathrm{d}\Omega \ \Psi^* \partial_\phi \Psi = \sum_{l=0}^{\infty} \sum_{m=-l}^{l} m |\psi_l^m|^2 \, . \tag{3.23}$$

In the present work, we will not encounter a case of rotation around the x- or y-axis, so the other components of the angular momentum vector

$$\begin{aligned} L_x &= \mathrm{i} \int \mathrm{d}\Omega \ \Psi^* (\cos\phi \ \cot\theta \ \partial_\phi + \sin\phi \ \partial_\theta) \Psi \, , \\ L_y &= \mathrm{i} \int \mathrm{d}\Omega \ \Psi^* (\sin\phi \ \cot\theta \ \partial_\phi - \cos\phi \ \partial_\theta) \Psi \end{aligned} \tag{3.24}$$

will be zero. Furthermore, the kinetic and rotational energy are

$$E_{\mathrm{kin}} = -\int \mathrm{d}\Omega \ \frac{1}{2} \Psi^* \Delta_\Omega \Psi = \sum_{l=0}^{\infty} \sum_{m=-l}^{l} \frac{1}{2} l(l+1) |\psi_l^m|^2, \tag{3.25}$$

$$E_{\mathrm{rot}} = -\mathrm{i}\tilde{\omega} \int \mathrm{d}\Omega \ \Psi^* \partial_\phi \Psi = \tilde{\omega} L_z = \tilde{\omega} \sum_{l=0}^{\infty} \sum_{m=-l}^{l} m |\psi_l^m|^2, \tag{3.26}$$

It is not so straightforward to express the interaction energy in a spectral representation in terms of the spherical harmonics expansion coefficients ψ_l^m of the wave function. Suppose instead that the density $n = |\Psi|^2$ is expanded in real spherical harmonics such that $n = \sum_{l,m} n_l^m \mathcal{Y}_l^m$ and likewise $|\Psi|^4 = \sum_{l,m} a_l^m \mathcal{Y}_l^m$. Then, one can write

$$E_{\mathrm{int}} = \frac{\tilde{g}}{2} \int \mathrm{d}\Omega \ |\Psi|^4 = \frac{\tilde{g}}{2} \sum_{l=0}^{\infty} \sum_{m=-l}^{l} (n_l^m)^2 = \sqrt{\pi} \tilde{g} a_0^0. \tag{3.27}$$

3.2. The weakly-interacting Bose gas on the surface of a sphere

To get a better grip on the similarities and differences between flat space and the sphere, we discuss a number of vital properties of the homogeneous Bose gas on the spherical surface in this section. A great deal is known about Bose-Einstein condensation on the surface of a sphere. We owe much of our theoretical insight into this particular geometry to the research of Andrea Tononi and Luca Salasnich in recent years [17, 21, 24, 29]. We will recount here an abridged version of some of their most important findings. For a more detailed understanding of the calculations, please reference the cited publications.

3.2.1. Grand Potential

In equilibrium, the statistical properties of the spherical BEC can be derived from the partition function

$$Z = \int \mathcal{D}\Psi\mathcal{D}\Psi^* e^{-S[\Psi,\Psi^*]/\hbar} . \tag{3.28}$$

The Euclidean action $S[\Psi, \Psi^*]$ takes the form

$$S[\Psi,\Psi^*] = \int_0^{\hbar\beta} \mathrm{d}t \int \mathrm{d}\Omega R^2 \mathcal{L}(\Psi,\Psi^*) = \int_0^{\hbar\beta} \mathrm{d}t \int \mathrm{d}\Omega R^2 \left\{ \Psi^* \left(\hbar\partial_t - \frac{\hbar^2\Delta}{2MR^2} - \mu \right) \Psi + \frac{g}{2}|\Psi|^4 \right\} . \tag{3.29}$$

Here, μ is the chemical potential and $\beta = 1/(k_B T)$. Subsequently, one decomposes the order parameter as $\Psi = \sqrt{n_0} + \delta\Psi$, where n_0 is the condensate density and $\delta\Psi$ represents complex quantum fluctuations on top of it. It is then possible, by discarding the cubic and quartic terms in the Lagrangian $\mathcal{L}$, to transform the partition function into a Gaussian integral which can be solved exactly. From there on, we are interested in the grand potential to access thermodynamical and other vital properties of the condensate:

$$\Phi = -\frac{\ln Z}{\beta} . \tag{3.30}$$

For the sake of brevity, the full calculation will not be illustrated here but instead we will simply give the result. The grand potential as a function of the chemical potential then reads

$$\Phi = -\frac{2\pi R^2\mu^2}{g^2} + \frac{1}{2}\sum_{l=0}^{\infty}\sum_{m=-l}^{l} (E_l - \epsilon_l - \mu) + \frac{1}{\beta}\sum_{l=0}^{\infty}\sum_{m=-l}^{l} \ln\left(1 - e^{-\beta E_l}\right) , \tag{3.31}$$

where $\epsilon_l = \hbar^2 l(l+1)/(2MR^2)$ is the energy of a free condensate and $E_l = \sqrt{\epsilon_l(\epsilon_l + 2\mu)}$ is the Bogoliubov dispersion (see also section 3.2.4). The first term reflects the mean-field result, and the two following terms are beyond mean-field, at zero temperature and finite temperature, respectively. Notably, the zero temperature term may be calculated explicitly and analytically, while the finite temperature terms needs numerical evaluation. Let us further remark that the Bogoliubov approximation employed here is only dependable in low-temperature regimes and where the condensate density is sufficiently high.

3.2.2. Condensate fraction and critical temperature

From the grand potential follows the particle density as

$$n = \frac{1}{4\pi R^2}\frac{\partial \Phi}{\partial \mu}\,, \tag{3.32}$$

with Φ as in (3.31). The aim is to phrase the total particle density as a function of the condensate density n_0 and ultimately find an expression of the condensate fraction n_0/n. A rather lengthy calculation involving variational perturbation theory finds

$$\frac{n_0}{n} = 1 - \frac{Mg}{4\pi\hbar^2} - \frac{1}{4\pi n R^2}\left(1+\sqrt{1+\frac{2MgnR^2}{\hbar^2}}\right) + \frac{M}{2\pi\hbar^2 n\beta}\ln\left[\exp\left(\frac{\hbar^2\beta}{MR^2}\sqrt{1+\frac{2MgnR^2}{\hbar^2}}\right)-1\right]. \tag{3.33}$$

Taking the limit $T \to 0$ of the above result, the condensate fraction at zero temperature is then given by

$$\frac{n_0}{n}(T=0) = 1 - \frac{Mg}{4\pi\hbar^2} - \frac{1}{4\pi n R^2}\left(1-\sqrt{1+\frac{2MgnR^2}{\hbar^2}}\right). \tag{3.34}$$

Sending the radius and the particle number to infinity $N, R \to \infty$, but keeping the density fixed produces $n_0/n = 1 - \frac{Mg}{4\pi\hbar^2}$. This result is equal to what is known for the flat 2D BEC [30] for g as in (3.8) which is a valuable consistency check. These matters are illustrated in Fig. 3.1.

Setting the condensate fraction to zero and rearranging equation (3.33), one finds an implicit but analytic expression for the critical temperature below which condensation occurs:

$$\beta_c = \frac{\frac{\hbar^2\beta_c}{2MR^2}\left(1+\sqrt{1+\frac{2MgnR^2}{\hbar^2}}\right) - \ln\left[\exp\left(\frac{\hbar^2\beta_c}{MR^2}\sqrt{1+\frac{2MgnR^2}{\hbar^2}}\right)-1\right]}{\frac{2\pi\hbar^2 n}{M} - \frac{gn}{2}}\,. \tag{3.35}$$

It must be reiterated that the results presented here are well within Bogoliubov theory and thus may not be reliable outside that regime. Future research could focus on the extension of analytic or numerical methods to generalize these results.

To find the superfluid density as a function of temperature, one may assume a Landau-type formula [31], modified for the specific geometry (detailed derivation in Ref. [21]):

$$n_s = n - \beta\int_1^\infty \mathrm{d}l\,\frac{2l+1}{4\pi R^2}\frac{\hbar^2 l(l+1)}{2MR^2}\frac{e^{\beta E_l}}{(e^{\beta E_l}-1)^2}\,. \tag{3.36}$$

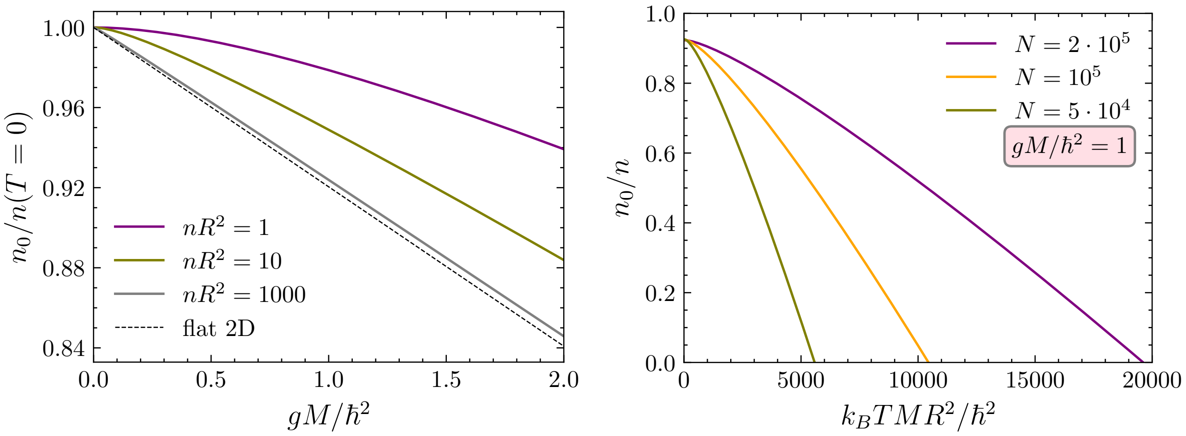

Figure 3.1: The left panel shows the condensate fraction at zero temperature. As the dimensionless parameter nR^2 becomes larger, it approaches the result known from flat 2D. The right panel shows the condensate fraction as a function of temperature for differing values of the particle number N. It follows that $nR^2 = N/(4\pi)$.

Kosterlitz and Nelson found that the quantity $T/n_s(T)$ approaches a universal constant as the transition temperature T_s is approached from below, also known as the Kosterlitz-Nelson criterion [32], or more precisely

$$\lim_{T \nearrow T_s} \frac{T}{n_s(T)} = \frac{\pi\hbar^2}{2Mk_B} \,. \tag{3.37}$$

Making use of this criterion, one can then numerically extract the transition temperature from (3.36). Thereof follows the phase diagram in Fig. 3.2.

There are a few important observations to be made here. Bose-Einstein condensation is a purely quantum statistical phenomenon, whereby the lowest energy state is macroscopically occupied below the critical temperature and can thus occur no matter the value of g. On the other hand, superfluidity is an effect of the collective interaction of the atoms and thus needs a non-zero value of g to exist. Hence, in an exponentially small region around $gM/\hbar^2 \to 0$ T_s drops to zero, while T_c stays finite and takes the value known for the non-interacting Bose gas [17]. For small values of nR^2 (the topmost panel in Fig. 3.2), the phase diagram shows a large area of condensation without superfluidity. This seems to be an immediate effect of the curvature. When nR^2 is small, the gas is either very dilute or the sphere small, which inhibits any kind of collective superfluid behavior. In this regime,

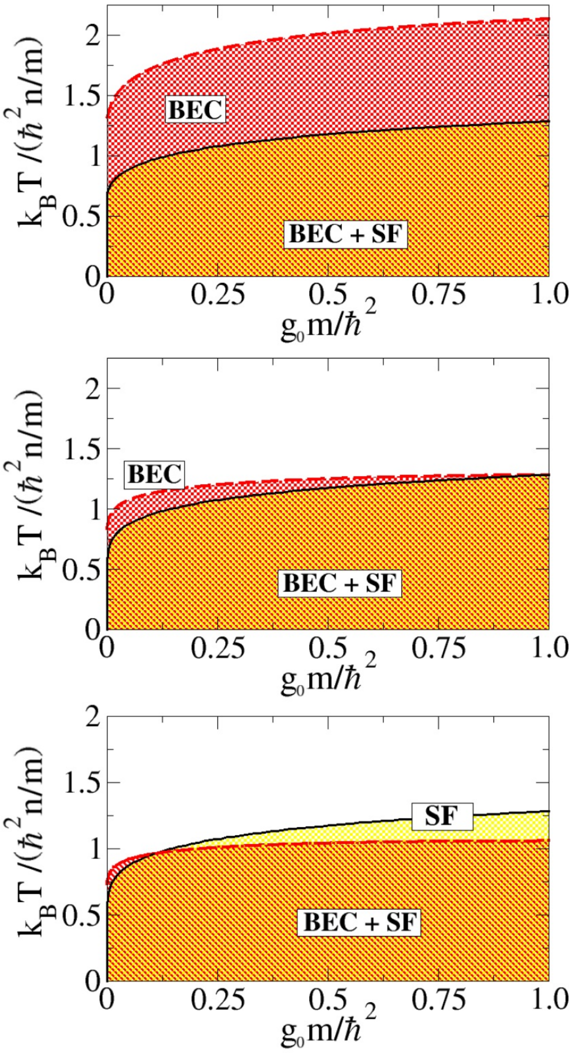

Figure 3.2: The phase diagram of a spherical Bose gas for differing values of the dimensionless parameter nR^2 (Top: $nR^2 = 10^2$, Middle: $nR^2 = 10^4$, Bottom: $nR^2 = 10^5$) as a function of the dimensionless interaction strength $gM/\hbar^2$. g_0 and m in this figure correspond to g and M in the text. The dashed red line shows the transition temperature of the condensation as specified by (3.35). The solid black line represents the transition temperature of superfluidity. The system shows both a mixed phase of BEC and superfluid coexistence, as well as condensation without superfluidity and superfluidity without condensation. Reused from Ref. [24, Fig. 4]. Copyright (2024) by Elsevier.

the curvature may have a similiar effect on the superfluid transition as applying a specific external potential to a flat 2D Bose gas [33]. After increasing nR^2, the phase diagram resembles that of a 2D Bose gas, the transition temperatures of condensation and superfluidity almost coinciding. However, at $nR^2 = 10^5$, one even observes a superfluid region without the presence of a condensate, a phenomenon that requires further reflection and more elaborate analysis. Is it a physical effect or merely a consequence of the deficiencies of the method?

3.2.3. Scattering theory

Turning to scattering theory, the ultimate goal in this context is it to find an expression for the dimensionless contact interaction strength $\tilde{g} = gM/\hbar^2$. In the following calculation, a sphere of radius $R \gg a$ is considered, where a is the s-wave scattering length on the sphere. Furthermore, one may assume the simplification that the wavelengths are much smaller than the radius. It follows that the waves do not "sense" the curvature very strongly, and the calculations are carried out in the near-Euclidean regime. With these restrictions in place, scattering processes give only a perturbative correction to the flat 2D problem. The sphere is parametrized as in Chapter 2, such that $|\theta, \phi\rangle$ is a position vector. The non-interacting scattering states $|l, m\rangle$ are the eigenstates of the free Hamiltonian $\hat{\mathcal{H}}_0 = -\Delta_\Omega$ with eigenvalues $\tilde{\epsilon}_l = l(l+1)$. Both sets $\{|\theta, \phi\rangle\}, \{|l, m\rangle\}$ form a complete, orthonormal eigenbasis on the sphere. Their completeness relations read

$$\begin{aligned} 1 &= \int \mathrm{d}\Omega \, |\theta, \phi\rangle \langle \theta, \phi| \ , \\ 1 &= \sum_{l=0}^{\infty} \sum_{m=-l}^{l} |l, m\rangle \langle l, m| \ . \end{aligned} \tag{3.38}$$

Then, the spherical harmonics are given by

$$Y_l^m(\theta, \phi) = \langle \theta, \phi | l, m\rangle \ . \tag{3.39}$$

Only s-wave scattering is relevant, so $m = 0$ for all scattering states, and a scattering process from l to l' is considered. The contact interaction potential is introduced as $\hat{V} = \tilde{g}\delta(1 - \cos\theta)\delta(\phi)$, where without loss of generality ϕ' and θ' were set to zero. Thus, the potential matrix element for the transition from one scattering state to another takes the form

$$\begin{aligned} V_{l',l} = \langle l',0|\,\hat{V}\,|l,0\rangle &= \int \mathrm{d}\Omega\,\langle l',0|\theta,\phi\rangle\,\tilde{g}\delta(1-\cos\theta)\delta(\phi)\,\langle\theta,\phi|l,0\rangle \\ &= \tilde{g}\frac{\sqrt{(2l'+1)(2l+1)}}{4\pi}\,, \end{aligned} \tag{3.40}$$

where it was used that $Y_l^0(\cos\theta=1,\phi=0)=\sqrt{\frac{2l+1}{4\pi}}$. The full Hamiltonian in the units of section 3.1.1 and with particles of reduced mass $M/2$ then reads

$$\hat{\mathcal{H}} = \hat{\mathcal{H}}_0 + \hat{V} = -\Delta_\Omega + \hat{V}\,. \tag{3.41}$$

Let us now introduce the (unknown) eigenstates of $\hat{\mathcal{H}}$ as $|\Psi_l\rangle$ and the transition operator $\hat{\mathcal{T}}$ as the operator whose action on the free eigenstates $|l,m\rangle$ is equal to action of the potential on the full eigenstates $|\Psi_l\rangle$, i.e. $\hat{\mathcal{T}}\,|l,m\rangle = \hat{V}\,|\Psi_l\rangle$. From this an implicit expression, also known as a Lippmann-Schwinger equation, can be found for the transition operator:

$$\hat{\mathcal{T}} = \hat{V} + \hat{V}\frac{1}{\tilde{\epsilon}_l + \Delta_\Omega - \mathrm{i}\eta}\hat{\mathcal{T}}\,, \tag{3.42}$$

where η is an infinitesimal parameter to regularize. Next, we turn to the matrix elements of the transition operator $\mathcal{T}_{l',l} = \langle l',0|\hat{\mathcal{T}}|l,0\rangle$, yielding a closed integral equation typical of the Lippmann-Schwinger approach:

$$\mathcal{T}_{l',l} = V_{l',l}\left(1 + \sum_{L=0}^{\infty}\sqrt{\frac{2L+1}{2l+1}}\frac{\mathcal{T}_{L,l}}{\tilde{\epsilon}_l - \tilde{\epsilon}_L + \mathrm{i}\eta}\right)\,. \tag{3.43}$$

To solve this equation iteratively, the whole right hand side is repeatedly inserted into the term $\mathcal{T}_{L,l}$ in summation resulting in the formation of a geometric series which can be evaluated to find

$$\frac{1}{\mathcal{T}_{l',l}} = \frac{1}{V_{l',l}} + \frac{1}{\sqrt{(2l'+1)(2l+1)}}\sum_{L=0}^{\infty}\frac{2L+1}{\tilde{\epsilon}_L - \tilde{\epsilon}_l - \mathrm{i}\eta}\,. \tag{3.44}$$

Similarly to (3.40), the effective interaction strength $\tilde{g}_e$ is now defined as proportional to the transition matrix element $\mathcal{T}_{l',l}$ in the following way:

$$\mathcal{T}_{l',l} = \tilde{g}_e\frac{\sqrt{(2l'+1)(2l+1)}}{4\pi}\,. \tag{3.45}$$

This finally leads to a familiar expression in scattering theory relating the bare interaction strength $\tilde{g}$ and the effective interaction strength $\tilde{g}_e$:

$$\frac{1}{\tilde{g}_e} = \frac{1}{\tilde{g}} + \frac{1}{4\pi}\sum_{L=0}^{\infty}\frac{2L+1}{\tilde{\epsilon}_L - \tilde{\epsilon}_l - \mathrm{i}\eta}\,. \tag{3.46}$$

The sum on the right hand side is replaced by an integral

$$\sum_{L=0}^{\infty} \frac{2L+1}{\tilde{\epsilon}_L - \tilde{\epsilon}_l - \mathrm{i}\eta} \to \int_0^{l_c} \mathrm{d}L \frac{2L+1}{\tilde{\epsilon}_L - \tilde{\epsilon}_l - \mathrm{i}\eta} \,, \tag{3.47}$$

where a cutoff l_c was imposed to avoid a UV divergence. The integral can be solved analytically and an expression for the effective interaction strength is retrieved:

$$\tilde{g}_e = -\frac{2\pi}{-\frac{2\pi}{\tilde{g}} + \frac{1}{2}\ln\left(\frac{\tilde{\epsilon}_l}{\tilde{\epsilon}_{l_c}}\right) - \mathrm{i}\frac{\pi}{2}} \,. \tag{3.48}$$

To find the bare interaction strength $\tilde{g}$ as a function of the cutoff l_c and the s-wave scattering length a, one may use the ansatz

$$f_0(\tilde{\epsilon}_l) = \tilde{g}_e \,, \tag{3.49}$$

where $f_0(\tilde{\epsilon}_l)$ is now the s-wave scattering amplitude which takes the general form

$$f_0(\tilde{\epsilon}_l)) = -\frac{4}{\cot\left(\delta_0(\tilde{\epsilon}_l)\right) - \mathrm{i}} \,. \tag{3.50}$$

The cotangent of the phase shift $\delta_0(\tilde{\epsilon}_l)$ reads [34]

$$\cot\left(\delta_0(\tilde{\epsilon}_l)\right) = -\frac{2}{\pi}\left(Q_l(\cos\theta_0) + B^{-1}\right) \,, \tag{3.51}$$

where $Q_l(x)$ is the Legendre function of the second kind, θ_0 is the angular range of the potential and B^{-1} a constant that depends on the properties of the potential inside the range θ_0. This constant can be fixed by introduction of the scattering length and setting it to $B^{-1} = \ln(\theta_0/\theta_s)$, with scattering angle $\theta_s = a/R$. The large wave vector regime suggests that $l \gg 1$ and for a small potential range $\theta_0 < 1/l$, the Legendre function can be approximated as

$$Q_l(\cos\theta_0) = -\ln\left(\frac{\theta_0 l e^{\gamma_E}}{2}\right) + O(\theta_0, 1/l) \,, \tag{3.52}$$

where γ_E is the Euler-Mascheroni constant. Thus, the scattering amplitude takes the form

$$f_0(\tilde{\epsilon}_l)) = -\frac{2\pi}{\ln\left(\frac{\theta_s l e^{\gamma_E}}{2}\right) - \mathrm{i}\frac{\pi}{2}} \,. \tag{3.53}$$

Finally, putting this result into (3.48), the bare interaction strength reads to leading order in l

$$\tilde{g} = -\frac{2\pi}{\ln\left[\frac{\sqrt{l_c(l_c+1)}e^{\gamma_E}}{2}\frac{a}{R}\right]}\,, \tag{3.54}$$

where it was used that

$$\frac{1}{\ln\left[\alpha l/\left(\sqrt{l(l+1)}\right)\right]} = \frac{1}{\ln\alpha} + O(1/l) \tag{3.55}$$

for $l \gg 1$. The central result of (3.54) is interesting in a number of ways. Firstly, it depends on the UV cutoff l_c, a number that is unknown and, in principle, unknowable, since it derives from the precise shape of the true interaction potential which is not captured by the simplified contact interaction approach. The only thing that is known is that $l_c \gg l$. However, due to the logarithmic scaling of the interaction strength with the system parameters, in the weakly-interacting limit it is not critical to know any factor appearing in the logarithm exactly. Furthermore, the scattering length a in the calculations is the scattering length for the spherical Bose gas which has a different value compared to flat 2D and is currently experimentally inaccessible. Nonetheless, working in the large radius limit, $R \gg \xi = \sqrt{\hbar^2/(2M\mu)}$, justifies to use parameters known from the flat case, once again noting the logarithmic scaling. In the following, we set $a/R = 10^{-4}$ and $l_c = 255$ (an inference from the grid format, compare with section 4.1), which gives

$$\tilde{g} \approx 1.66\,. \tag{3.56}$$

3.2.4. Bogoliubov dispersion and speed of sound

To close out this section, the Bogoliubov dispersion of a rotating spherical Bose gas is calculated. In Bogoliubov theory, an infinitesimal delocalised excitation is placed on top of an otherwise homogeneous background. To treat this problem, units are once again included. First, the condensate is set to be of uniform density with some small Bogoliubov-type excitations and the classical field takes the form

$$\Psi = \sqrt{n_0}e^{-\mathrm{i}\frac{\mu}{\hbar}t} + \epsilon\left[AY_l^m e^{-\mathrm{i}(\frac{\mu}{\hbar}+\omega_l^m)t} + B^*Y_l^{-m}e^{-\mathrm{i}(\frac{\mu}{\hbar}-\omega_l^m)t}\right]\,, \tag{3.57}$$

with $\epsilon \ll 1$. The chemical potential μ is included to satisfy energy conservation upon creation of the two excited modes. To compute the excitation spectrum, this function is plugged into (3.16). On order $O(\epsilon^0)$, the well-known relation

$$\mu = gn_0. \tag{3.58}$$

is found. On order $O(\epsilon^1)$, the terms in the sGPE yield

$$\mathrm{i}\hbar\partial_t\Psi = AY_l^m(\mu + \hbar\omega_l^m)e^{-\mathrm{i}(\frac{\mu}{\hbar}+\omega_l^m)t} + B^*Y_l^{-m}(\mu - \hbar\omega_l^m)e^{-\mathrm{i}(\frac{\mu}{\hbar}-\omega_l^m)t}\,, \tag{3.59}$$

$$-\frac{\hbar^2}{2MR^2}\Delta_\Omega\Psi = \frac{\hbar^2}{2MR^2}l(l+1)\left[AY_l^m e^{-\mathrm{i}(\frac{\mu}{\hbar}+\omega_l^m)t} + B^*Y_l^{-m}e^{-\mathrm{i}(\frac{\mu}{\hbar}-\omega_l^m)t}\right]\,, \tag{3.60}$$

$$\begin{aligned} g|\Psi|^2\Psi = \mu\Big(&A^*(-1)^mY_l^{-m}e^{-\mathrm{i}(\frac{\mu}{\hbar}-\omega_l^m)t} + B(-1)^mY_l^m e^{-\mathrm{i}(\frac{\mu}{\hbar}+\omega_l^m)t} \\ &+ 2AY_l^m e^{-\mathrm{i}(\frac{\mu}{\hbar}+\omega_l^m)t} + 2B^*Y_l^{-m}e^{-\mathrm{i}(\frac{\mu}{\hbar}-\omega_l^m)t}\Big)\,, \end{aligned} \tag{3.61}$$

$$-\mathrm{i}\hbar\omega\partial_\phi\Psi = m\hbar\omega\left(AY_l^m e^{-\mathrm{i}(\frac{\mu}{\hbar}+\omega_l^m)t} - B^*Y_l^{-m}e^{-\mathrm{i}(\frac{\mu}{\hbar}-\omega_l^m)t}\right)\,, \tag{3.62}$$

where it was used that $Y_l^{m*} = (-1)^mY_l^{-m}$. Collecting all terms that are proportional to $Y_l^m e^{-\mathrm{i}(\frac{\mu}{\hbar}+\omega_l^m)t}$ and to $Y_l^{-m}e^{-\mathrm{i}(\frac{\mu}{\hbar}-\omega_l^m)t}$, A and B satisfy the two equations

$$A\omega_l^m = A\left(m\omega + \frac{\hbar}{2MR^2}l(l+1) + \frac{\mu}{\hbar}\right) + B(-1)^m\frac{\mu}{\hbar}\,, \tag{3.63}$$

$$B\omega_l^m = B\left(m\omega - \frac{\hbar}{2MR^2}l(l+1) - \frac{\mu}{\hbar}\right) - A(-1)^m\frac{\mu}{\hbar}\,. \tag{3.64}$$

These are equivalent to the eigenvalue equation

$$\begin{pmatrix} m\omega + \frac{\hbar}{2MR^2}l(l+1) + \frac{\mu}{\hbar} & (-1)^m\frac{\mu}{\hbar} \\ -(-1)^m\frac{\mu}{\hbar} & m\omega - \frac{\hbar}{2MR^2}l(l+1) - \frac{\mu}{\hbar} \end{pmatrix}\begin{pmatrix} A \\ B \end{pmatrix} = \omega_l^m\begin{pmatrix} A \\ B \end{pmatrix}. \tag{3.65}$$

To find the non-trivial eigenfrequencies, the following determinant must be equal to zero:

$$\det\begin{pmatrix} m\omega + \frac{\hbar}{2MR^2}l(l+1) + \frac{\mu}{\hbar} - \omega_l^m & (-1)^m\frac{\mu}{\hbar} \\ -(-1)^m\mu & m\omega - \frac{\hbar}{2MR^2}l(l+1) - \frac{\mu}{\hbar} - \omega_l^m \end{pmatrix} \overset{!}{=} 0. \tag{3.66}$$

This finally results in the expression for the Bogoliubov dispersion:

$$\omega_l^m = m\omega \pm \sqrt{\frac{\hbar}{2MR^2}l(l+1)\left(\frac{\hbar}{2MR^2}l(l+1) + \frac{2\mu}{\hbar}\right)}\,. \tag{3.67}$$

Unsurprisingly, this relation takes the familiar form of $\sqrt{E(E+2\mu)}$, where E is the energy of the free Bose gas. The rotation merely adds a term of linear scaling to it. To cast the dispersion relation into a dimensionless form, we can write $\tilde{\omega}_l^m = \frac{\omega_l^m M R^2}{\hbar}$, $\tilde{\omega} = \frac{\omega M R^2}{\hbar}$, $\tilde{\mu} = \frac{\mu M R^2}{\hbar^2}$ to find

$$\tilde{\omega}_l^m = m\tilde{\omega} \pm \sqrt{\frac{1}{2}l(l+1)\left(\frac{1}{2}l(l+1)+2\tilde{\mu}\right)}\,. \tag{3.68}$$

The eigenvalues of the square of the angular momentum operator $\hat{L}^2$ are given by $\hbar^2 l(l+1)$. By analogy to the linear momentum operator in flat space, the wave number is given by $k_l = \sqrt{l(l+1)}/R$. One can therefore calculate the phase velocity of the Bogoliubov modes:

$$v_p(l) = \frac{|\omega_l^0|}{k_l} = \sqrt{\left(\frac{\hbar}{2MR}\right)^2 l(l+1) + \frac{\mu}{M}}\,. \tag{3.69}$$

From this follows the speed of sound as the minimal phase velocity via

$$v_s = \min_l v_p(l) = \sqrt{\frac{\mu}{M}}\,, \tag{3.70}$$

which is the same as in flat space. The angular speed of sound then reads

$$\omega_s = \frac{v_s}{R} = \sqrt{\frac{\mu}{MR^2}}\,. \tag{3.71}$$

We may therefore also use the following heuristic line of argument. On the equator, the speed of sound v_s and the angular speed of sound are related via (3.71). In the limit of large radii, the value of v_s must eventually approach the result known for the flat plane, that is $v_s = \sqrt{\mu/M}$. For the speed of sound to approach a constant value as R goes to infinity, ω_s must go to zero as $\omega_s \propto R^{-1}$. This suggests that the speed of sound on the equator is constant and equal to the flat case, so one can write for the large-radius limit

$$\omega_s \overset{R\to\infty}{=} \sqrt{\frac{\mu}{MR^2}}, \tag{3.72}$$

which means that the expression above reproduces the large radius limit and, in fact, coincides with it. Finally, in dimensionless form, this equation takes the simple form

$$\tilde{\omega}_s = \sqrt{\tilde{\mu}}\,. \tag{3.73}$$

Chapter 4

Numerical methods

In this chapter, the numerical and computational methods to treat the system of a spherical Bose gas, as discussed in the previous chapter, will be introduced. None of this thesis would have been possible without the aid of large-scale, high-performance computer clusters at our disposal. Employment of numerical computations has achieved great success in the understanding of ultracold atomic physics. We follow the footsteps of well-known numerical procedures in flat space and adapt them to the geometry at hand. The code that produced the present thesis was inspired by a previously existing numerical implementation written by Davide Proment but was otherwise created from scratch. It is open source and can be found at `https://github.com/n-cuadra/Master-thesis-on-quantum-vortices-in-spherical-geometry`.

In flat space, the fast Fourier transform (FFT) plays a vital role to be able to efficiently compute the discrete Fourier transform of a data set. The most commonly used FFT algorithm was published by Cooley and Tukey in 1965 and computes the Fourier transform of a data set of length n in $O(n \log n)$ time [35]. As introduced in section 2.2, the spherical harmonics expansion takes the critical role of the Fourier transform on the sphere and all the numerical methods that follow will make extensive use of it.

4.1. Grid and spherical harmonics expansion

The first step to a working numerical implementation of the spherical geometry requires the discretization of its coordinates. To that end, the two angles θ and ϕ that parametrize the sphere are mapped onto an equally spaced $N \times 2N$ grid. Unless otherwise noted, $N = 512$ will be used in the following which is a value that strikes a sensible balance between grid resolution and computation time. It follows then that the angle between two neighboring grid points in both directions is π/N and the angles are discretized as

$$\theta_i = \frac{i\pi}{N} \text{ and } \phi_j = \frac{j\pi}{N}\,, \tag{4.1}$$

where $i \in \{0, 1, \ldots, N-1\}$ and $j \in \{0, 1, \ldots, 2N-1\}$. The wave function Ψ is then formally stored as a 2D array of shape $(N, 2N)$ and the entry with index $[i, j]$ gives the complex number $\Psi(\theta_i, \phi_j)$, i.e. the rows of this array represent constant latitude and the columns constant longitude. Next, let us turn to the computation of the spherical harmonic transform from this discretized wave function.

The algorithm to determine the expansion coefficients is based on the sampling theorem by Driscoll and Healy [25], as implemented in the Python package SHTOOLS [36]. This theorem provides exact quadrature for two types of regular grid formats. First, an equally sampled $N \times N$ grid, where $N = 2^k$ with some natural number k. This means that a function is sampled at N equidistant grid points in both latitudinal and longitudinal direction. However, the distance between two neighboring longitudinal points is twice the distance of two neighboring latitudinal points. The other option is to have an equally spaced $N \times 2N$ grid, where two neighboring points in both directions have the same spacing. As was outlined above, the latter is the grid format employed in this thesis. That is to say, that the grid points correspond to the angles

$$\begin{aligned} \theta &= 0, \frac{\pi}{N}, \frac{2\pi}{N}, \ldots, \frac{(N-1)\pi}{N}\,, \\ \phi &= 0, \frac{\pi}{N}, \frac{2\pi}{N}, \ldots, \frac{(2N-1)\pi}{N}\,. \end{aligned} \tag{4.2}$$

The bands at the south pole ($\theta = \pi$) and at $\phi = 2\pi$ (which is the same as $\phi = 0$) are not required by the transformation routines and are thus not included in the gridded data. These two grid formats are numerically equivalent, except that an equally spaced grid has twice as many data points $n = 2N^2 = 2^{2k+1}$. This kind of sampling means that in terms of distance in real space, the sample points are denser near the poles and one must account for this by properly weighting them. As an example, it follows that the band at the north pole is downweighted to zero and thus has no influence on the computation of the expansion coefficients. Let us now turn to a function $f(\theta, \phi)$ with spherical harmonics expansion coefficients f_l^m. The sampling theorem is exact if the function is band-limited, i.e. $f_l^m = 0$ for $l > l_{\max}$, and the function is sampled such that $N = 2(l_{\max} + 1)$. Next, we can define the necessary sampling weights a_i to be the unique solutions to the equations

$$a_0 P_l(\cos\theta_0) + a_1 P_l(\cos\theta_1) + \ldots + a_{2l_{\max}+1} P_l(\cos\theta_{2l_{\max}+1}) = \sqrt{2}\delta_{l,0}\,, \tag{4.3}$$

for $l = 0, \ldots, 2l_{\max} + 1$, $P_l(x)$ are again the Legendre polynomials (2.11) and the grid points are given as in (4.1). From this follows eventually the closed expression

$$a_i = \frac{2\sqrt{2}}{N} \sin\left(\frac{i\pi}{N}\right) \sum_{l=0}^{l_{\max}} \frac{\sin\left((2l+1)\frac{i\pi}{N}\right)}{2l+1} \,. \tag{4.4}$$

With this knowledge, the sampling theorem for the expansion coefficients f_l^m can be formulated:

$$f_l^m = \frac{\sqrt{2\pi}}{N} \sum_{i=0}^{N-1} \sum_{j=0}^{2N-1} a_i f(\theta_i, \phi_j) Y_l^{m*}(\theta_i, \phi_j) \,. \tag{4.5}$$

At first glance, the two sums seem to suggest that a computation would cost $O(n^2)$ time. However, Driscoll and Healy developed an algorithm that makes use of $O(n \log n)$ FFTs at appropriate waypoints to arrive at an implementation of the sampling theorem that takes $O(n(\log n)^2)$ time. The back transform is simply given by

$$f(\theta_i, \phi_j) = \sum_{l=0}^{l_{\max}} \sum_{m=-l}^{l} f_l^m Y_l^m(\theta_i, \phi_j) \,. \tag{4.6}$$

Unlike the IFFT which is functionally equivalent to the FFT except for a sign and normalization difference, the back transform is a numerically distinct operation and there exists no method to reduce the complexity of the above expression and thus the summation must be carried out naively which gives a computation time of $O(n^{3/2})$.

One interesting consequence of the sampling theorem is that $l_{\max} = N/2 - 1 < N$ which means that total number of expansion coefficients is

$$\sum_{l=0}^{l_{\max}} (2l+1) = \frac{N^2}{4} = \frac{n}{8}. \tag{4.7}$$

The number of degrees of freedom in the space of spherical harmonics is thus eight times smaller than the number of grid points, another peculiarity of the numerical analysis on the sphere. Consider now the wave function Ψ with expansion coefficients ψ_l^m. Typically, Ψ will not be band-limited and so the expansion will not be numerically exact. Nonetheless, the prescription by which the expansion is cut off above $l_{\max} = N/2 - 1$ is still necessary, because the system of equations (4.3) does no longer hold for any larger value of $l_{\max}$. For such a truncation, all areas of the sphere are equally well resolved by the spherical

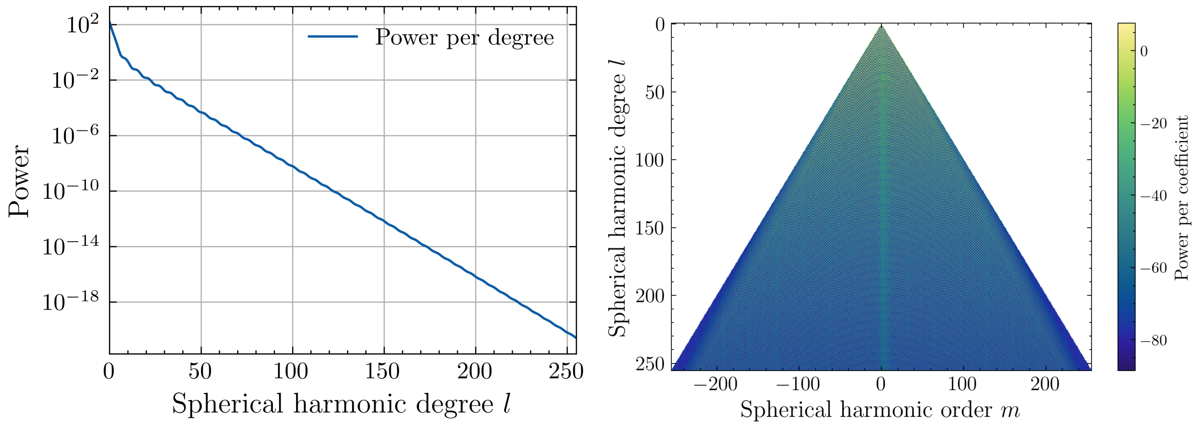

Figure 4.1: Line spectrum and 2D Spectrum of an exemplary wave function of a vortex-antivortex pair situated on the surface of a sphere. The left panel shows the spectrum as in (4.8) in a semilog plot and the spectrum exhibits an exponential decay for $l \gtrsim 20$, where roughly $S_l \propto 10^{-0.08l}$. The right panel shows the 2D spectrum of the same function where the pixel corresponding to the indices l and m is color-coded by the value of $\ln|\psi_l^m|^2$.

harmonics (see chapter 18 of Ref. [37]). One must, however, make sure that the spectrum which is defined by

$$S_l = \sum_{m=-l}^{l} |\psi_l^m|^2 \tag{4.8}$$

decays sufficiently fast, otherwise the cutoff was either too small (and thus the grid cannot resolve the function well enough) or the function may not be represented by a finite expansion. For non-pathological functions, this is usually the case. Throughout the thesis, special care was taken examining the spectra to ensure proper convergence, as exemplified in Fig. 4.1.

With this knowledge, one can now illustrate the computation of the Laplacian and the angular momentum operator as present in the sGPE (3.16). Following the considerations above, the wave function may be written as

$$\Psi(\theta_i, \phi_j) = \sum_{l=0}^{l_{\max}} \sum_{m=-l}^{l} \psi_l^m Y_l^m(\theta_i, \phi_j)\,. \tag{4.9}$$

Since the spherical harmonics are eigenfunctions of Δ_Ω with eigenvalues $-l(l+1)$, the action of the Laplacian on Ψ is

$$\Delta_\Omega \Psi(\theta_i, \phi_j) = \sum_{l=0}^{l_{\max}} \sum_{m=-l}^{l} -l(l+1)\psi_l^m Y_l^m(\theta_i, \phi_j)\,. \tag{4.10}$$

In conclusion, applying the Laplacian onto the wave function is equivalent to the operation

$$\psi_l^m \to -l(l+1)\psi_l^m\,. \tag{4.11}$$

This is very similar to the flat case where the Laplacian simply gives a multiplication with k^2 in Fourier space. Similarly, applying ∂_ϕ to the wave function is identical to

$$\psi_l^m \to \mathrm{i}m\psi_l^m\,. \tag{4.12}$$

These simple results demonstrate the extraordinary power that the spherical harmonic transform brings to the table.

4.2. Split-stepping

In the previous section, the discretization of the spatial coordinates was formulated. A vital part of the numerical treatment of the spherical Bose gas is to solve the dimensionless sGPE (3.20), i.e. to evolve the wave function $\Psi(\theta, \phi, t)$ in time. To that end, the time coordinate is discretized as well, with time steps of length δt. The method of choice for the time propagation of the sGPE is the split-stepping approach, a popular numerical solver for any type of nonlinear Schrödinger equation, known to conserve particle number and energy [38]. To that end, the sGPE is reformulated with the linear operator $\mathscr{L} = -\frac{1}{2}\Delta_\Omega - \mathrm{i}\tilde{\omega}\partial_\phi$ and the nonlinear operator $\mathscr{N} = \tilde{g}|\Psi|^2 - \tilde{\mu}$ (which are both time-independent) as

$$\mathrm{i}\partial_t \Psi = (\mathscr{L} + \mathscr{N})\Psi\,. \tag{4.13}$$

Formally, the solution to this equation for an initial condition $\Psi_0 = \Psi(t_0)$ may be written as

$$\Psi(t_0 + \delta t) = e^{-\mathrm{i}\delta t(\mathscr{L}+\mathscr{N})}\Psi_0\,.$$

Unless $|\Psi|^2$ is constant in time, this expression is only first order accurate. The split-stepping procedure now prescribes that the exponential is split up to generate

$$e^{-\mathrm{i}\delta t(\mathscr{L}+\mathscr{N})} = e^{-\mathrm{i}\delta t\mathscr{L}} e^{-\mathrm{i}\delta t\mathscr{N}} + O(\delta t^2)\,. \tag{4.14}$$

which, by the the Baker-Campbell-Hausdorff formular, produces a second order error. That is to say, the sGPE is split into two parts

$$\mathrm{i}\partial_t \Psi = \mathscr{N}\Psi\,, \quad \mathrm{i}\partial_t \Psi = \mathscr{L}\Psi\,, \tag{4.15}$$

which are solved in sequential order and the solution of the left equation serves as an initial condition for the right equation. This splitting scheme is profoundly helpful since the operator $\mathscr{L}$ is diagonal in the space of spherical harmonics and the operator $\mathscr{N}$ can easily be evaluated on the grid which makes solving the equations (4.15) straightforward. A full, singular time step then takes the following form. First, the action of the nonlinear operator on the initial wave function Ψ_0 produces an intermediate result

$$\bar{\Psi}(\theta_i, \phi_j) = e^{-\mathrm{i}(\tilde{g}|\Psi_0(\theta_i,\phi_j)|^2 - \tilde{\mu})\delta t}\Psi_0(\theta_i, \phi_j) \tag{4.16}$$

for all grid points (θ_i, ϕ_j). Next, the spherical harmonics expansion coefficients $\bar{\psi}_l^m$ of $\bar{\Psi}$ are calculated according to section 4.1. So we can write

$$e^{-\mathrm{i}\delta t\mathscr{L}}\bar{\Psi} = \sum_{l=0}^{l_{\max}} \sum_{m=-l}^{l} \bar{\psi}_l^m e^{-\mathrm{i}\delta t(-\frac{1}{2}\Delta_\Omega - \mathrm{i}\tilde{\omega}\partial_\phi)} Y_l^m$$

Since the spherical harmonics are eigenfunctions of $\mathscr{L}$ and their eigenvalues are as in (2.17), the argument of the exponential simply becomes a complex number involving these eigenvalues. One can then conclude that it suffices to modify the expansion coefficients by

$$\bar{\psi}_l^m \longrightarrow \bar{\psi}_l^{m\prime} = e^{-\mathrm{i}\frac{1}{2}l(l+1)\delta t} e^{-\mathrm{i}m\tilde{\omega}\delta t} \bar{\psi}_l^m\,. \tag{4.17}$$

To complete the time step, we return back to real space with the transform

$$\Psi(t_0 + \delta t) = \sum_{l=0}^{l_{\max}} \sum_{m=-l}^{l} \bar{\psi}_l^{m\prime} Y_l^m\,. \tag{4.18}$$

4.2.1. Imaginary time

It is often helpful to also consider an evolution in imaginary time. This means that the time t is replaced by a purely imaginary number $\tau = \mathrm{i}t$ which is equivalent to replacing $\mathrm{i}\partial_t$ by $-\partial_\tau$ in the sGPE. The time evolution is methodologically exactly identical to what was shown for real time, only iδt changes to $\delta\tau$. That means the nonlinear time step becomes

$$\bar{\Psi}(\theta_i,\phi_j) = e^{-\tilde{g}|\Psi_0(\theta_i,\phi_j)|^2\delta\tau}\Psi_0(\theta_i,\phi_j)\,. \tag{4.19}$$

We do not need to add the chemical potential term here because particle conservation is enforced otherwise (see below). Similarly, the linear time step is modified as

$$\bar{\psi}_l^{m\prime} = e^{-\frac{1}{2}l(l+1)\delta\tau}e^{-m\tilde{\omega}\delta\tau}\bar{\psi}_l^m\,. \tag{4.20}$$

The principal idea behind imaginary time evolution is the following. The equation of motion is transformed into

$$-\partial_\tau\Psi = \mathscr{H}\Psi\,, \tag{4.21}$$

where $\mathscr{H}$ is some (nonlinear, time-independent) quantum-mechanical Hamilton operator. Let now Ψ_n denote its energy eigenstates and ϵ_n their energies. Then, for an initial condition $\Psi_{\text{init}} = \sum_n c_n\Psi_n$ with complex coefficients c_n, the imaginary time evolution takes the form

$$\Psi(\tau) = \sum_n c_n e^{-\epsilon_n\tau}\Psi_n\,. \tag{4.22}$$

Imaginary time evolution thus produces an exponentially decaying superposition of the Hamiltonian eigenstates, where the decay rate is proportional to the energy of the eigenstates. Since the ground state has the lowest energy, it decays the slowest and thus, in the limit of long imaginary time, the evolution will transport the system into its ground state. The only caveat being that the initial condition must contain a contribution by the ground state, i.e. $\Psi_{\text{init}} = c\Psi_{\text{gs}} + ...$, otherwise the imaginary time evolution will converge to the lowest present energy state or some other meta-stable state. Noting the exponential decay, the imaginary time does not conserve particle number on its own. It is thus necessary to externally enforce this condition. This is done by calculating the particle number N for the initial condition and the particle number N' after each time step and then multiplying the wave function by $\sqrt{N/N'}$ to finalize the time step.

Chapter 5

Vortex dipole physics

In section 3.2.4, the form of the dispersion for the Bogoliubov quasiparticles was already established. However, an ultracold Bose gas can, even at zero temperature, exhibit another type of excitation. These are topological in nature and take the form of quantized vortices, which means there is a point in space around which the field rotates, carrying quantized angular momentum. If the order parameter is written as

$$\Psi(\theta, \phi) = \sqrt{n(\theta, \phi)} e^{\mathrm{i}S(\theta,\phi)} \,, \tag{5.1}$$

then the velocity of the condensate takes the form

$$\vec{v}(\theta, \phi) = \frac{\hbar}{m} \nabla S(\theta, \phi) \,, \tag{5.2}$$

where the gradient is as in (2.6). By construction, the velocity is irrotational which is to say that $\nabla \times \vec{v} = 0$. However, the phase field $S(\theta, \phi)$ may still contain topological defects, singular points (the vortex core) where its value is undefined. Since the wave function must be single-valued, the density n must go to zero in the vortex core. One can then write the velocity as $\vec{v} = \vec{v}_{\mathrm{ir}} + \vec{v}_{\mathrm{v}}$, where $\vec{v}_{\mathrm{ir}}$ denotes the completely irrotational part and $\vec{v}_{\mathrm{v}}$ the velocity of the vortices with nonzero curl. Consider now a small region on the surface that contains a single vortex, enclosed by the curve C. If one follows the curve once around the defect the phase can increase by 2π or an integer multiple of it. In other words [39]

$$\oint_C \vec{v}_{\mathrm{v}} \cdot \mathrm{d}\vec{s} = \frac{2\pi q \hbar}{m} \,, \tag{5.3}$$

where $q \in \mathbb{Z}$ is the topological charge or the winding number of the vortex and $\mathrm{d}\vec{s} = R\vec{e}_\theta \mathrm{d}\theta + R \sin\theta \vec{e}_\phi \mathrm{d}\phi$ is the line element on the sphere. In the present thesis, we set out to study the most simple system containing such topological defects. In the flat, infinite plane it is possible to excite a single vortex. On the sphere, however, such an excitation is topologically prohibited. Consider again (5.3), but now with the curve enclosing all vortices, which means the rest of the sphere contains no vortices. It is not possible to distinguish between “inside” and “outside” the path, hence the total charge must be equal on both sides. One can then conclude that the BEC must exhibit charge neutrality due to the compactness of the sphere. If there are N vortices with charges $\{q_i\}$, it holds that

$$\sum_{i=1}^{N} q_i = 0\,. \tag{5.4}$$

Furthermore, a vector field $\vec{v}$ defined on a given surface with Euler characteristic χ is beholden to the Poincaré-Hopf index theorem, whereby

$$\sum_{s} \mathrm{ind}_v(s) = \chi\,. \tag{5.5}$$

Here, s denotes a singular point of the vector field, that is to say a point on the surface where the vector field vanishes or becomes infinite. In flat 2D, the index of the vector field at the point s $\mathrm{ind}_v(s)$ is then given by the amount of times the vector field rotates when traversing a closed path that contains only this one singular point. It is a non-trivial claim that an analogous point on a curved surface has the same index, but it turns out to be true. Then, the theorem states that the sum over indices of all singular points of the vector field (if there is only a finite number of singular points) is equal to the Euler characteristic, a topological invariant describing important properties of the topological space. For the sphere $\chi = 2$ and a singly-charged vortex or antivortex ($q = \pm 1$) has index 1. Hence, the minimally permitted configuration is a vortex-antivortex pair which naturally conforms to the index theorem and the creation of vortices on the sphere happens in these pairs. Such a vortex dipole will be the object of study in the coming sections. Although at first glance a relatively unassuming system, it harbours rich physics which might also give insight into more complicated problems. However, in order to proceed we must first take a quick detour.

5.1. Numerical verification of Bogoliubov dispersion

Before we finally turn to the discussion of topological excitations, it is instructive to look a the Bogoliubov dispersion in some detail within the present numerical apparatus. Bogoliubov modes are, after all, the most basic excitations of the systems and one ought to examine their proper reproduction. Following the ansatz in (3.57), the wave function is initialized as

$$\Psi = \sqrt{n_0} + \epsilon \sum_{l=1}^{l\mathrm{max}} \sum_{m=-l}^{l} Y_l^m \,, \tag{5.6}$$

with $\epsilon \ll 1$. Since $Y_0^0 = 1/\sqrt{4\pi}$, the coefficient ψ_0^0 is accordingly set to $\sqrt{4\pi n_0}$ and all other coefficients are set to ϵ. This wave function is then propagated in time using the split-stepping method outlined in section 4.2 and the expansion coefficients are recorded throughout to find them as a function of time $\psi_l^m(t)$. To now recover the dominant frequencies of the coefficients, it is necessary to perform a Fourier transform. However, the functions $\psi_l^m(t)$ are not necessarily periodic in time. While periodicity is not a strict numerical prerequisite (it is possible to apply an FFT to a non-periodic function), it is expedient to window the coefficients before the Fourier transform. Mathematically speaking, a window function is a function that is non-zero only inside a certain interval, typically symmetric around a maximum in the middle and varying smoothly to zero. When a signal is multiplied with a window function, one therefore retrieves the signal seen "through the window." In practice, the interval of window functions is often chosen to be of same length as the signal, so its purpose is not to window but instead to taper the signal off to zero. Whether the expansion coefficients are periodic or not, due to the arbitrary termination point of the time evolution, their beginning and endpoints are not continuous. These discontinuities appear in the FFT as high-frequency contributions absent in the original function. These frequencies can be higher than the Nyquist frequency and thus get mapped to a lower frequency alias. This phenomenon is known as spectral leakage because frequencies tend to "leak" into the surrounding area. This effect is most pronounced for the peaks of the spectrum and so they get smeared out and broaden. The aim of windowing, then, is to reduce the amount of spectral leakage. In signal processing, it is generally agreed upon that the Hann window (see chapter 3.9 of Ref. [40] for more detail)

$$w(t) = \frac{1}{2}\left[1 - \cos\left(\frac{2\pi t}{T}\right)\right] \tag{5.7}$$

is best suited for signals with unknown content. Here, T is the size of the interval and $0 \leq t \leq T$. For our present purpose, T is chosen to be the length of the time evolution. Then, the windowed coefficients take the form

$$\tilde{\psi}_l^m(t) = \psi_l^m(t) w(t) \,. \tag{5.8}$$

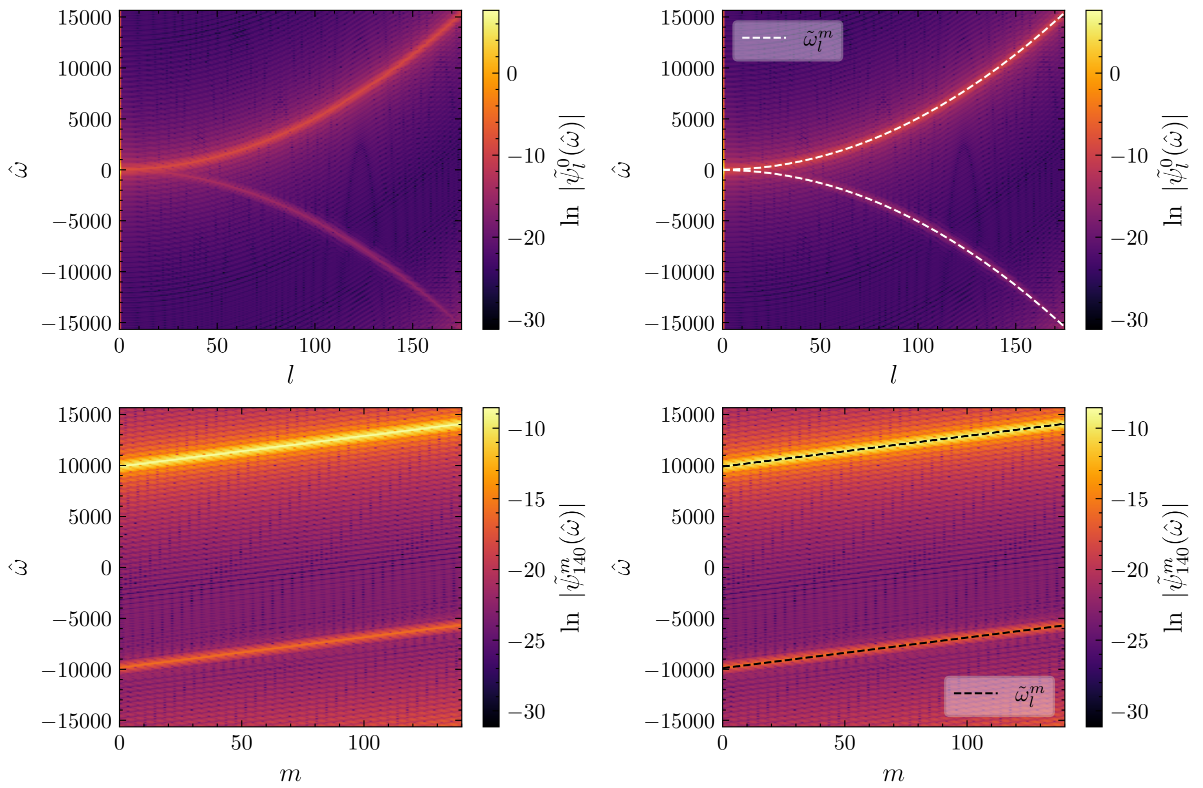

Figure 5.1: Bogoliubov dispersion relation of a spherical Bose gas. The top panels show the spectrum for fixed $m = 0$. The bottom panels show the spectrum for fixed $l = 140$. The two panels on the right also include the analytically known result for the dispersion relation to show that it accurately overlaps with the spectral peaks. To make the spectrum visible, the logarithm of the magnitude of the coefficients $\tilde{\psi}_l^m(\hat{\omega})$ is plotted. The parameters used are $n_0 = 10$, $\epsilon = 10^{-6}$, $\tilde{g} = 1.66$ and $\tilde{\omega} = 30$.

After this procedure is complete, an FFT is performed to find the coefficients $\tilde{\psi}_l^m(\hat{\omega})$ in frequency space, where $\hat{\omega}$ denotes the dimensionless Fourier complement to the time t. Next, one can either set a fixed l or m and plot $\tilde{\psi}_l^m(\hat{\omega})$ as a function of both frequency and the non-fixed index to indeed find that the spectra reproduce the dispersion relation (3.68) as shown in Fig. 5.1. This is an important consistency check which confirms the integrity of the numerical implementation.

5.2. Initial condition

Having understood the Bogoliubov dispersion, the next step is the introduction of vortices into the condensate. The first hurdle to the study of vortex dipoles is to find a method to properly initialize the topological defects. In the flat plane in polar coordinates (r, ϕ), the wave function of a single vortex situated at the origin is simply

$$\Psi = f(r)e^{\mathrm{i}\phi} . \tag{5.9}$$

The transformation rules from polar to Cartesian coordinates tell us that $\phi = \mathrm{atan2}(y, x)$. The phase of two or more vortices may simply be written as the sum of the phases of the single vortex. Therefore, the phase profile of a dipole with the vortex at (x_+, y_+) and the antivortex at (x_-, y_-) is

$$S_{\mathrm{pl}} = \mathrm{atan2}(y - y_+, x - x_+) - \mathrm{atan2}(y - y_-, x - x_-) . \tag{5.10}$$

The next step in the procedure is to map this phase onto the spherical surface the means of which will be the stereographic projection. To this end, the center of the sphere is placed at the origin and the projection is carried out through the North Pole $(0, 0, 1)$ of the sphere, such that the xy-plane, where the dipole (5.10) sits, is perpendicular to the diameter through the North Pole. This leads to the standard form of the stereographic projection:

$$(x, y) = \cot\frac{\theta}{2}(\sin\phi, \cos\phi) , \tag{5.11}$$

with the polar angle θ and the azimuthal angle ϕ. It is then straightforward to insert this transformation into (5.10) to find the general form of the spherical phase

$$\begin{aligned} S = {} & \mathrm{atan2}\left(\cot\frac{\theta}{2}\cos\phi - \cot\frac{\theta_+}{2}\cos\phi_+,\ \cot\frac{\theta}{2}\sin\phi - \cot\frac{\theta_+}{2}\sin\phi_+\right) \\ & - \mathrm{atan2}\left(\cot\frac{\theta}{2}\cos\phi - \cot\frac{\theta_-}{2}\cos\phi_-,\ \cot\frac{\theta}{2}\sin\phi - \cot\frac{\theta_-}{2}\sin\phi_-\right) , \end{aligned} \tag{5.12}$$

where now the positions of the vortex pair are (θ_+, ϕ_+) and (θ_-, ϕ_-). This mapping suggests that a vortex dipole placed on the y-axis is projected onto the antimeridian, a vortex with positive y will end up on the Northern Hemisphere and an antivortex with negative y will end up on the Southern Hemisphere. Translating these considerations into numbers, we have $\phi_+ = \phi_- = \pi$ and $\theta_- = \pi - \theta_+$ with $\theta_+ \in \left[0, \frac{\pi}{2}\right)$. It then follows that

$$\begin{aligned} y_+ &= -\cot\frac{\theta_+}{2}\,, \\ y_- &= -\cot\frac{\theta_-}{2} = -\tan\frac{\theta_+}{2}\,, \\ x_+ &= x_- = 0. \end{aligned} \tag{5.13}$$

With this in mind, the position of the dipole is entirely characterized by θ_+ and the phase then simplifies to

$$S = \operatorname{atan2}\left(\cot\frac{\theta}{2}\cos\phi + \cot\frac{\theta_+}{2},\ \cot\frac{\theta}{2}\sin\phi\right) - \operatorname{atan2}\left(\cot\frac{\theta}{2}\cos\phi + \tan\frac{\theta_+}{2},\ \cot\frac{\theta}{2}\sin\phi\right). \tag{5.14}$$

As dicussed above, the vortex is on the Northern Hemisphere and the anti-vortex on the Southern Hemisphere this way. If the mirrored configuration is desired, the phase can simply be multiplied by -1. In the following, the polar angle of the vortex will always be denoted as θ_+. Note that the stereographic projection is a conformal mapping, i.e. it preserves angles which means that circles on the plane are mapped to circles on the sphere. However, it does not preserve lengths or areas. It is therefore expected that eq. (5.14) has introduced distortions into the phase profile, yet it is not critical to get the phase exactly right. The initial condition proposed here will be subject to a short imaginary time evolution to properly form the vortex cores which will smooth out any distortions. Nonetheless, numerically comparing the phase (5.14) to the phases of several fully stationary solutions of (3.20), the differences were always smaller than 10^{-8} which suggests a remarkable degree of accuracy present in this approach.

In general, the wave function of the condensate can then be written in the following form:

$$\Psi = \sqrt{n_{\mathrm{bg}}} f_\xi e^{\mathrm{i}S}\,, \tag{5.15}$$

with the background density n_{bg} and where f_ξ is a function that is zero at the vortex cores and rises to one on the length scale of the healing length which is given by $\xi = 1/\sqrt{2\bar{n}\tilde{g}}$ in the units of section 3.1.1 and $\bar{n} = N/(4\pi)$ is the average particle density. This function must typically be evaluated numerically. In the flat plane, a popular choice to initalize the density is to employ a Padé approximation of varying order [41]. Whether Padé approximations exist on the sphere is currently unknown, and in any case needs careful consideration due to the compact geometry. It is not vital to imprint the density at all since an imaginary time evolution of the phase will produce the vortex cores one way or the other. In the name of expediency, consider the following model nonetheless. Let us assume the vortex and antivortex are positioned in Cartesian coordinates at

$$\vec{x}_{+/-} = \left(\sin\theta_{+/-}\cos\phi_{+/-}, \sin\theta_{+/-}\sin\phi_{+/-}, \cos\theta_{+/-}\right). \tag{5.16}$$

Then

$$f_\xi = \left(1 - e^{-\ell_+/\xi}\right)\left(1 - e^{-\ell_-/\xi}\right), \tag{5.17}$$

where $\ell_{+/-}$ are the arc lengths separating a point on the sphere

$$\vec{x} = (\sin\theta\cos\phi, \sin\theta\sin\phi, \cos\theta) \tag{5.18}$$

from the vortex or anti-vortex. On the unit sphere, the arc length is simply given by the angle the two vectors enclose:

$$\ell_{+/-} = \sphericalangle(\vec{x}, \vec{x}_{+/-}). \tag{5.19}$$

Since the two vectors form the legs (of length one) and their difference the base of an isosceles triangle, this angle is given by

$$\ell_{+/-} = \sphericalangle(\vec{x}, \vec{x}_{+/-}) = 2\arcsin\left(\frac{|\vec{x} - \vec{x}_{+/-}|}{2}\right). \tag{5.20}$$

Fig. 5.2 shows a wave function initialized with the phase (5.14) after an imaginary time evolution.

5.3. Dynamics

The starting point of this section is Ref. [42]. The authors put a vortex dipole as in (5.14) on the spherical surface which means its position is entirely characterized by the polar angle θ_+ of the vortex on the Northern Hemisphere. Then, its energy is calculated as a function of θ_+ and the external rotation $\tilde{\omega}$ according to the mean-field functional (3.13). They found an energy landscape where the position of the maximum is dependent on $\tilde{\omega}$. Specifically, for a vortex pair where the anti-vortex is on the Northern (Southern) Hemisphere, there is a critical value $\tilde{\omega}_c = 0.5$ ($\tilde{\omega}_c = -0.5$) below (above) which the energy

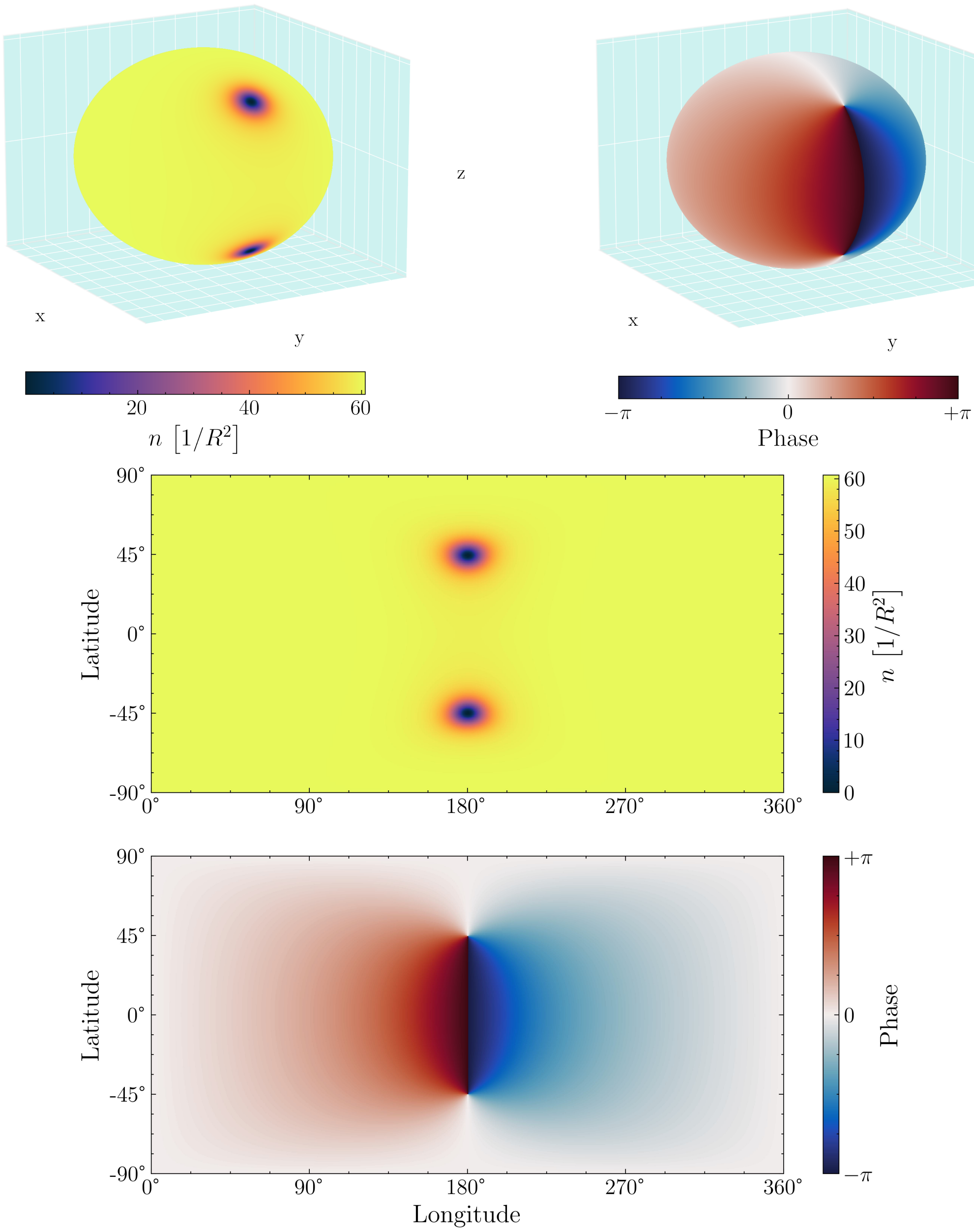

Figure 5.2: Initialized wave function of a vortex dipole for $\theta_+ = 45°$. The particle number was set to be fixed at $N = 750$ and $\tilde{g} = 1.66$. The two panels at the top show the density and the phase of the wave function in a 3D plot, the bottom panel shows them in a 2D plot. Note that the 2D depiction makes the form of the vortex cores slightly distorted (i.e. not circular) since the grid points are denser in terms of distance the closer they are to the poles.

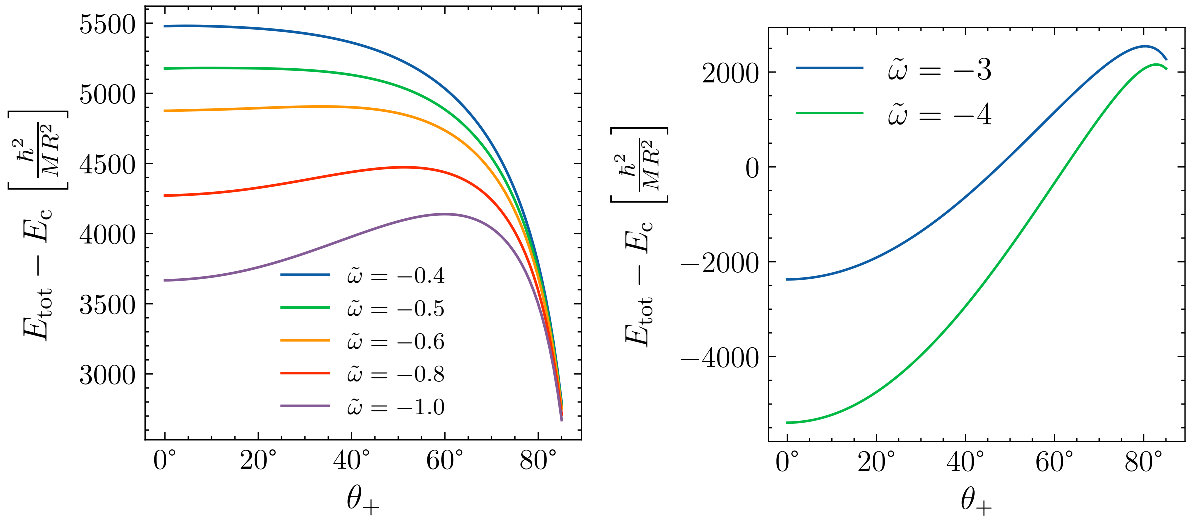

Figure 5.3: Energy of a vortex dipole (vortex on Northern Hemisphere, antivortex on Southern Hemisphere) as function of the position θ_+ for different values of the external rotation $\tilde{\omega}$. E_{tot} is the total energy (3.13) and the energy of the homogeneous condensate with same particle number E_{c} is substracted such that the graph goes to zero as $\theta_+ = 90°$ is approached. The right panel shows that the ground state for a single vortex dipole can be at the poles for a sufficiently large $|\tilde{\omega}|$. Parameters used are $N = 3020$ and $\tilde{g} = 1.66$.

exhibits a global maximum at $\theta_+ = 0$, i.e. the two vortices situated at the poles. Away from the poles, the energy decreases strictly monotonic towards the equator where the two vortices meet and annihilate. Ergo, the ground state of the system is the homogeneous condensate. If one increases (decreases) the external rotation above (below) $\tilde{\omega}_c$, the picture changes. The global minimum at the equator persists at first, but another minimum forms at the poles, and a global maximum sits in between. Since the rotational energy is given by $E_{\mathrm{rot}} = \tilde{\omega} L_z$ and the angular momentum is zero for the homogeneous condensate, one can set the energy for the vortex pole solution to any arbitrary value by modifying $\tilde{\omega}$. It is then possible to create a true ground state at the poles. These matters are illustrated in Fig. 5.3.

One can then argue that it is always energetically favorable for the dipole to relax towards the equator and annihilate when $\tilde{\omega} < \tilde{\omega}_c$ ($\tilde{\omega} > \tilde{\omega}_c$). Thus, there is an attraction between the two vortices in this regime. For $\tilde{\omega} > \tilde{\omega}_c$ ($\tilde{\omega} < \tilde{\omega}_c$), however, it is possible to energetically stabilize the system by placing the vortex pair on the poles. Nevertheless, it is not apparent whether there is an actual mechanism by which the vortices are allowed to either move towards the equator or the poles (depending on the values of $\tilde{\omega}$ and θ_+). In an infinite, flat, two-dimensional BEC, the energy similarly decreases the smaller the distance between the vortices. However, their motion follows the local velocity field of the superfluid which induces a uniform translation rather than decreasing the separation. Furthermore, within the GPE time evolution, there is no dissipation and thus no process through which the vortices can lose energy and move closer together. It is not immediately obvious why this should be any different in spherical geometry. To test this statement, the vortex dipole will be propagated in time and the exact position of the cores determined. To that end, a sophisticated vortex tracking procedure is necessary.

5.3.1. Vortex tracking

To examine the dynamics of moving vortices, it is crucial to have a method to track their movement, that is to detect the position of the vortices on the surface during the time evolution. Since the vortex cores are situated at the roots of the wave function Ψ, we present here a root finding approach based on the Newton-Raphson method which will be able to produce the vortex positions with spectral accuracy, degrees of magnitude more precise than the grid spacing. Let us outline the basic principles of the method. For a simple function $f : \mathbb{R} \longrightarrow \mathbb{R}$ with a root at x_0, the function can be Taylor-expanded

$$0 = f(x_0) = f(x_g) + f'(x_g)(x_0 - x_g) + O\left((x_0 - x_g)^2\right) , \tag{5.21}$$

with a point x_g that is close to x_0. If $x_0 - x_g$ is sufficiently small, then one may truncate the expansion after the linear term and invert to find

$$x_0 = x_g - \frac{f(x_g)}{f'(x_g)} . \tag{5.22}$$

This is the basic idea behind the Newton-Raphson method. One starts out with a guess x_g that must be close to the actual root for the method to converge, then one iteration is performed by computing x_0 via (5.22) and finally x_0 is used as a new guess. This process is repeated until satisfactory convergence is achieved. A great number of algorithms to solve systems of (nonlinear) equations are based on this method. We will see later a much more complicated implementation to find stationary solutions of the sGPE. For the present purpose, it needs to be modified such that it can find the roots of a complex-valued function on the unit sphere. Let us begin by defining

$$\vec{\Psi} = \begin{pmatrix} \Psi_r \\ \Psi_i \end{pmatrix} \tag{5.23}$$

where $\Psi_r = \mathrm{Re}\Psi$ and $\Psi_i = \mathrm{Im}\Psi$ are the real and imaginary part of the wave function. The position of the vortices is then defined by the points where $\vec{\Psi}$ vanishes identically. We will assume that it is possible to find a good inital guess (θ_g, ϕ_g) that is in the vicinity of the actual vortex core position, such that $|\Psi(\theta_g, \phi_g)|^2 < \eta n_{\mathrm{bg}}$ for a sufficiently small number η. Typically, it will be easy to find an initial guess by simply using the points of local minima within the gridded data. If we now denote the actual position of the vortex as (θ_v, ϕ_v), we can Taylor-expand around the initial guess:

$$0 \equiv \vec{\Psi}(\theta_v, \phi_v) = \vec{\Psi}(\theta_g, \phi_g) + \underbrace{\begin{pmatrix} \partial_\theta \Psi_r(\theta_g, \phi_g) & \frac{1}{\sin\theta_g}\partial_\phi \Psi_r(\theta_g, \phi_g) \\ \partial_\theta \Psi_i(\theta_g, \phi_g) & \frac{1}{\sin\theta_g}\partial_\phi \Psi_i(\theta_g, \phi_g) \end{pmatrix}}_{J(\theta_g, \phi_g)} \cdot \begin{pmatrix} \theta_v - \theta_g \\ \phi_v - \phi_g \end{pmatrix} + \dots . \tag{5.24}$$

To find the position of the vortex, this whole structure can now be inverted (assuming that the Jacobian $J(\theta_g, \phi_g)$ is invertible) to find

$$\begin{pmatrix} \theta_v \\ \phi_v \end{pmatrix} = \begin{pmatrix} \theta_g \\ \phi_g \end{pmatrix} - J^{-1}(\theta_g, \phi_g) \cdot \vec{\Psi}(\theta_g, \phi_g) . \tag{5.25}$$

In order to compute the expression above numerically, first the spherical harmonic coefficients are determined via the relation (2.15). With this knowledge, we can then find spectral expressions for $\Psi_r(\theta_g, \phi_g)$ and $\Psi_i(\theta_g, \phi_g)$ by doing a spherical harmonic expansion, i.e.

$$\Psi(\theta_g, \phi_g) = \sum_{l=0}^{l_{\mathrm{max}}} \sum_{m=-l}^{l} \psi_l^m Y_l^m(\theta_g, \phi_g) . \tag{5.26}$$

Note that (θ_g, ϕ_g) need not be a point on the grid. Once the expansion coefficients are calculated, the above expression can be evaluated for any point on the sphere and thus the root can be determined with great precision. Similarly, for the derivatives we then have

$$\partial_\phi \Psi(\theta_g, \phi_g) = \sum_{l=0}^{l_{\max}} \sum_{m=-l}^{l} \mathrm{i}m\psi_l^m Y_l^m(\theta_g, \phi_g) \tag{5.27}$$

$$\partial_\theta \Psi(\theta_g, \phi_g) = \sum_{l=0}^{l_{\max}} \sum_{m=-l}^{l} \psi_l^m \partial_\theta Y_l^m(\theta_g, \phi_g) \tag{5.28}$$

where the derivative with respect to θ is given by (2.18). To get the entries for the Jacobian, one only needs to take the real or imaginary part, e.g. $\partial_\theta \Psi_r(\theta_g, \phi_g) = \mathrm{Re}(\partial_\theta \Psi(\theta_g, \phi_g))$. This procedure can be repeated as many times as necessary by using the new coordinates (θ_v, ϕ_v) as the next initial guess. We then assume that the solution has converged sufficiently well once $|\Psi(\theta_g, \phi_g)|^2 < \epsilon n_{\mathrm{bg}}$ for a small tolerance ϵ. For the initial condition (5.15), it is observed that this algorithm does not converge to the actual - in this case - known positions of the vortices, but it is ever so slightly off in polar direction only. In fact, if the density at the vortex core is calculated via (5.26), one finds that $n(\theta_v, \phi_v) \approx 8 \times 10^{-10} n_{\mathrm{bg}}$, whereas the vortex tracking converges to a point of lower density. One can attribute this numerical inaccuracy to the fact that the spherical harmonic expansion is truncated at $l_{\max}$ by virtue of the finite grid and that information is ultimately lost due to this truncation. It is in principle possible to fix ϵ to the machine precision but considering these matters, we conclude that it is sufficient to set $\epsilon = 10^{-9}$.

5.3.2. Aliasing

Before going over to the discussion of the time evolution itself, it is advisable to spend some time on a common ailment of integrating nonlinear equations of motion: Aliasing instabilities. Aliasing is an effect of the finite truncation of the expansion in basis functions whereby high wavenumbers, which can not be resolved by the grid, are “aliased” to low wavenumbers that can be resolved. This eventually leads to the spectrum blowing up and the simulation crashing. To discuss these matters, let us look at the one-dimensional flat space. It will be straightforwards to extend these concepts to higher dimensions or the spherical case. Suppose that the grid spacing is Δx, the total length of the grid is $2L$ and the grid points are situated at $x \in \{-L, -L + \Delta x, \ldots, 0, \ldots, L - \Delta x, L\}$. It follows that the spacing in Fourier space is $\Delta k = \pi/L$ and the grid points in Fourier space are

$$k \in \{-\pi/\Delta x, -\pi/\Delta x + \Delta k, \ldots, 0, \ldots, \pi/\Delta x - \Delta k, \pi/\Delta x\}\,. \tag{5.29}$$

That is to say there is a maximum wavenumber

$$|k|_{\max} = \frac{\pi}{\Delta x}\,, \tag{5.30}$$

which is also called the aliasing limit wavenumber, and any higher wavenumber can not be represented by the grid anymore. However, it is possible to show that any $|k| > |k|_{\max}$ will be aliased to a wavenumber permissible by (5.29). In practice, this means that a wavenumber $k = |k|_{\max} + j\Delta k$ ($j \in \mathbb{N}$) will appear in the numerics as $|k|_{\max} - j\Delta k$ and $k = -|k|_{\max} - j\Delta k$ will appear as $-|k|_{\max} + j\Delta k$. If j is very large, this "folding back" into the range (5.29) might have to be performed multiple times. One can then state that the truncation of the Fourier expansion introduces two errors. First, an error due to the truncation itself which discards any components with $|k| > |k|_{\max}$. Second, an error of the expansion coefficients because they include contributions from higher wavenumbers due to aliasing and are therefore not identical to those of the exact expansion. This is entirely a consequence of the nonlinearity. The discretization of a linear equation does not lead to aliasing and thus the expansion coefficients will be exact. The first error will stay constant. The second, however, can grow without bounds because continued aliasing will eventually lead to numerical instabilities.

Thankfully, these instabilites are relatively easy to spot. It is sufficient to visually monitor the spectrum because the wavenumbers with $|k|_{\max}$ are the first to be excited by aliasing (see Chapter 11 of Ref. [37]). Consequently, the absolute value of the corresponding expansion coefficients must grow. This leads to a phenomenon called "spectral blocking" which means that the spectrum exhibits a rise in value near the highest wavenumber instead of a uniform exponential decay which would be the non-pathological behavior. This signifies that the high wavenumbers have accumulated a lot of noise due to aliasing and it is a precursor to the complete breakdown of the numerical method. Aliasing is a secular effect, meaning that it gets worse over time and will eventually cause a blow-up if no countermeasures are taken. However catastrophic that may sound, it is indeed a boon in some situations because the blow-up tells you unequivocally that something has gone horribly wrong where the remedies to aliasing might sometimes skillfully hide such a numerical failure.

Before turning to the antidotes, let us remark that spectral blocking can additionally be caused by choosing a time step that is too large, specifically when it violates the Courant–Friedrichs–Lewy condition [43].

There are a wide variety of possibilities to remedy this issue. Orszag proposed in 1971 an effective and simple de-aliasing method (in seven sentences no less!) [44]. This is a rule of thumb that works sufficiently well for many systems in flat space. At the end of every time step, all expansion coefficients corresponding to wavenumbers $|k| > \frac{2}{3}|k|_{\max}$ are set to zero while all others are left untouched. Consequently, it is also known as "Orszag's two-thirds rule." The two-thirds rule is an example of a broader class of spectral filtering methods where a filter function is applied to the coefficients in every time step to ensure their proper decay. In that sense, the filter for the two-thirds rule is simply a step-function. This is a rather brutal method, completely erasing one third of the spectrum, and relatively costly since you effectively reduce the degrees of freedom while still having to include all grid points in the computations. Therefore, continuous and smooth filters have become more and more popular. We will thus focus here on a filtering approach to combat aliasing in the time integration of the sGPE. But let it be said that there are other cures for aliasing. One example is the forceful conservation of the discretized energy [45]. The build-up of spectral blockage implies that the energy of the system increases unphysically. If one enforces exact conservation of energy within the numerical method, then the occurrence of spectral blockage is prohibited.

The time evolution of the sGPE is a fairly stable affair. Aliasing does occur, but at a slow rate. The effect is most pronounced when the features of the wave function are not well-resolved. In the present case, this means that the size of the vortex core must be sufficiently big, or, in other words, the radius of the sphere must not be much larger than the healing length. At a step size of $\delta t = 2 \times 10^{-5}$, it is possible to time-evolve the sGPE for a few hundred thousand steps before spectral blockage becomes visible.

While the two-thirds rule works well as a de-aliasing tool in the flat case, it has no effect in spherical geometry. It creates a discontinuity in the spectrum which leads to spectral blocking at that point instead of the edge of the spectrum. Indeed, aliasing is even stronger then, because the base value of the coefficients corresponding to $\frac{2}{3}l_{\max}$ is higher. It seems that this method simply relocates the issue and causes the modes with

$\frac{2}{3}l_{\max} < l \leq l_{\max}$ to be aliased as well. Instead, inspired by Ref. [46], we propose here an exponential, isotropic filter to suppress the high-l modes which is multiplied with every coefficient during every time step:

$$F_l = \begin{cases} 1 & l < l_{\text{cut}}, \\ e^{-\alpha(l-l_{\text{cut}})} & l \geq l_{\text{cut}}. \end{cases} \tag{5.31}$$

This method has two distinct advantages. First, it provides a continuous transition from the unfiltered to the filtered part of the spectrum. Second, at the cutoff point l_{cut}, below which no filtering is applied, instabilities can still grow even with a continuous filter. The numerical procedure is most stable when the strength of the filter α is tuned to respect the exponential decay exhibited by the spectrum. For long time-evolutions, however, not even this is sufficient. Therefore, the spectrum is recorded periodically and l_{cut} is adjusted dynamically if the spectrum grows above a certain threshold at that point. The efficacy of this method is outlined in Fig. 5.4.

However promising these results might be, there are certain pitfalls to de-aliasing. First of all, unless the filter exactly filters out the noise accumulation due to aliasing (it does not), then the conserved quantities of the sGPE (total energy, particle number, angular momentum) are no longer conserved, but will decay instead. One must therefore make sure that the loss is tenable compared to the initial values. Otherwise, the solution might be complete nonsense even though it will be smooth. Filtering is accordingly a last resort. If the flow is well-resolved, the time evolution will be stable for a long time, even if some amount of aliasing is unavoidable. A small spectral blockage is still acceptable and the filter should only be turned on once the danger of a blow-up arises.

5.3.3. Stationary dipoles?

A numerical method to determine the vortex positions with spectral accuracy and a filter that prevents the time evolution from exploding in place, we have all the tools necessary to examine the dynamics of the vortex dipole in detail. The procedure is simple. The wave function is initialized as in section 5.2 for differing values of θ_+ and particle number N, then propagated in time using the split-stepping method with different values of $\tilde{\omega}$. The particle number does not directly influence the dynamics, but the average particle

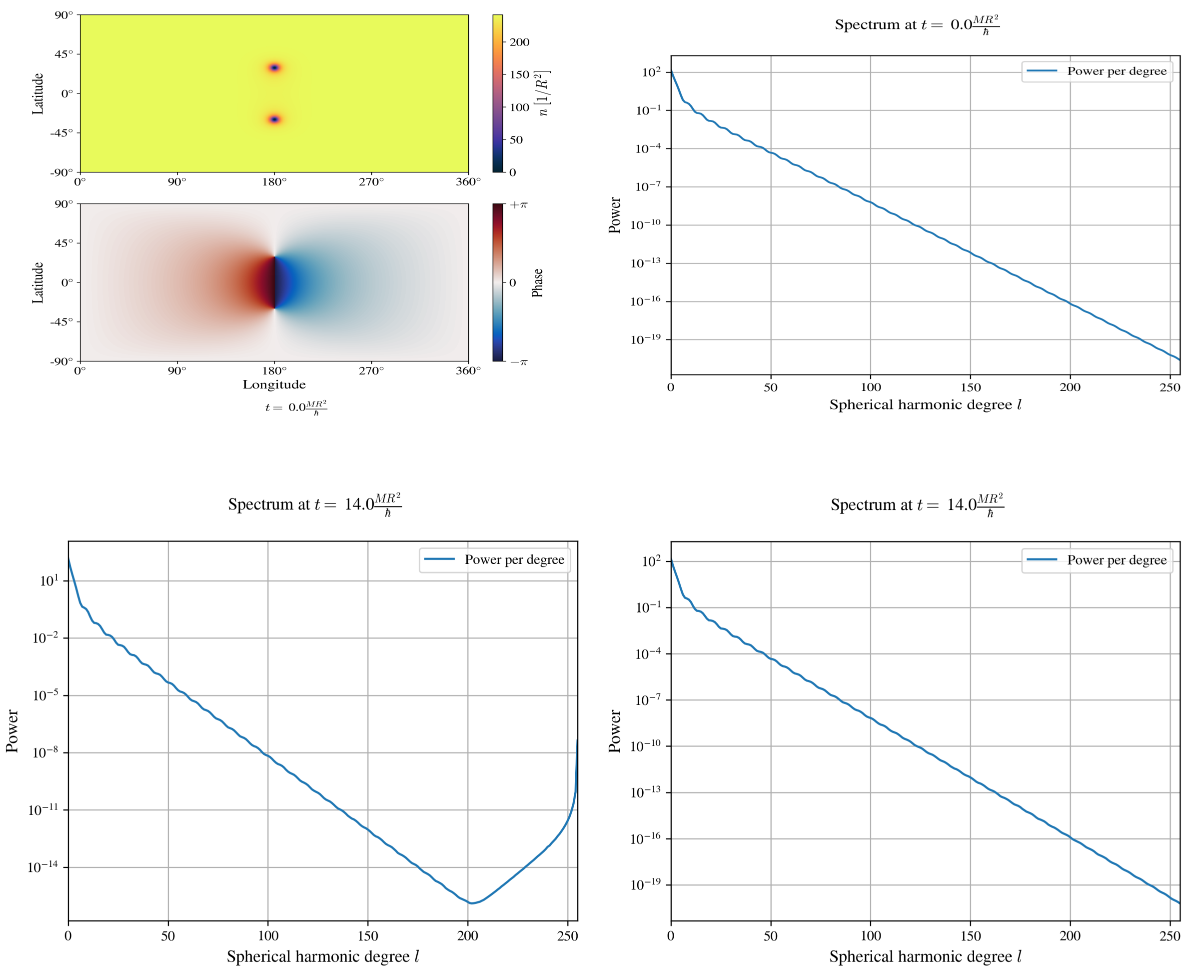

Figure 5.4: The top left panel shows the density and phase of a wave function containing a single vortex dipole with $\theta_+ = 60°$ while the top right panel shows its spectrum, initialized as in section 5.2. The wave function is then propagated in time. The bottom left panel shows the spectrum at the end of the time evolution without filtering. The buildup of spectral blockage is clearly visible and, if the time evolution is continued, would eventually lead to a complete break-down of the numerical method. The same time evolution was repeated with the filter (5.31) in place, shown in the bottom right panel. The spectrum is then visually unchanged in comparison to the initial condition. With a time step of $\delta t = 2 \times 10^{-5}$ and end time of $t = 14$, the total number of steps was 700,000. Without filter, spectral blockage begins to be visually perceptible after around 250,000 time steps. The strength of the filter was set to $\alpha = 0.01$ and $l_{\text{cut}} = l_{\max} - 20$.

density is related to it by $\bar{n} = N/(4\pi)$ and so the particle number affects the size of the vortices and thus how well the grid is able to resolve them. This is relevant for the amount of aliasing, as discussed above. The (angular) velocity of the vortex dipole in the rest frame of the sphere depends on their separation. The closer they are together, the higher their velocity. This is directly analogous to the flat case where the linear velocity is inversely proportional to their separation. A dipole with the vortex on the Northern Hemisphere and an antivortex on the Southern Hemisphere travels eastward, while the mirrored configuration travels westward. It was made sure that the dipole completes at least on rotation in the rest frame.

The first example of such a simulation is illustrated in Fig. 5.5. For a rotation frequency of $\tilde{\omega} = 0$, it is energetically favorable to reduce the separation of the vortices and eventually annihilate. The result of the time evolution shows that no such movement occurs. The polar position of the vortices oscillates slightly, but within a very small band around the initial position (pay specific attention to the numbers on the y-axis!). These oscillations may be related to imperfections in the initial condition. One can see the effect of the filtering in the conserved quantities that do decay, but on an absolutely miniscule scale compared to their initial values which constitutes another proof of concept for the filtering approach.

Secondly, in Fig. 5.6, the time evolution for a rotating sphere is shown. Here, the frequency of rotation was set to $\tilde{\omega} = -17.1$. For the vortex-antivortex pair, this suggests that $\theta_+ = 0$ constitutes the ground state of the system. In addition, the particle number was set much higher, corresponding to a maximum density of $n = 2000$. This makes the vortex cores tiny compared to the grid spacing. Here, we encounter the limits of the filtering method, which is reflected in the conserved quantities decaying on much larger scales and particularly fast towards the end of the time evolution. Roughly 22 particles are lost where it was below the numerical precission before. Due to the loss of energy, vortex separation also decreases somewhat monotonically. Still, this change in the polar position remains very small compared to the initial value of $\theta_+ = 30°$.

Lastly, the wave function was initialized with a slightly different initial θ_+, but a much smaller particle number, as shown in Fig. 5.7. The rotation frequency was kept the same to be able to compare to the previous time evolution. The results are very similar to the

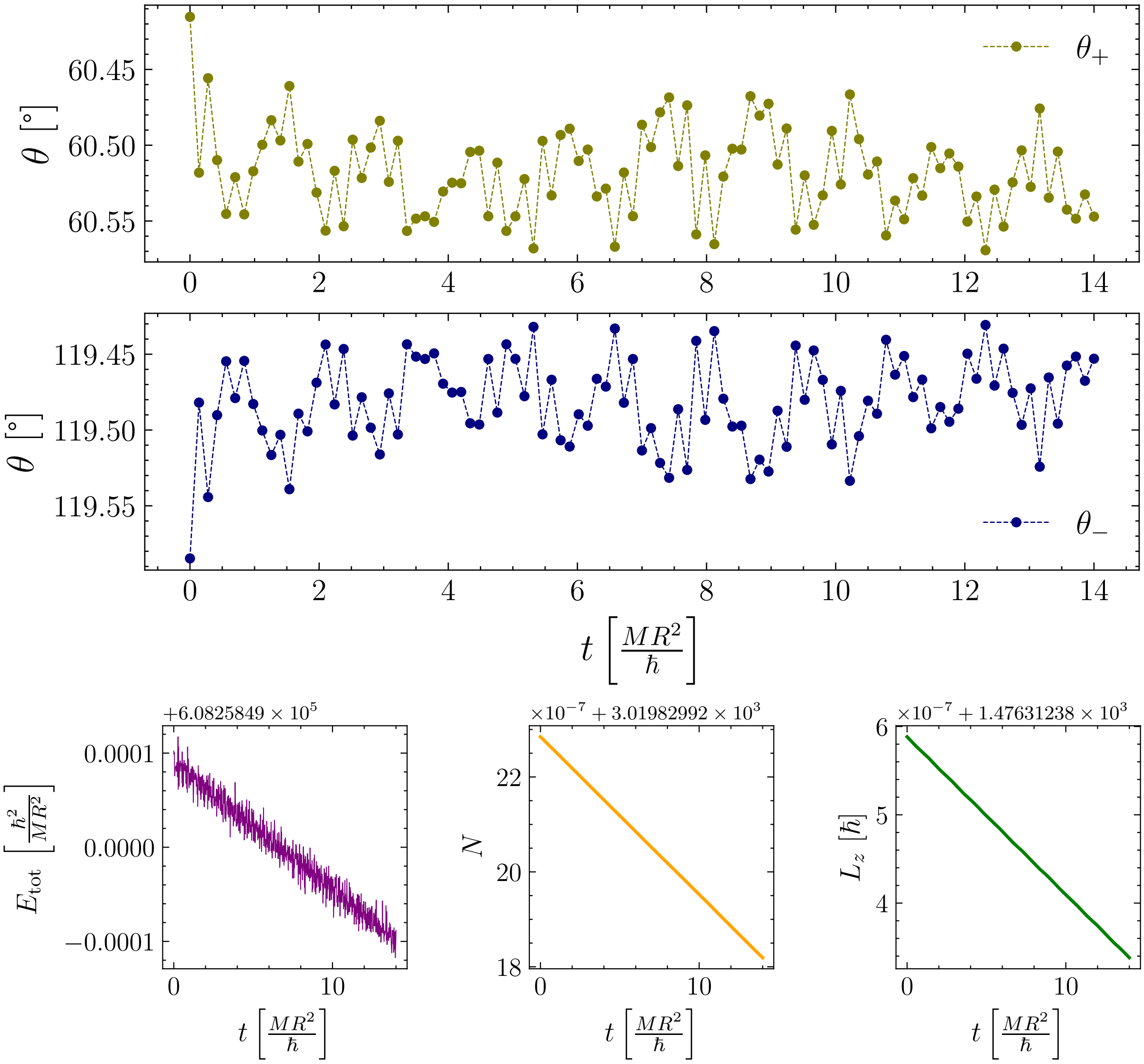

Figure 5.5: Wave function initialized with $\theta_+ = 60°$ and $N = 3020$, time evolution with $\tilde{\omega} = 0$. The two top panels show the polar angle of the vortex (in olive) and antivortex (in purple) as a function of time. The initial condition is exactly that of Fig. 5.4. The three panels in the bottom show the total energy, the particle number and the angular momentum of the wave function.

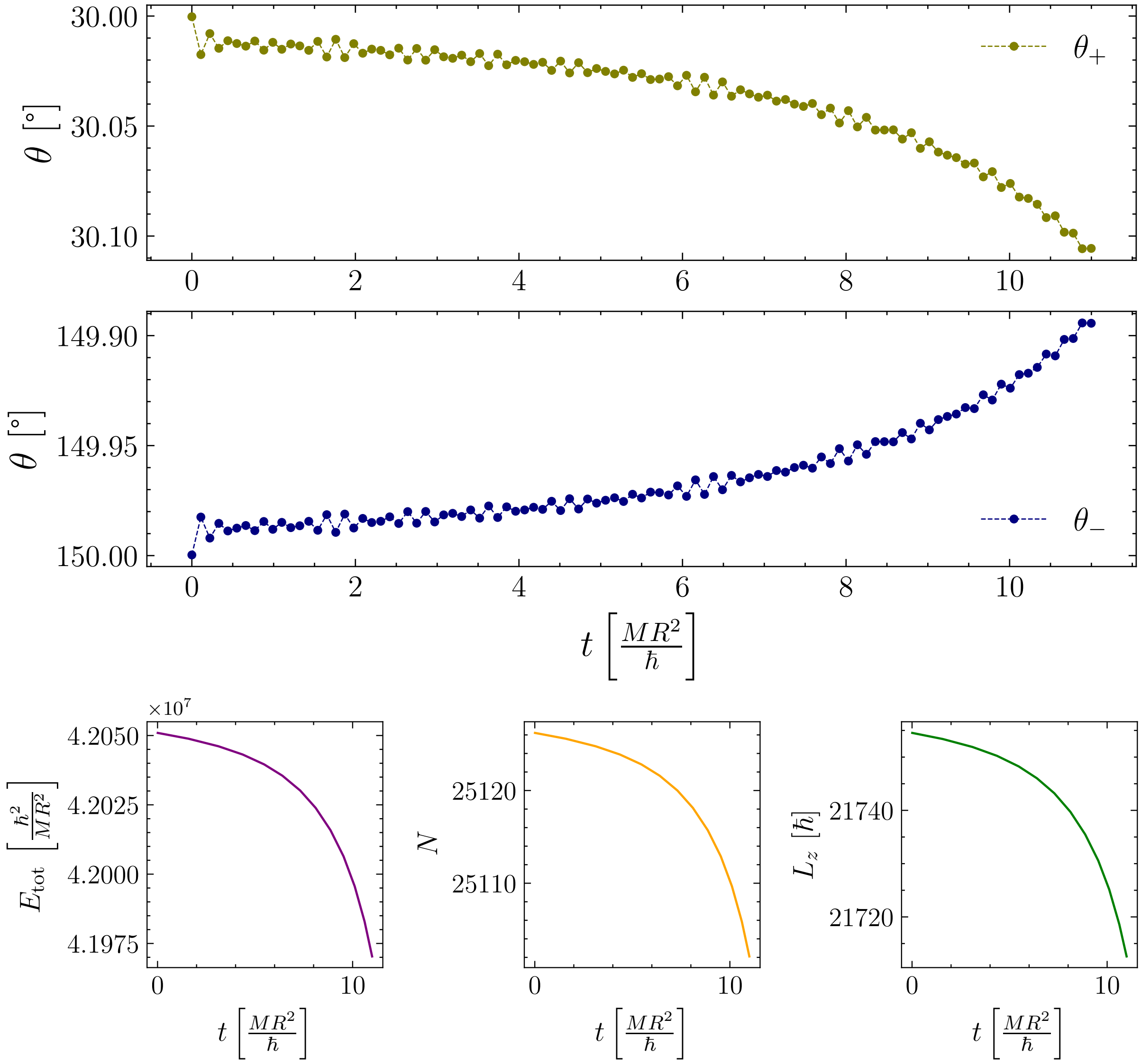

Figure 5.6: Wave function initialized with $\theta_+ = 30°$ and $N = 25126$, time evolution with $\tilde{\omega} = -17.1$. The two top panels show the polar angle of the vortex (in olive) and antivortex (in purple) as a function of time. The three panels in the bottom show the total energy, the particle number and the angular momentum of the wave function.

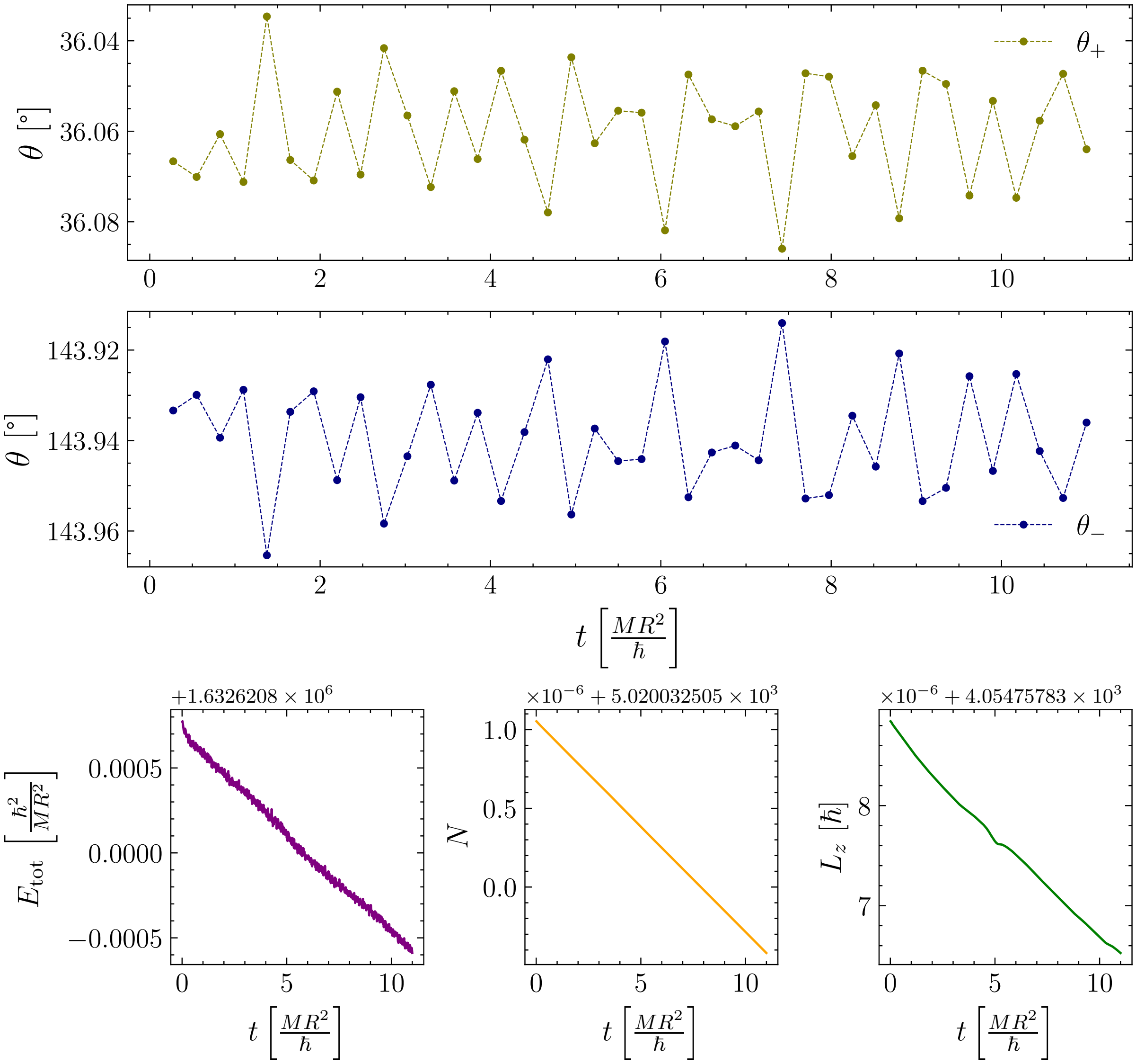

Figure 5.7: Wave function initialized with $\theta_+ = 36°$ and $N = 5020$, time evolution with $\tilde{\omega} = -17.1$. The two top panels show the polar angle of the vortex (in olive) and antivortex (in purple) as a function of time. The three panels in the bottom show the total energy, the particle number and the angular momentum of the wave function.

first example Fig. 5.5. There is an oscillating behavior around the initial positions, the conserved quantities decay very slowly, but no indication of a change in separation. This goes to show that one must stay vigilant when applying de-aliasing methods. A change in vortex size can have untenable consequences on the result of the time evolution.

Many more (too many to be shown here) simulations have been carried out and they all corroborate the same statement: Analogously to flat space, there is no mechanism through which the vortex pair can lose energy and increase or decrease its separation. Once their positions are set, they are very happy to remain at a constant distance and rotate with uniform speed around the sphere which suggests that the vortex dipole forms a traveling wave solution, i.e. $\Psi(\theta, \phi, t) = \psi(\theta, \phi + \omega t)$, where ω is the dimensionless angular velocity of the dipole. This brings us to an interesting question. If the sphere is rotated with some frequency $\tilde{\omega}$, can one then find a stationary solution of the sGPE for a dipole travelling on the sphere with angular velocity $-\tilde{\omega}$? A dipole with this configuration would then simply stay put, meaning that $\partial_t \psi = 0$. This is the central question of the present thesis and will be explored in the next chapter.

5.4. Ground State

Before turning to the discussion of stationary solutions in the rotating spherical BEC, let us briefly examine the effect of the rotation on its ground state which is a crucial characteristic of ultracold Bose gases. The ground state of an infinite 2D Bose gas responds to an external rotation with the formation of a vortex lattice, thereby breaking translational and rotational symmetry [47]. If ω is the frequency of external rotation, then the characteristic length scale between vortices is

$$\ell = \frac{\hbar}{2M\omega}\,, \tag{5.32}$$

with which eventually follows an estimation for the density of vortices in the ground state [39]

$$n_v = \frac{M\omega}{\pi\hbar}\,. \tag{5.33}$$

This result is also known as the "Feynman rule." The creation of vortex lattices in the flat plane has been studied in Refs. [48, 49]. For a system of finite size such as the surface of

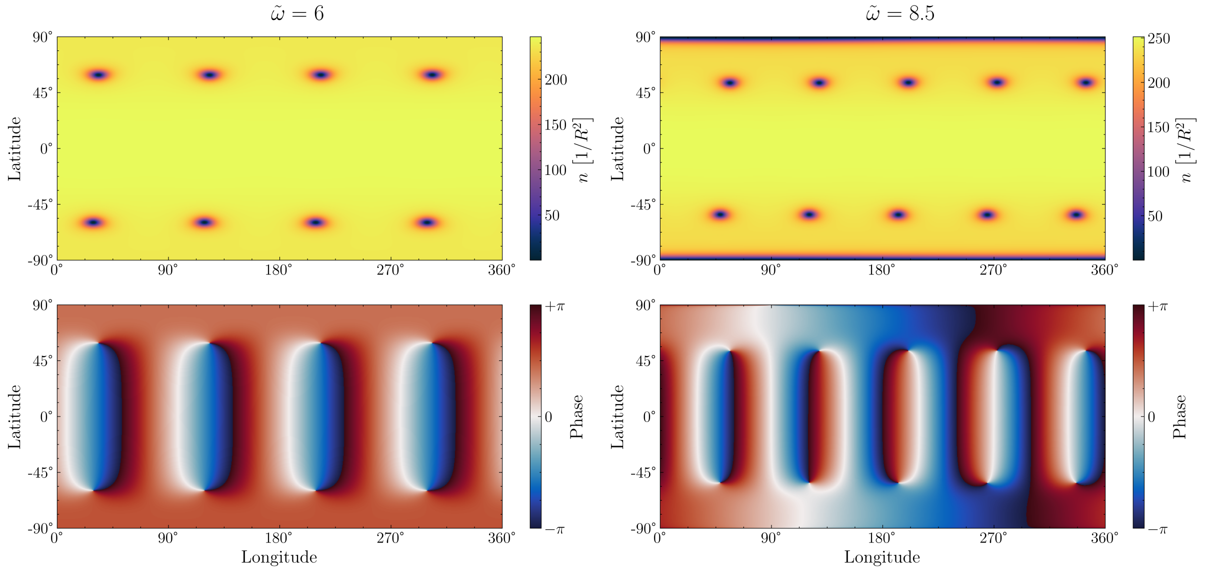

Figure 5.8: Vortex lattices in the ground state of a rotating spherical Bose gas for $\tilde{\omega} = 6$ (left) and $\tilde{\omega} = 8.5$ (right). Density in the top panels, phase in the bottom panels. The parameters were set to $\tilde{\mu} = 400$ and $\tilde{g} = 1.66$.

the sphere, it is more instructive to talk about the absolute number of vortices instead of the density. As outlined in the beginning of this chapter, the creation of vortices is only allowed in vortex-antivortex pairs, therefore we will look at the number of dipoles N_d in relation to the external rotation $\tilde{\omega}$. To study the ground state of the system, the wave function is initialized as

$$\Psi = \sqrt{\tilde{\mu}/\tilde{g}}\; e^{\mathrm{i}S_r} \,. \tag{5.34}$$

The density is set to be of constant, uniform value but the phase profile is imprinted with a number of dipoles. S_r sums up the phases (5.12) of the dipoles at randomly chosen angular positions $\theta_+, \phi_+, \theta_-, \phi_-$. Next, this initial condition is propagated in imaginary time for different values of $\tilde{\omega}$. In theory, as long as the initial condition has at least as many dipoles as the ground state it contains a contribution by the ground state, and thus we expect the imaginary time evolution to converge to the ground state.

The numerical results, however, suggest that reality is a bit more subtle and complicated. The imaginary time evolution is volatile with respect to the initial condition. While the numerical procedure itself is deterministic, the randomized initial positions generate different outcomes for a constant value of $\tilde{\omega}$. In practice, this means that the imaginary

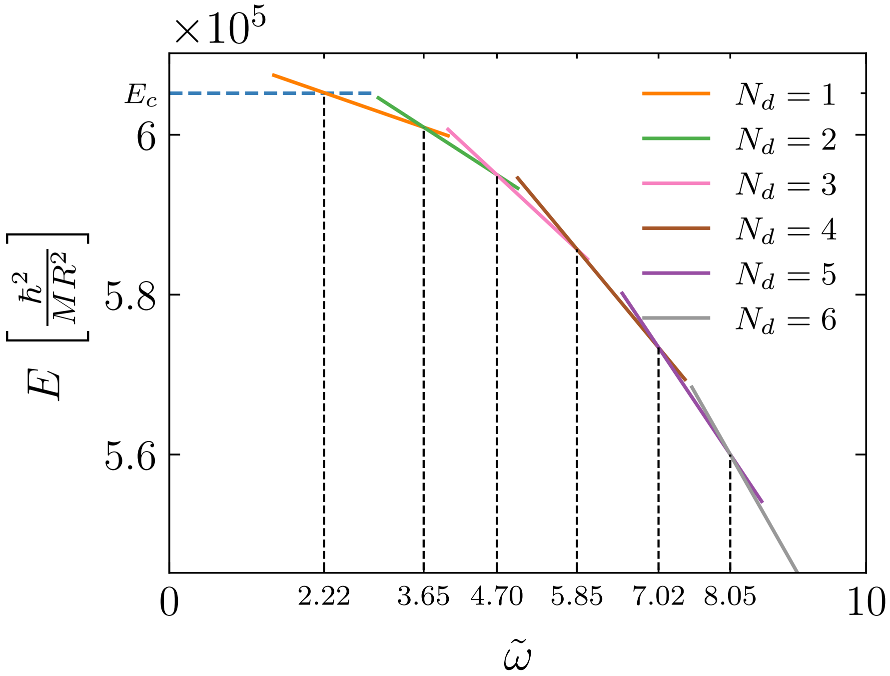

Figure 5.9: Energy of vortex lattices with N_d dipoles as a function of $\tilde{\omega}$. E_c is the energy of the homogeneous condensate which is the ground state below $\tilde{\omega} \approx 2.22$. The dashed vertical lines mark the transition to the vortex lattice with next highest N_d being the new ground state.

time converges to a wave function where N_d can take different values. This implies that the true ground state and excited states have comparable energies, and the imaginary time evolution is not consistently able to find the global energy minimum but instead converges to a local minimum. Consequently, for every $\tilde{\omega}$, there exist several energy minima associated with a specific vortex lattice and dipole number N_d. For a set $N_d > 1$, the lattice spacing changes depending on $\tilde{\omega}$. That is to say, the positions of the vortices responds to a change of $\tilde{\omega}$. If $N_d = 1$, then the lowest energy state is simply always the pole solution. Two of these vortex lattices are shown in Fig. 5.8. To make matters worse, even for fixed N_d and $\tilde{\omega}$, there may be more than one energy minimum. For example, the ground state for $\tilde{\omega} = 7.5$ contains $N_d = 5$ dipoles but there are two possible configurations. An antivortex at the North Pole, a row of four antivortices on the Northern hemisphere and a row of five vortices on the Southern hemisphere. Alternatively, a row of 5 antivortices on the Northern hemisphere, a row of four vortices on the Southern hemisphere and a vortex at the South Pole. However, these different states have numerically indiscernible energies so it stands to reason that they are degenerate. We will therefore not distinguish between them in the following.

To remedy these issues, both the initial number of phase defects in S_r is varied and many runs for different random initial positions are carried out to find the state with the lowest energy. Once a state with minimum energy has been found, we can follow the energy of that state by doing an imaginary time evolution with modified $\tilde{\omega}$. Thus, an energy landscape is created from which it can be numerically determined when N_d of the ground state changes its value. The results are illustrated in Fig. 5.9.

The important lesson here is that there is a linear relationship between N_d and $\tilde{\omega}$, similar to flat space. For $N_d > 1$, the difference between neighboring transition frequencies is roughly one. It is plausible that this relation does not hold for $N_d = 1$. The pole solution allows the vortices to have a single separation, whereas the vortex lattices characteristically exhibit different separations in longitudinal and latitudinal directions. From this follows a marked increase in the kinetic energy that accounts for the later transition to the next ground state.

Chapter 6

Jones-Roberts solitary waves

In this chapter, we will discuss a special class of solutions of the 2D and 3D GPE known as Jones-Roberts solitary waves (JRSW), or sometimes Jones-Roberts solitons. Let us begin by having a look at solitons as they materialize in the one-dimensional GPE and then how JRSWs form in two and three dimensions.

6.1. Solitons and solitary waves in the flat GPE

In general, solitons are solutions to nonlinear equations which take the form of strongly stable, completely localized excitations travelling with constant velocity (which can be zero). Additionally, they scatter elastically with other solitons, meaning that a soliton interaction retains their shape and velocity at large distances after the collision. Their stability is a consequence of the interplay between nonlinear and dispersive effects in the equations. More strictly speaking, they appear as solutions of integrable systems which are characterized by an infinite set of conservation laws ultimately giving rise to the localized solutions interacting elastically. The first such solution was described by Korteweg and de Vries modelling shallow-water waves, eventually formulating a 1D nonlinear PDE which was later named after them [50]. Nowadays, solitonic solutions are the focus of intense research in a wide variety of fields such as fluid dynamics, nonlinear optics and, in this case, Bose-Einstein condensation. The 1D GPE

$$\mathrm{i}\hbar\partial_t\Psi = -\frac{\hbar^2}{2M}\partial_x^2\Psi + g|\Psi|^2\Psi \tag{6.1}$$

has been shown to be integrable by the inverse scattering method [51], and indeed may be mapped onto the KdV equation with the application of a perturbational treatment [52]. The equation permits two different types of solitonic solutions. For a repulsive interaction ($g > 0$), the soliton travels with uniform speed v which is bound from above by the speed of sound $c = \sqrt{\mu/M}$ and its density profile is characterized by a zone of depletion whose size is fixed by the healing length $\xi = \sqrt{\hbar^2/(2\mu M)}$. This "dark soliton" takes the form

$$\Psi = \sqrt{n}\left(\mathrm{i}\frac{v}{v} + \sqrt{1-\frac{v^2}{c^2}}\tanh\left[\frac{x-vt}{\sqrt{2}\xi}\sqrt{1-\frac{v^2}{c^2}}\right]\right)e^{-\mathrm{i}\mu t/\hbar}\,, \tag{6.2}$$

where n is the bulk density and $\mu = ng$ the chemical potential (see section 5.5 of Ref. [53]). The density is symmetric around its minimum at $x = 0$ and its value there is $n(0) = nv^2/c^2$. Thus, a stationary dark soliton has a minimum of zero. For an attractive interaction ($g < 0$), the GPE admits the presence of a different soliton

$$\Psi = \sqrt{n}\frac{e^{-\mathrm{i}\mu \mathrm{t}/\hbar}}{\cosh\left(x/(\sqrt{2}\xi\right)}\,, \tag{6.3}$$

which is a localized wave packet with a peak at $x = 0$, and is thus referred to as a "bright soliton." Here, n refers to the density at the peak, $\mu = \frac{1}{2}ng$ and $\xi = \sqrt{-\hbar^2/(2ngM)}$. Closed analytic expressions for dark and bright solitons exist also in the presence of a harmonic confining potential and the formation of bright [54, 55] and dark [56, 57] solitons has been verified experimentally.

The picture changes considerably for higher dimensions. In 2D or 3D, the GPE is no longer an integrable PDE. Consequently, the existence of solitons is not permitted anymore. However, in their seminal paper from 1982, Jones and Roberts found a continuous family of localized solutions consisting of axisymmetric waves in two and three dimensions [58]. In the literature, similar solutions of nonlinear, non-integrable systems are often still referred to as solitons although they typically scatter inelastically and thus lose energy upon interaction, indicating that they are not true solitons. For the sake of clarity, we will strictly refer to these as solitary waves in the following. In two and three dimension, solitary waves are subject to instabilities like the snaking instability and are thus prone to decay [59, 60]. The solutions found by Jones and Roberts are the only known stable, dark solitary waves in the 2D and 3D GPE to date. They take the form of axisymmetric shape-preserving excitations whose speed, again, is bound from above by the speed of sound.

In three dimensions, there are two different regimes. At low velocities, the JRSWs appear as a vortex ring whose radius becomes larger as the speed decreases. In the limit of linear momentum $p \to \infty$ of the condensate, the radius becomes infinite and scales as $r \propto \sqrt{p}$. As the velocity increases, the radius of the vortex ring decreases until one eventually reaches a minimum in the energy-momentum ($E - p$) plane, where both energy and momentum are minimized. This constitutes the lower branch of the family of solutions. If the velocity is further increased, the topological defect disappears and a zone of density depletion remains. This transition marks the onset of the second, upper branch of solutions. This rarefaction pulse extends in all directions as its velocity increases, but becomes increasingly one-dimensional (thin and elongated) as the velocity reaches the speed of sound. At the same time, its amplitude decreases, but not sufficiently to prevent the energy and momentum from rising. From the minimum in the energy-momentum plane, both energy and momentum increase again with increasing velocity and the velocity approaches the speed of sound as $p \to \infty$ on the upper branch. Accordingly, for any momentum value above the minimum, there are two different solutions, one on the lower (vortex) branch and on the upper (rarefaction pulse) branch.

In two dimensions, there is only one branch of solutions. For small velocities, these are a single vortex dipole. As the velocity decreases, their separation and momentum increases and eventually becomes infinite for zero velocity. Increasing the velocity brings the two vortices closer together until they eventually overlap and annihilate. Here, too, an elliptically shaped rarefaction pulse remains that becomes elongated as the velocity is further increased. Unlike 3D, no second branch forms. Instead, as the velocity approaches the speed of sound, both energy and momentum go to zero. The rarefaction pulse becomes shallower and eventually gives way to a homogeneous condensate. In both two and three dimensions, the velocity of the JRSW is given by $\partial E/\partial p$ where the derivative is understood to be taken along the family of solutions. It has been established that solutions with $\partial E/\partial p = 0$ do not exist in 3D and thus the minimum in the energy-momentum plane is not smooth but instead forms a cusp, even though both energy and momentum have smooth minima as a function of the velocity. Both the lower 3D branch and the entire 2D branch have been shown to represent stable solutions [61]. For a visual representation of the energy-momentum curve, consult Figs. 2 and 3 of Ref. [58].

Although experimentally challenging, these predictions have been verified both in an atomic BEC [62] as well as in a quantum fluid of light [63].

Hereby follows the connection to the previous chapter. If stationary vortex dipole solutions of the sGPE can be found, then they constitute the low-velocity regime of the 2D JRSW branch. Is it then possible to incrementally increase the angular velocity of these solutions to eventually discover the transition from a vortex dipole to a rarefaction pulse just like Jones and Roberts have shown in flat space? This question will be addressed in the following sections.

6.2. Stationary solutions of the sGPE

In this section, we will discuss a numerical method to find the roots of the sGPE (i.e. a steady-state solution). Earlier, we have already encountered a root finding method in section 5.3.1 to track the movement of vortices. There, the Newton-Raphson method was employed to find the zeros of the complex wave function Ψ. Now, we wish to find a function Ψ, such that the sGPE becomes zero, that is $\partial_t \Psi = 0$. Let $\psi(\theta, \phi)$ be such a stationary solution of (3.20) to find

$$0 = -\frac{1}{2}\Delta_\Omega \psi + \tilde{g}|\psi|^2\psi - \mathrm{i}\tilde{\omega}\partial_\phi \psi - \tilde{\mu}\psi =: \mathscr{F}(\psi)\,. \tag{6.4}$$

Additionally, the nonlinear operator $\mathscr{F}$ was defined which formally is a mapping

$$\mathscr{F} : L^2(S^2, \mathbb{C}) \longrightarrow L^2(S^2, \mathbb{C})\,, \tag{6.5}$$

and $L^2(S^2, \mathbb{C})$ is the space of complex, square-integrable functions on the unit sphere. The generalization to nonlinear equations to find the roots of operators like $\mathscr{F}$ is often referred to as the Newton-Kantorovich method. We proceed as before, assuming that ψ_0 is a root of $\mathscr{F}$ and ψ_g is a guess which is sufficiently close to the root such that $||\mathscr{F}(\psi_g)||$ (definition of the norm below) is small. Let the subscripts r and i denote the real and imaginary parts. One can then employ the same "trick" as for the vortex tracking and write

$$\vec{\mathscr{F}}(\psi) = \begin{pmatrix} \mathscr{F}_r(\psi) \\ \mathscr{F}_i(\psi) \end{pmatrix}\,. \tag{6.6}$$

Next, $\vec{\mathscr{F}}$ is expanded around ψ_0 and the expansion is truncated after the linear term:

$$0 = \vec{\mathscr{F}}(\psi_0) = \vec{\mathscr{F}}(\psi_g) - \left.\begin{pmatrix} \frac{\partial \mathscr{F}_r}{\partial \psi_r} & \frac{\partial \mathscr{F}_r}{\partial \psi_i} \\ \frac{\partial \mathscr{F}_i}{\partial \psi_r} & \frac{\partial \mathscr{F}_i}{\partial \psi_i} \end{pmatrix}\right|_{\psi=\psi_g} \begin{pmatrix} \delta\psi_r \\ \delta\psi_i \end{pmatrix} + \dots\,, \tag{6.7}$$

where $\delta\psi = \psi_g - \psi_0$. The matrix entries of the linear term are no longer real numbers but instead linear operators, and thus it is non-trivial to invert. To continue, the linearized system of equations

$$\begin{pmatrix} \frac{\partial \mathscr{F}_r}{\partial \psi_r} & \frac{\partial \mathscr{F}_r}{\partial \psi_i} \\ \frac{\partial \mathscr{F}_i}{\partial \psi_r} & \frac{\partial \mathscr{F}_i}{\partial \psi_i} \end{pmatrix}\Bigg|_{\psi=\psi_g} \begin{pmatrix} \delta\psi_r \\ \delta\psi_i \end{pmatrix} = \begin{pmatrix} \mathscr{F}_r(\psi_g) \\ \mathscr{F}_i(\psi_g) \end{pmatrix} \tag{6.8}$$

must be solved. To do so, the operator (or Fréchet) derivative is introduced as

$$\frac{\partial \mathscr{F}}{\partial \psi}(\delta\psi) = \lim_{\epsilon\to 0} \frac{\mathscr{F}(\psi + \epsilon\delta\psi) - \mathscr{F}(\psi)}{\epsilon} \,. \tag{6.9}$$

Then, the linear operator matrix in (6.8) takes the form

$$\begin{pmatrix} \frac{\partial \mathscr{F}_r}{\partial \psi_r} & \frac{\partial \mathscr{F}_r}{\partial \psi_i} \\ \frac{\partial \mathscr{F}_i}{\partial \psi_r} & \frac{\partial \mathscr{F}_i}{\partial \psi_i} \end{pmatrix}\Bigg|_{\psi=\psi_g} = \begin{pmatrix} -\frac{1}{2}\Delta_\Omega + \tilde{g}(3\psi_{g,r}^2 + \psi_{g,i}^2) - \tilde{\mu} & 2\tilde{g}\psi_{g,r}\psi_{g,i} + \tilde{\omega}\partial_\phi \\ 2\tilde{g}\psi_{g,r}\psi_{g,i} - \tilde{\omega}\partial_\phi & -\frac{1}{2}\Delta_\Omega + \tilde{g}(3\psi_{g,i}^2 + \psi_{g,r}^2) - \tilde{\mu} \end{pmatrix} . \tag{6.10}$$

Additionally, the right hand side of (6.8) is given by

$$\begin{pmatrix} \mathscr{F}_r(\psi_g) \\ \mathscr{F}_i(\psi_g) \end{pmatrix} = \begin{pmatrix} -\frac{1}{2}\Delta_\Omega\psi_{g,r} + \tilde{g}(\psi_{g,r}^3 + \psi_{g,r}\psi_{g,i}^2) + \tilde{\omega}\partial_\phi\psi_{g,i} - \tilde{\mu}\psi_{g,r} \\ -\frac{1}{2}\Delta_\Omega\psi_{g,i} + \tilde{g}(\psi_{g,i}^3 + \psi_{g,i}\psi_{g,r}^2) - \tilde{\omega}\partial_\phi\psi_{g,r} - \tilde{\mu}\psi_{g,i} \end{pmatrix} . \tag{6.11}$$

The following procedure is then very similar to before. One starts with an initial guess ψ_g, and better approximations are found iteratively with $\psi_{\text{new}} = \psi_g - \delta\psi$. This iteration can be repeated as many times as necessary with ψ_{new} as the next guess. The theory of the Newton-Kantorovich method suggests that the algorithm will necessarily converge if the initial guess is good enough. The asymptotic convergence will be quadratic, meaning that $||\delta\psi^{(i)}|| \sim ||\delta\psi^{(i-1)}||^2$, where (i) denotes the i-th iteration. There are, however, a few caveats to this statement. Quadratic convergence will only set in for sufficiently large i. It will furthermore not continue indefinitely, but $||\delta\psi||$ will rather converge to a point that is determined by the machine precision (if the algorithm is not stopped earlier). Furthermore, convergence speed may be reduced to geometric in certain circumstances, particularly if errors are accumulated when solving the linearized problem (6.8). For the present purpose, we define the operator norm of $\mathscr{F}$ as

$$||\mathscr{F}(\psi)|| = \sqrt{\frac{1}{N}\int \mathrm{d}\Omega |\mathscr{F}(\psi)|^2} = \sqrt{\frac{1}{N}\int \mathrm{d}\Omega \left| -\frac{1}{2}\Delta_\Omega\psi + \tilde{g}|\psi|^2\psi - \mathrm{i}\tilde{\omega}\partial_\phi\psi - \tilde{\mu}\psi \right|^2} \,, \tag{6.12}$$

where N is the particle number of ψ. One assumes sufficient convergence once the norm of the operator has fallen below a certain tolerance, i.e. $\|\mathscr{F}(\psi_{\text{new}})\| < \epsilon$.
To find the stationary solutions in the spherical geometry, the major challenge is to solve the linear system of equations (6.8).

6.3. Linear solvers

Very generally, one may write a system of linear equations in the form

$$A \cdot \mathbf{x} = \mathbf{b} \, , \tag{6.13}$$

where $\mathbf{x}$ and $\mathbf{b}$ are vectors with n and m entries respectively and A is a $m \times n$ matrix. A and $\mathbf{b}$ are given and one wants to solve for $\mathbf{x}$. In the simplest case, A is invertible and the solution is $\mathbf{x} = A^{-1} \cdot \mathbf{b}$, as it was done in section 5.3.1. If A is not invertible, the linear solvers are still able to find solutions. There are a number of iterative algorithms to solve linear systems when A is square but not symmetric, including the biconjugate gradient stabilized method (BiCGSTAB) [64] and the generalized minimal residual method (GMRES) [65]. These methods are based on the creation of Krylov vectors. The basic idea is to apply A onto the right hand side repeatedly and thereby create the Krylov vector of n-th order $\mathbf{K}_n = A^n \cdot \mathbf{b}$. Krylov methods approximate the solution as a linear superposition of Krylov vectors:

$$\mathbf{x} \approx \sum_{n=0}^{k-1} c_n \mathbf{K}_n \, . \tag{6.14}$$

The challenge is then to reduce the computation time by minimizing the number k of Krylov vectors needed to construct the solution. For the present purpose, A is given by (6.10), $\mathbf{b}$ by (6.11) and solving (6.8) constitutes the main numerical bottleneck of the Newton-Kantorovich method. Thus, $\mathbf{x}$ and $\mathbf{b}$ each contain two entries given by real functions defined on the $N \times 2N$ grid. Linear solvers require the input vector to be stored as a 1D array, so the gridded data of the two functions is flattened and then the two are concatenated to give a 1D array of length $4N^2$. The flattening is done in such a way that the rows of the gridded data are glued next to each other. It is, in principle, possible to discretize the linear operator (6.10) and represent it as a matrix. For the usual grid size of $N = 512$, the matrix would have 2^{40} entries, a size that is prohibitively expensive. To remedy the issue, most programming languages provide a Linear Operator class. In that case A need not be a matrix, but instead can be implemented as an object of that class which behaves as a function with the vector $\mathbf{x}$ as its input and the vector $A \cdot \mathbf{x}$ as its output.

The most relevant optional argument to accelerate the convergence of linear solvers is to provide a preconditioner. In effect, preconditioning aims to provide an approximation of the inverse of A. There are well-known preconditioning methods to find stationary solutions of the GPE in flat space. Refs. [66, 67] seem to suggest that a sensible choice to use for the preconditioner is

$$(1-\mathscr{L})^{-1} = \left(1 + \frac{1}{2}\Delta_\Omega + \mathrm{i}\tilde{\omega}\partial_\phi + \tilde{\mu}\right)^{-1}, \tag{6.15}$$

where $\mathscr{L}$ is the linear part of $\mathscr{F}$. The inversion is done easily enough, since $\mathscr{L}$ is diagonal in the space of spherical harmonics. In the vector notation this would translate to the preconditioner M taking the form

$$M \begin{pmatrix} \delta\psi_r \\ \delta\psi_i \end{pmatrix} = \begin{pmatrix} \left[(1-\mathscr{L})^{-1}\delta\psi\right]_r \\ \left[(1-\mathscr{L})^{-1}\delta\psi\right]_i \end{pmatrix}. \tag{6.16}$$

Unfortunately, neither this nor any other attempted choice for M brings the desired result. None of the plausible preconditioning methods in the literature have shown any impact on the performance of the linear solver. A successful preconditioner can reduce the number of iterations necessary for convergence by up to two orders of magnitude while (6.16) slows it down. Future research could focus on working out the proper expression for the preconditioner. For now, we must be content with a rather slow convergence.

The next question to ask is which iterative method is most suitable for the problem at hand. While both BiCGSTAB and GMRES have their adherents, the decision is taken off our hands. The BiCGSTAB algorithm does not provide sufficient convergence consistently in the spherical geometry. The typical behavior is that it only converges up to the second or third Newton-Kantorovich iteration and not afterwards. BiCGSTAB is therefore unsuited to find stationary solutions of the sGPE. The performance of GMRES has seen improvements by the development of new techniques to accelerate its convergence. These improvements have been implemented as the methods LGMRES [68] and GCROT [69]. LGMRES provides convergence in fewer iterations, reducing the overall convergence time despite a slower computation time per iteration compared to GMRES. LGMRES has therefore been the linear solver of choice. Incidental testing with GCROT has also been promising, and its performance may be similar to LGMRES.

With the linear solver established, let us turn to the input parameters to produce the fastest convergence time. The Newton-Kantorovich method itself has a tolerance to determine when the solution is sufficiently stationary. Similarly, the linear solver must be given a tolerance to check for convergence. That is to say it produces a vector $\mathbf{x}^{(i)}$ in the i-th iteration that will be returned as the solution to (6.13) if the residual

$$\frac{||\mathbf{b} - A \cdot \mathbf{x}^{(i)}||}{||\mathbf{b}||} \tag{6.17}$$

is smaller than the tolerance. In spherical geometry, the convergence of the linear solver is considerably slower than in flat space. A tolerance of 0.09 to extract the stationary solutions has proven to be appropriate and will be used in the following. If no starting guess is given, the solver starts with a vector of zeros such that the initial residual is one. A good guess that puts the residual below one reduces the time to convergence but has no influence on the number of iterations needed from the starting residual. No other input arguments of the LGMRES algorithm impact the performance in any meaningful way, therefore it is not necessary to deviate from the default values.

Lastly, it is instructive to briefly talk about the form of the initial guess ψ_g. It is essential to the convergence of the linear solver that the solution one is looking for is properly resolved by the grid in every Newton iteration. In the present case, this means that the size of the vortices must be sufficiently large. This will be done by appropriately tuning the dimensionless chemical potential $\tilde{\mu}$ and thereby the healing length ($\xi = 1/\sqrt{2\tilde{\mu}}$). It is likely that the linear solver accumulates aliasing errors if the vortex cores are not covered by enough grid points and therefore cannot converge. While solving (6.8) has been made possible by LGMRES for a broad set of parameters, many intricacies of the numerical treatment of the spherical geometry remain mysterious, and we will see that the method is not universally reliable.

6.4. From dipole to rarefaction pulse

With the discussion of the methods to find stationary solutions of the sGPE under our belt, it is time to turn theory into practice. The dimensionless coupling constant $\tilde{g} = 1.66$

will be kept constant throughout. We will aim to find different branches of solutions for $\tilde{\mu} \in \{50, 333, 400, 529\}$. The initial guess ψ_g will be given by a short imaginary time evolution of the initial condition as in section 5.2. Its particle number is set to $N = 4\pi\tilde{\mu}/\tilde{g}$. To get an idea which value to put in for the rotation frequency, ψ_g is propagated in time and its angular velocity recorded. The negative of that value is then used for $\tilde{\omega}$. Since the initial dipole travels eastward, $\tilde{\omega}$ is smaller than zero. Thus, all the parameters of $\mathscr{F}$ are fixed and the Newton-Kantorovich method can begin. The tolerance is set to $\epsilon = 9 \times 10^{-5}$ and convergence is typically achieved within four to seven iterations. Once a converged solution is found, it is used as a new initial guess for a modified rotation frequency $\tilde{\omega} - \delta\tilde{\omega} < \tilde{\omega}$. All other parameters are kept fixed. The vortices are therefore compelled to move closer together. Since the Newton method is quite sensible to the initial guess, it is vital to choose $\delta\tilde{\omega}$ to be small. Then, the procedure begins anew, and in that way one

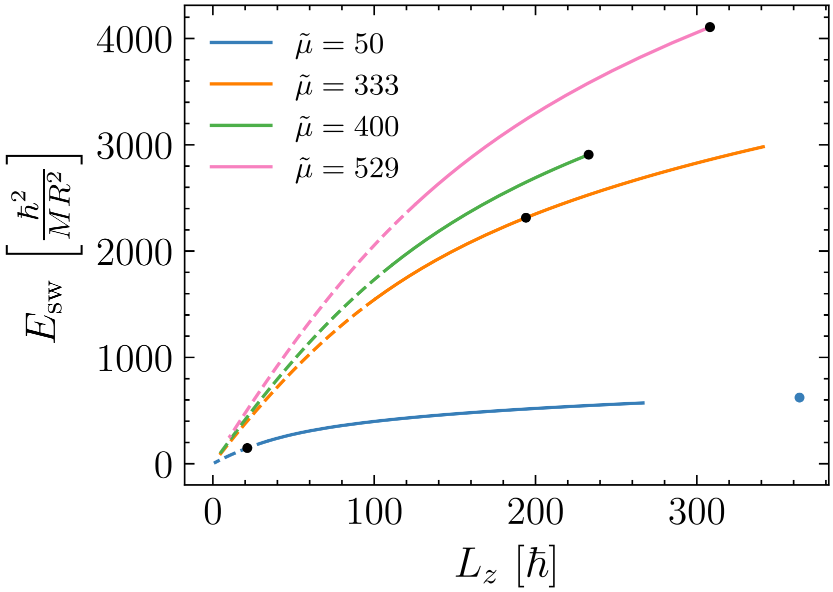

Figure 6.1: Energy-momentum curve of Jones-Roberts solitary waves for different $\tilde{\mu}$. The solid lines represent dipole solutions, the dashed lines represent rarefaction pulse solutions. The black dots show where the solution for $\tilde{\omega} = -6.1$ is situated. The blue dot shows the position of the pole solution ($\theta_+ = 0$) for $\tilde{\mu} = 50$. The energy of the solitary waves E_{sw} is given by adding kinetic and interaction energy of the solution and subtracting the homogeneous condensate energy of equal particle number.

follows a branch of solutions for a particular value of $\tilde{\mu}$. As $\tilde{\omega}$ is decreased incrementally, new solutions with decreasing dipole separation are found iteratively. Eventually, the vortices overlap and annihilate, thereby eliminating all vorticity from the wave function. What remains is a rarefaction pulse that is symmetric around the equator. As the rotation frequency is further decreased, the size of the pulse increases in latitudinal direction while becoming shallower. This transition from a vortex dipole to a rarefaction pulse is identical to the description of Jones and Roberts in their paper. The existence of families of Jones-Roberts solitary waves has therefore been established numerically for the spherical case. It is important to stress that this is a central result of the thesis as it was initially unclear whether these solutions exist, and if so, in what form. The energy-momentum curve for the four branches is shown in Fig. 6.1 where the angular momentum L_z replaces the linear momentum. For a visual representation of the wave function as it transitions to a rarefaction pulse, see Fig. 6.2.

One can further extract the maximal angular velocity $\tilde{\omega}_{\max}$ and the critical angular velocity $\tilde{\omega}_c$ at which the transition occurs. Since $\xi = 1/\sqrt{2\tilde{\mu}}$, increasing the chemical potential relates to a smaller size of the vortices. Accordingly, their separation must become small for them to overlap and annihilate from which follows that $\tilde{\omega}_c$ increases with $\tilde{\mu}$. These matters are illustrated in Table 2. Note that these are all positive numbers. While $\tilde{\omega}$ is negative and refers to the frequency with which the sphere is rotated, the JRSWs move in the opposite direction and their velocities are therefore positive. Near the transition, there are two solutions where vorticity disappears from one to the other. $\tilde{\omega}_c$ is taken to be the value exactly in between the velocities of these two solutions and its error is the distance from either one. As the density dip becomes shallower it is increasingly difficult for the linear solver to converge which is especially true the smaller the vortex size. Therefore, $\tilde{\omega}_{\max}$ does not constitute the maximally available angular velocity. The higher $\tilde{\mu}$, the larger the distance in energy to the homogeneous condensate of the $\tilde{\omega}_{\max}$-solution.

Interestingly, $\tilde{\omega}_{\max}$ exceeds the speed of sound (3.73) in all cases, a phenomenon that is entirely prohibited in the infinite, flat plane for which a rigorous mathematical proof exists [70]. The idea is that the speed of sound is the minimum speed of delocalized Bogoliubov excitations (phonons). As soon as a traveling wave reaches the speed of sound, energy is transferred onto the delocalized excitations. Thus, the wave must emit

$\tilde{\mu}$	$\tilde{\omega}_c$	$\tilde{\omega}_{\max}$	$\tilde{\omega}_s$
50	4.535 ± 0.005	8.0	7.1
333	11.23 ± 0.01	19.6	18.3
400	12.25 ± 0.05	21.2	20
529	14.05 ± 0.05	23.8	23

Table 2: $\tilde{\omega}_c$ is the angular velocity where the transition from dipole to rarefaction pulse occurs, $\tilde{\omega}_{\max}$ is the maximum angular velocity for which a solution was found. $\tilde{\omega}_s$ is the angular speed of sound.

sound, therefore lose energy and its localized character, and disappear. Mathematically, localized solutions with supersonic speed are not allowed to decay asymptotically. Instead, they have oscillating tails that radiate away energy. However, the story gets a little more subtle when leaving the infinite plane and introducing periodicity. In section 6.7, we will encounter a physical reason why these supersonic solutions may exist. For the moment, we can also make arguments based on the geometric situation. While periodic boundary conditions are a numerical tool in flat space, periodicity is an intrinsic feature of the spherical geometry. The notion of a localized solution is therefore different since one cannot speak anymore of asymptotic decay as the distance grows to infinity. Instead, the localized object must be much smaller than the domain size, as it might interact with itself otherwise. This self-interaction can stabilize solutions that would otherwise be unstable. Due to the periodicity, phonons are not able to escape towards infinity but instead wrap around and can in principle re-interact with the structure that emitted them. Additionally, finite systems feature a discrete phonon spectrum (see the Bogoliubov dispersion (3.68)), which means that a solution might not properly couple to any phonon mode. Notably, the supersonic JRSW solutions exhibit a strongly nonlocalized density profile (see Fig. 6.3), reinforcing these suspicions. We therefore contend that supersonic JRSWs likely do not constitute fully localized solutions.

In two and three dimensions, it has been shown that the flat GPE may be mapped onto the Kadomtsev–Petviashvili (KP) equation in the limit of speeds close to the speed of sound

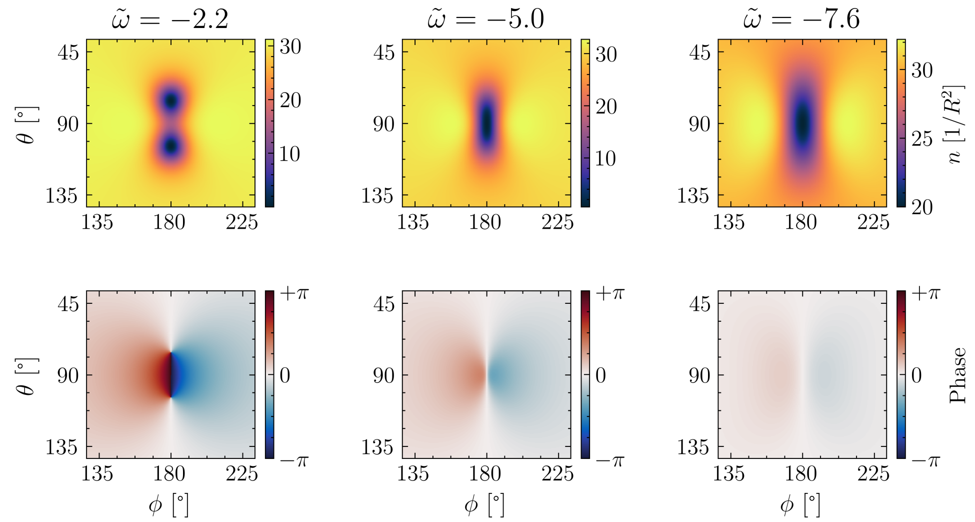

Figure 6.2: JRSW solutions for $\tilde{\mu} = 50$ and decreasing $\tilde{\omega}$. The top panels show the density and the bottom panels the phase of the respective wave function in a region around the disturbance. One starts out with two vortices that draw closer as $\tilde{\omega}$ decreases. The solution for $\tilde{\omega} = -5.0$ is shortly after the transition to a rarefaction pulse. Then, the extent of the excitation grows and its amplitude shrinks while the phase gradient diminishes.

[58, 61]. The KP equation arises in fluid dynamics as a (2 + 1)D generalization of the KdV equation and likewise models weakly dispersive shallow-water waves [71]. Importantly, the KP equation constitutes an integrable system and explicit analytic expressions for solitonic solutions are known (see Ref. [72] for the first such solution). These solitons are characterized by an algebraic decay and are called “lump” solitons. It has thus been conjectured that in this limit, the JRSWs transition to solutions of the KP equation and become true solitons, but no rigorous proof exists. However, it was shown that lump solitons can be mapped to traveling wave solutions of the GPE in the transonic limit [73]. The general relation between JRSWs and lump solitons is not yet established but continues to be investigated. Let us end the discussion of the high velocity regime for the spherical geometry by noting that the density profiles of supersonic solutions as shown in Fig. 6.3 resemble those of lump solutions of the KP equation (e.g. compare with Refs. [74, 75]). The typical structure being a peak in the density next to the depletion zone. Therefore, it might well be the case that these already constitute solitons or near-

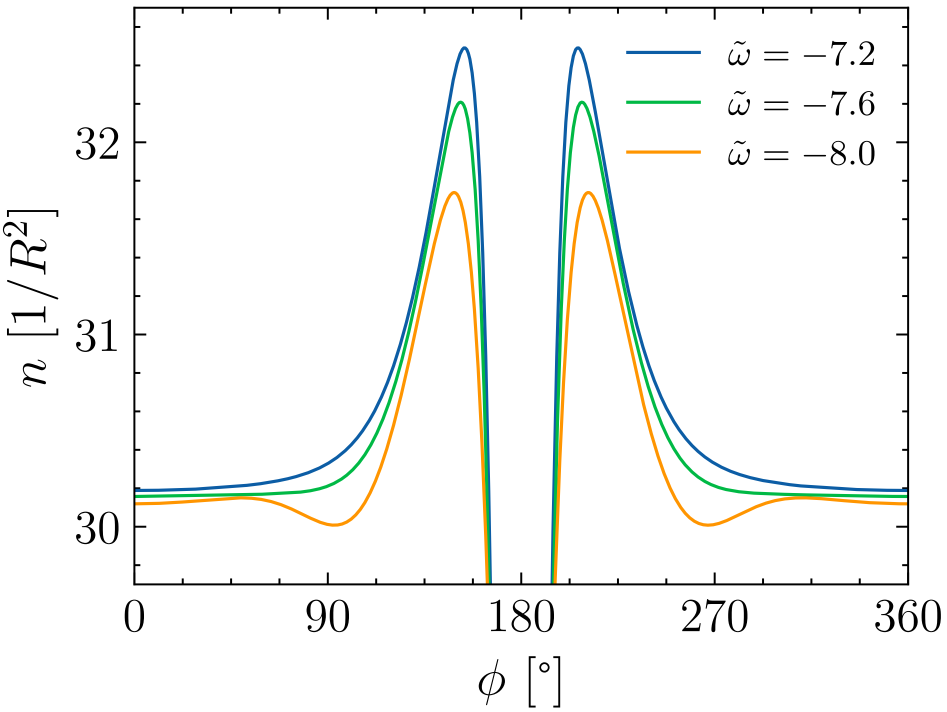

Figure 6.3: Density profiles of supersonic JRSWs along the equator for $\tilde{\mu} = 50$

solitonic solutions. Additional evidence is brought forward by the fact that these fast solutions emit next to no sound upon scattering, indicating that the interactions might be (almost) completely elastic (see Fig. 6.4).

The other regime of interest is presented by the low velocity dipole solutions. Here, we encounter a qualitative difference to the flat case necessitated by the compact geometry. In the infinite plane, a vortex dipole may have any arbitrary separation and their velocity goes to zero as the separation goes to infinity. This is no longer possible on the sphere because there is a maximum separation which is reached when both vortices are situated at the poles. For this vortex pole configuration, any external rotation $\tilde{\omega}$ yields a stationary solution as the wave function is then given by $\psi(\theta, \phi) = f(\theta)e^{\mathrm{i}\phi}$ and

$$-\tilde{\mu}\psi - \mathrm{i}\tilde{\omega}\partial_\phi\psi = -(\tilde{\mu} - \tilde{\omega})\psi\,. \tag{6.18}$$

Hence, the external rotation merely modifies the chemical potential. The stationary solutions for the pole configuration are easily found and the respective angular momentum and energy for one such solution ($\tilde{\mu} = 50$ and $\tilde{\omega} = 0$) have been inscribed into Fig. 6.1 as

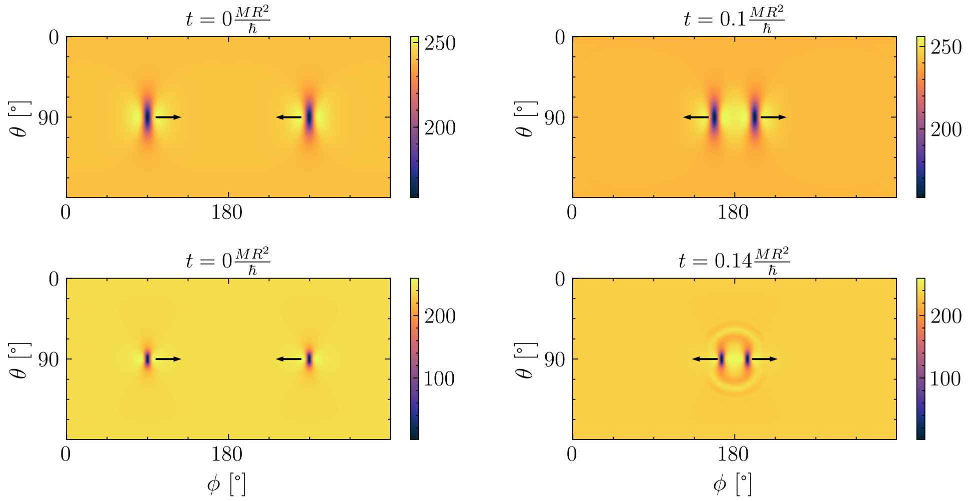

Figure 6.4: Scattering simulation of two JRSWs of equal but opposite speed for $\tilde{\mu} = 400$. All panels show the density of the wave function in units of $1/R^2$. The left panels show the initial condition, the right panels are snapshots shortly after the interaction. The top panels correspond to an angular velocity of $13\frac{\hbar}{MR^2}$, the bottom panels to an angular velocity of $19.6\frac{\hbar}{MR^2}$. After the scattering event, the slower waves emit visually perceptible sound while the faster ones do not.

a reference (the blue dot). By the above argument, it is impossible to move the vortices away from the poles by changing $\tilde{\omega}$. Therefore, one cannot follow the family of solutions by starting at the poles. The other direction proves equally troublesome. While it is possible to increase $\tilde{\omega}$ for a while and find new solutions with increasing vortex separation, the numerical procedure eventually fails at around $\tilde{\omega} = -0.69$, where the linear solver is no longer able to converge. Only the energy-momentum curve for $\tilde{\mu} = 50$ in Fig. 6.1 shows the branch of solutions until numerical failure, but this has been true for all values of $\tilde{\mu}$. It is unclear why this occurs. Perhaps additional solutions do not exist, perhaps the energy-momentum curve is discontinuous, perhaps the wave function changes very rapidly with varying $\tilde{\omega}$. On the other hand, there might be an issue with the numerical method itself. Whatever the reason, the completion of the full branch of JRSWs remains beyond the scope of this work.

6.5. Stability analysis

While Jones-Roberts solitary waves have been numerically shown to exist on the spherical surface, it remains to be seen whether they are stable objects. To begin with, the solitary waves are propagated in time with a white noise perturbation added

$$\psi = \psi_{\mathrm{sw}} + \eta\,, \tag{6.19}$$

where ψ_{sw} is the wave function of a solitary wave and η is a Gaussian white noise signal whose amplitude is $10^{-3} \cdot \max(|\psi_{\mathrm{sw}}|)$. The temporal evolution of ψ does not result in a change of shape of the disturbance, nor is the height of the density depletion zone affected by it (see Fig. 6.5). This is first tentative evidence for the stability of the solutions. To test the stability of the system rigorously, one must perform a linear stability analysis. As a start, consider the configuration where both vortices are at the poles. Then, the

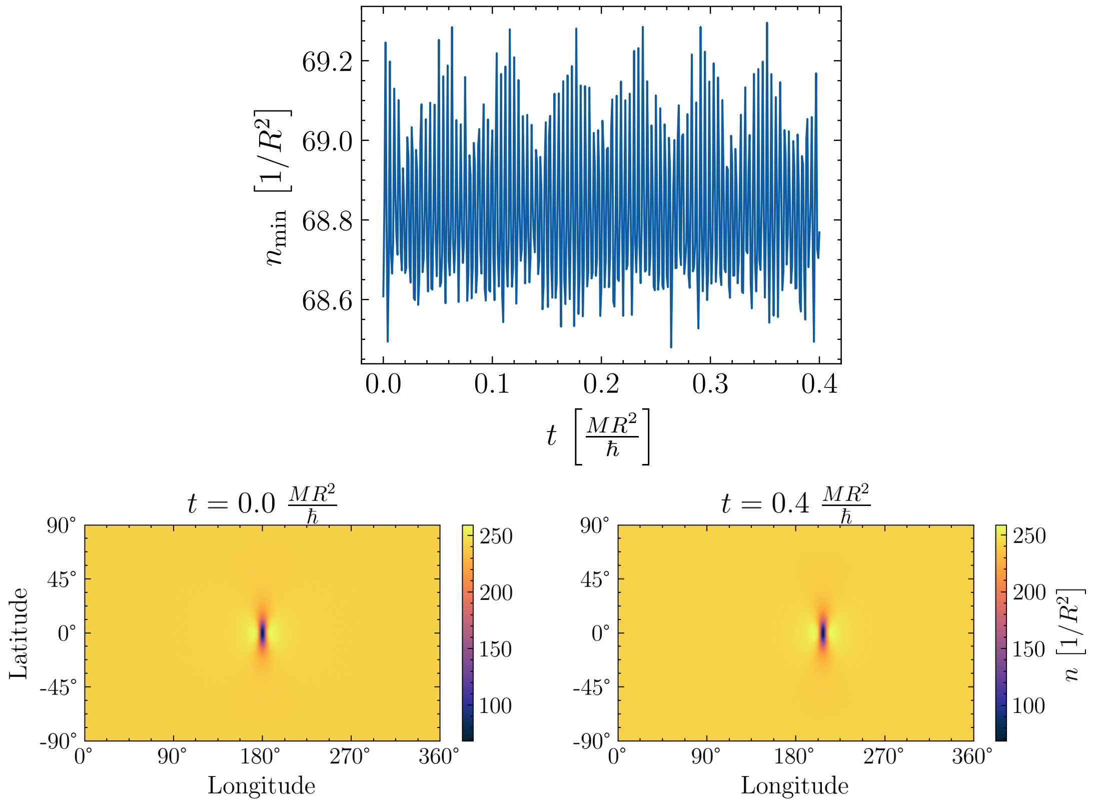

Figure 6.5: The minimum density of a JRSW time evolution in the top panel. The bottom panels show the density of the initial JRSW ($\tilde{\mu} = 400$, $\tilde{\omega} = -16.9$) + noise and of the wave function after it has completed one revolution.

wave function is simply given by $\psi_{\text{pole}} = f(\theta)e^{\mathrm{i}\phi}$. Add now linear perturbations to its magnitude in the form

$$\psi(\theta,\phi) = \left(f(\theta) + a(\theta)e^{\sigma t} + b^{*}(\theta)e^{\sigma^{*} t}\right)e^{\mathrm{i}\phi}\,. \tag{6.20}$$

Inserting this ansatz into the sGPE yields the following set of equations after collecting all the terms proportional to $e^{\sigma t}$ and $e^{\sigma^{*} t}$:

$$\mathrm{i}\sigma a = \mathscr{L}_0 a + \tilde{g}f^2(2a+b)\,, \tag{6.21}$$

$$-\mathrm{i}\sigma b = \mathscr{L}_0 b + \tilde{g}f^2(2b+a)\,, \tag{6.22}$$

where the linear operator

$$\mathscr{L}_0 := -\frac{1}{2\sin\theta}\partial_\theta(\sin\theta\,\partial_\theta) + \frac{1}{2\sin^2\theta} - (\tilde{\mu} - \tilde{\omega}) \tag{6.23}$$

was introduced. Inspired by Ref. [76], this expression can be further simplified by writing

$$u = a + b\,, \tag{6.24}$$

$$v = a - b\,, \tag{6.25}$$

which leads to

$$\mathrm{i}\sigma u = \mathscr{L}_0 v + \tilde{g}f^2 v\,, \tag{6.26}$$

$$\mathrm{i}\sigma v = \mathscr{L}_0 u + 3\tilde{g}f^2 u\,. \tag{6.27}$$

This is equivalent to the eigenvalue equation

$$\sigma\begin{pmatrix} u \\ v \end{pmatrix} = -\mathrm{i}\begin{pmatrix} 0 & \mathscr{L}_0 + \tilde{g}f^2 \\ \mathscr{L}_0 + 3\tilde{g}f^2 & 0 \end{pmatrix}\begin{pmatrix} u \\ v \end{pmatrix}\,. \tag{6.28}$$

To test the stability of the pole solution, it is therefore necessary to compute the eigenvalues of the matrix on the right hand side.

In contrast, for a solitary wave solution away from the poles, the linear stability analysis is very similar but numerically considerably more complex. Consider a solitary wave solution ψ_{sw} with added linear perturbations, i.e.

$$\psi(\theta,\phi) = \psi_{\text{sw}}(\theta,\phi) + \alpha(\theta,\phi)e^{\sigma t} + \beta^{*}(\theta,\phi)e^{\sigma^{*} t}\,. \tag{6.29}$$

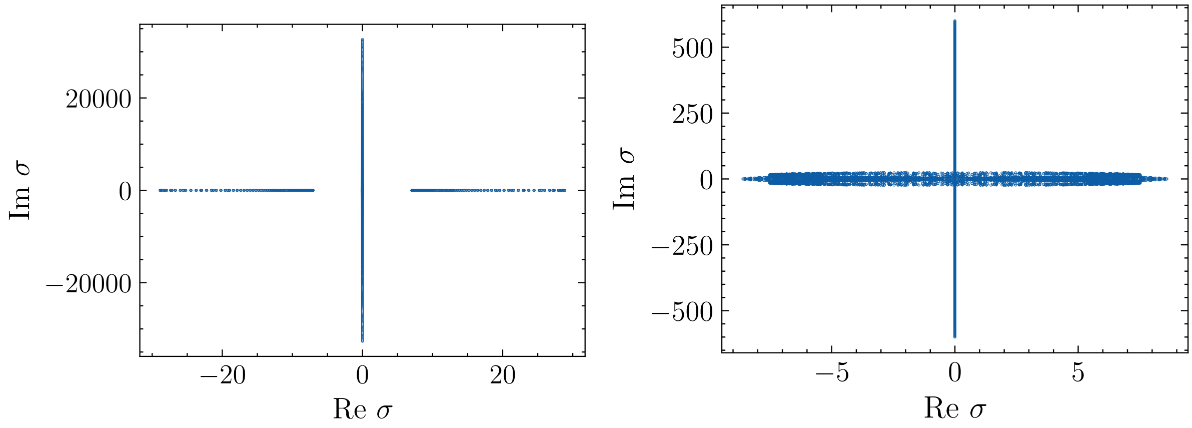

Figure 6.6: Eigenvalues of (6.28) for $\tilde{\mu} = 50$ and $\tilde{\omega} = 0$ in the left panel. Eigenvalues of (6.30) on a 64 × 128 grid for $\tilde{\mu} = 15$ and $\tilde{\omega} = -2.885$ in the right panel.

Different than before, α and β are now functions of both angles which spells trouble. Proceeding as above, the ansatz is inserted into the sGPE and the terms proportional to $e^{\sigma t}$ and $e^{\sigma^* t}$ are collected, leading to the eigenvalue equation

$$\sigma \begin{pmatrix} \alpha \\ \beta \end{pmatrix} = -\mathrm{i} \begin{pmatrix} -\frac{1}{2}\Delta_\Omega + 2\tilde{g}|\psi_{\mathrm{sw}}|^2 - \mathrm{i}\tilde{\omega}\partial_\phi - \tilde{\mu} & \tilde{g}\psi_{\mathrm{sw}}^2 \\ -\tilde{g}\psi_{\mathrm{sw}}^2 & \frac{1}{2}\Delta_\Omega - 2\tilde{g}|\psi_{\mathrm{sw}}|^2 - \mathrm{i}\tilde{\omega}\partial_\phi + \tilde{\mu} \end{pmatrix} \begin{pmatrix} \alpha \\ \beta \end{pmatrix}, \tag{6.30}$$

which, in this case, cannot be further simplified. The complications arise because the matrix in (6.30) has 2^{20} eigenvalues for a 512 × 1024 grid while the matrix in (6.28) has 2^{10}. It is computationally infeasible to calculate all of them, both in terms of memory and computation time, but the problem can be made accessible by reducing the grid size. The largest grid size where all eigenvalues (minus two) can be computed is a 64 × 128 grid. As shown in Fig. 6.6, for both eigenvalue equations, there exist a large number of eigenvalues with positive real value suggesting that the solitary waves are unstable objects. This leads to an obvious contradiction with the result from the dynamics where - even with large-amplitude noise signals - no decay of the disturbance was observed. It is unclear where this contradiction arises and it will need further study in the future.

6.6. Variational approach for solitary wave speed

Jones and Roberts have shown in Ref. [58] for the flat case that the speed of the solitary wave is given by $\partial E/\partial p$. We will follow their lead and extend the argumentation to the spherical geometry. The energy and angular momentum of the JRSWs are formally given by

$$\begin{aligned} E_{\mathrm{sw}} &= \int \mathrm{d}\Omega \left\{ \frac{1}{2}\nabla\psi\cdot\nabla\psi^* + \frac{\tilde{g}}{2}|\psi|^4 - \tilde{\mu}|\psi|^2 \right\} , && (6.31) \\ L_z &= -\mathrm{i}\int \mathrm{d}\Omega\psi^*\partial_\phi\psi\, , && (6.32) \end{aligned}$$

and the wave function ψ is a stationary solution, i.e. it obeys

$$-\frac{1}{2}\Delta\psi + \tilde{g}|\psi|^2\psi - \tilde{\mu}\psi = \mathrm{i}\tilde{\omega}\partial_\phi\psi\, . \tag{6.33}$$

One may then perform the infinitesimal variation

$$\psi \to \psi + \delta\psi \tag{6.34}$$

in the above integrals. For the angular momentum, one finds

$$\begin{aligned} L_z + \delta L_z &= -\mathrm{i}\int \mathrm{d}\Omega(\psi^* + \delta\psi^*)\partial_\phi(\psi + \delta\psi) \\ &= -\mathrm{i}\int \mathrm{d}\Omega\left(\psi^*\partial_\phi\psi + \delta\psi^*\partial_\phi\psi - \delta\psi\partial_\phi\psi^*\right) . \end{aligned} \tag{6.35}$$

The terms nonlinear in $\delta\psi$ are discarded, and one assumes the same symmetry around the equator for $\delta\psi$ that is present for ψ to set the “boundary” terms arising from the integration by parts to zero. It follows that

$$\delta L_z = -\mathrm{i}\int \mathrm{d}\Omega\left(\delta\psi^*\partial_\phi\psi - \delta\psi\partial_\phi\psi^*\right) . \tag{6.36}$$

The procedure for the energy is very similar and leads to

$$\begin{aligned} E_{\mathrm{sw}} + \delta E_{\mathrm{sw}} &= \int \mathrm{d}\Omega \left\{ \frac{1}{2}\nabla(\psi+\delta\psi)\cdot\nabla(\psi^*+\delta\psi^*) + \frac{\tilde{g}}{2}(\psi+\delta\psi)^2(\psi^*+\delta\psi^*)^2 - \tilde{\mu}(\psi+\delta\psi)(\psi^*+\delta\psi^*) \right\} \\ &= E_{\mathrm{sw}} + \int \mathrm{d}\Omega \Bigg\{ \delta\psi \underbrace{\left(-\frac{1}{2}\Delta\psi^* + \tilde{g}|\psi|^2\psi^* - \tilde{\mu}\psi^*\right)}_{-\mathrm{i}\tilde{\omega}\partial_\phi\psi^*} + \delta\psi^* \underbrace{\left(-\frac{1}{2}\Delta\psi + \tilde{g}|\psi|^2\psi - \tilde{\mu}\psi\right)}_{\mathrm{i}\tilde{\omega}\partial_\phi\psi} \Bigg\} . \end{aligned} \tag{6.37}$$

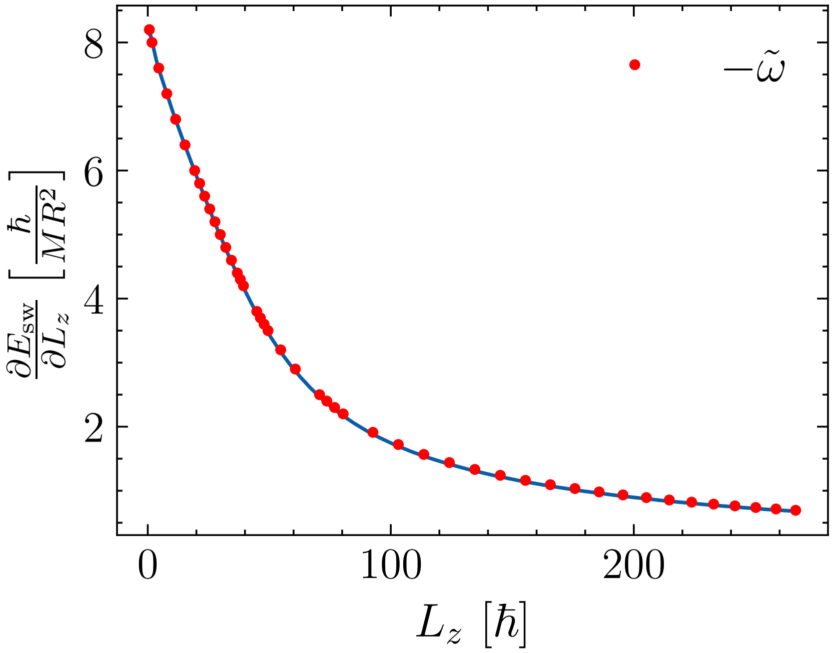

Figure 6.7: The blue line shows the derivative of energy with respect to angular momentum for $\tilde{\mu} = 50$. The red dots are the angular velocities of the JRSWs at the corresponding angular momentum.

Therefore, the variation of the energy is

$$\delta E_{\mathrm{sw}} = -\mathrm{i}\tilde{\omega} \int \mathrm{d}\Omega \left(\delta\psi \partial_\phi \psi^* - \delta\psi^* \partial_\phi \psi\right) = -\tilde{\omega} \delta L_z \,. \tag{6.38}$$

If $\delta\psi$ is the variation that takes ψ to the next member of the branch of solutions, then the variation of the energy is proportional to the variation of the angular momentum. This means that

$$\frac{\partial E_{\mathrm{sw}}}{\partial L_z} = -\tilde{\omega} \,, \tag{6.39}$$

if we understand the derivative to be taken along the energy-momentum curve which is in line with the flat case since $-\tilde{\omega}$ is the angular velocity of the JRSWs. This analytic result is complemented by numerical calculations. Fits of the curves in Fig. 6.1 are created by constructing smoothing splines to generate a fit function that passes through the points given by the data. The spline fit can then be differentiated with the finite difference method which neatly overlaps with the corresponding values of $-\tilde{\omega}$. This result is shown for $\tilde{\mu} = 50$ in Fig. 6.7.

6.7. Dispersion relation

To round out the discussion of solitary waves on the surface of a sphere, let us look at the dispersion relation they produce. If the external rotation of the sphere is turned off, it is clear that the JRSWs are no longer time-independent. Instead they move in longitudinal direction with the negative of $\tilde{\omega}$ for which they are stationary, i.e. $\psi(\theta, \phi, t) = \psi(\theta, \phi - \tilde{\omega} t)$. If ψ_l^m are the spherical harmonics expansion coefficients of the stationary solution, then

$$\psi(\theta, \phi - \tilde{\omega} t) = \sum_{l=0}^{\infty} \sum_{m=-l}^{l} \psi_l^m e^{-\mathrm{i} m \tilde{\omega} t} Y_l^m(\theta, \phi)\,, \tag{6.40}$$

which follows from the form of the spherical harmonics. In other words, the expansion coefficients become functions of time and take the form $\psi_l^m e^{-\mathrm{i} m \tilde{\omega} t}$. This means that they oscillate with the frequency $-m\tilde{\omega}$. Thus, we expect that this behavior is reproduced in the spectrum of the expansion coefficients. To examine this statement, the procedure is exactly as in section 5.1, the result of which is shown in Fig. 6.8.

While the spectrum accurately displays the dispersion relation, the Bogoliubov dispersion (3.68) is still visible. This is likely the effect of aliasing errors present after the Newton-Kantorovich method. Which is to say that the numerical expansion coefficients deviate from their exact values, and these deviations correspond to infinitesimal Bogoliubov excitations. This statement is corroborated by the fact that the spectra of the solitary

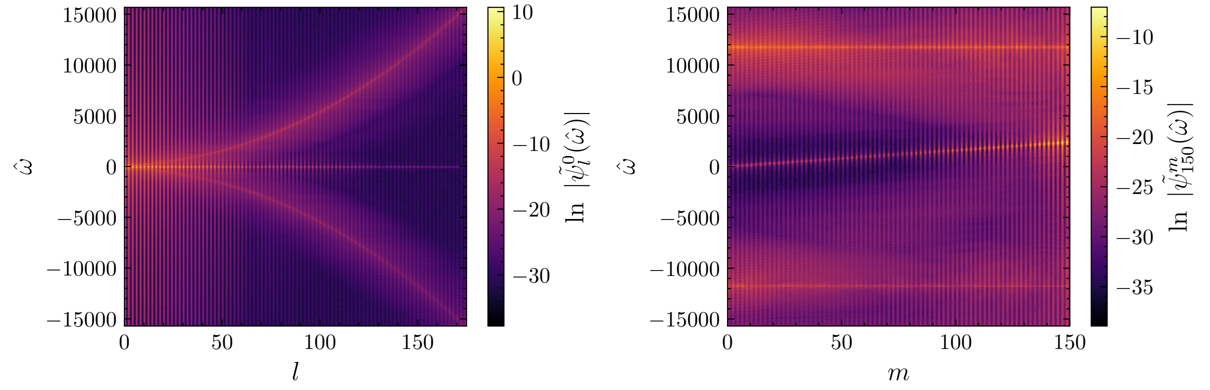

Figure 6.8: Dispersion of JRSW moving with $-\tilde{\omega} = 14$. The left panel shows the spectrum for $m = 0$. The right panel shows the spectrum for $l = 150$. The numerical dispersion exactly overlaps with the analytical result $-m\tilde{\omega}$. Additionally, the Bogoliubov dispersion is still visible.

$\tilde{\mu}$	$\tilde{\omega}_c$	$\tilde{\omega}_{\max}$	$\tilde{\omega}_s$	$\min_{l\neq 0} \frac{\lvert\tilde{\omega}_l^0\rvert}{l}$
50	4.535 ± 0.005	8.0	7.1	8.29
333	11.23 ± 0.01	19.6	18.3	19.88
400	12.25 ± 0.05	21.2	20	21.67
529	14.05 ± 0.05	23.8	23	24.74

Table 3: $\tilde{\omega}_c$ is the angular velocity where the transition from dipole to rarefaction pulse occurs, $\tilde{\omega}_{\max}$ is the maximum angular velocity for which a solution was found. $\tilde{\omega}_s$ is the angular speed of sound. $\min_{l\neq 0} \frac{|\tilde{\omega}_l^0|}{l}$ is the condition for energy transfer.

waves do not exhibit a purely exponential decay, but are rather characterized by a hump for large l. This suggests that there is indeed some buildup of aliasing errors which are reduced by a higher convergence tolerance.

Here, we can deduce a physical argument for the existence of supersonic JRSWs. For any fixed l, the maximum frequency of the solitary waves is reached for $|m| = l$. For energy transfer to the Bogoliubov modes not to occur, this frequency must be smaller than the smallest frequency in the Bogoliubov dispersion relation. In other words,

$$|\tilde{\omega}|l < |\tilde{\omega}_l^0| \quad \forall l \neq 0 \Longrightarrow |\tilde{\omega}| < \min_{l\neq 0} \frac{|\tilde{\omega}_l^0|}{l} \,. \tag{6.41}$$

Energy transfer is contingent on the speed and the frequency of the excitations to coincide with those of the Bogoliubov modes. In flat space, both of these conditions translate to the same mathematical relation, namely that $v < \min_k \omega(k)/k$, where $\omega(k)$ is the Bogoliubov dispersion. But not so on the sphere. With the condition (6.41) in mind, we can complete Table 2 to find Table 3.

It follows that $\tilde{\omega}_{\max}$ is always smaller than $\min_{l\neq 0} |\tilde{\omega}_l^0|/l$. Hence, one can conclude that, even though the speed of sound was breached by the solitary waves, energy transfer to the Bogoliubov modes is not possible until the higher value of $\min_{l\neq 0} |\tilde{\omega}_l^0|/l$ is reached. Additionally, in the large radius limit, (6.41) takes the form (with units included)

$$\lim_{R\to\infty}\min_{l\neq 0}\frac{|\omega_l^0|}{l}=\lim_{R\to\infty}\min_{l\neq 0}\sqrt{\frac{\hbar}{2MR^2}\frac{l+1}{l}\left(\frac{\hbar}{2MR^2}l(l+1)+\frac{2\mu}{\hbar}\right)}=\sqrt{\frac{\mu}{MR^2}}=\omega_s\,. \tag{6.42}$$

This is a necessary consistency check, because the large radius limit marks the transition to flat space and we must therefore recover this relation. One would therefore expect that for larger radius (or conversely large $\tilde{\mu}$) $\tilde{\omega}_{\mathrm{max}}$ is eventually bound from above by $\tilde{\omega}_s$. Indeed, the ratio $\tilde{\omega}_s/\tilde{\omega}_{\mathrm{max}}$ increases for increasing $\tilde{\mu}$. Unfortunately, the grid resolution does not permit finding solutions for arbitrarily high values of $\tilde{\mu}$ and thus this hypothesis can presently not be tested rigorously.

Chapter 7

Conclusion and Outlook

In this thesis, we have examined traveling wave solutions of a Bose-Einstein condensate on the surface of a sphere. We began by expressing the typical equation of motion, the Gross-Pitaevskii equation, in spherical coordinates to numerically treat the system. While the procedure is very similar to the flat case, it introduces a new length scale: the radius of the sphere R. This leads to a specific non-dimensionalization suited to the geometry. To get a better understanding of the effects of the geometry in comparison to flat space, we discussed a broad spectrum of theoretical results, including the condensate fraction and the critical temperature, pertaining to the homogeneous Bose gas on the spherical surface without localized excitations. The Bogoliubov dispersion is of particular interest because it provides a tool to scrutinize the numerical methods and gives access to the speed of sound.

Next, a sophisticated numerical apparatus to treat the spherical system was introduced and implemented as a codebase. This might prove to be quite useful not only in furthering the research of Bose-Einstein condensation but also to spherical fluid dynamics in general. The primary point of comparison are the planetary sciences (as planets are spheres) where the implementation of numerical methods based on spherical harmonics has been common practice for decades.

As a first test of the numerical methods, it was shown that the Bogoliubov dispersion is accurately reproduced which instilled confidence to expand the system to include localized excitations. Hence, the next step was to place a vortex-antivortex pair, the minimally allowed configuration, on the surface. This can be achieved by projecting the phase profile of a vortex dipole in flat 2D onto the sphere. The dynamics of these dipoles suggested that they might form stationary solutions with the right tuning of the dimensionless, external rotation frequency $\tilde{\omega}$. Additionally, we showed that the ground state of the system responds to a change in $\tilde{\omega}$ with the formation of vortex lattices. The relation between the number of dipoles in the ground state N_d and $\tilde{\omega}$ seems to be roughly linear, suggesting a continuation of the Feynman rule on the sphere.

The paramount result of this work has been the numerical proof of existence for a family of Jones-Roberts solitary waves in the spherical Gross-Pitaevskii equation. These are localized traveling wave solutions that form a vortex dipole at low angular velocities and transition to a rarefaction pulse at high angular velocities. For various values of the dimensionless chemical potential $\tilde{\mu}$, this transition was recorded and illustrated as a curve in the energy-angular momentum plane. Interestingly, supersonic solitary waves have been found to exist. These seem to be a consequence of the fact that energy transfer to the Bogoliubov modes necessitates an angular velocity that exceeds the angular speed of sound. There is tentative evidence that the "solitonicity" of the solutions increases with their angular velocity which is in line with the hypothesis that the solitary waves become solutions of the Kadomtsev–Petviashvili equation in the high-velocity limit and form so-called lump solitons. Furthermore, we have investigated in part the stability of the solitary waves but could not come to a definitive conclusion. The speed of the solitary waves is given by the derivative of their energy with respect to their angular momentum, a result that has been verified both numerically and analytically. Lastly, we ascertained that the dispersion relation of the solitary waves correctly shows up in the numerics.

While these are promising results, some problems have been left unanswered. First and foremost, it was not possible to complete the branches of solutions to the poles, the reason for which is similarly elusive. The development of a proper, functioning preconditioning method to solve the linear system of equations (6.8) would have a massive impact on the speed of convergence and would be an important and essential step forward on the numerical side of things. Simulations with well-resolved, large spheres would be able to find out whether the angular velocity of the JRSWs eventually becomes bound from above by the angular speed of sound. Furthermore, the implementation of a method to reliably find the eigenvalues of (6.30) with largest real value for arbitrary grid sizes within an acceptable time frame is equally crucial to conclude the question of stability.

Of course, the spherical geometry holds many more mysteries. While outside the scope of the present thesis, from its inception several interesting questions came up which could lead to compelling findings beyond the discussion of Jones-Roberts solitary waves.

Planetary waves

Planetary waves such as Rossby, Kelvin or Yanai waves are large-scale perturbations occurring in the atmosphere and oceans of planets which develop as a consequence of the planetary rotation. As a prominent example, atmospheric Rossby waves are caused by the Coriolis force and conservation of potential vorticity. They from along the polar front of cold polar air and warmer subtropical air creating meandering wave patterns that rotate westward. The similarity of the fluid dynamics between a planetary system and a spherical BEC is immediately clear and has hence sparked interest in their study. Rossby waves have also been theorized to exist in a rapidly rotating BEC in flat 3D [77]. Ref. [78] shows that the perturbation potential

$$V_p = \alpha(t) \sin^m(\theta) \cos(m\phi)$$

is able to excite a Rossby mode in the spherical BEC, where m is an integer and $\alpha(t)$ is a function of time that linearly goes to zero. The further study of Rossby or other planetary waves may thus prove to be an insightful course of future research.

Dipolar Bose Gas

Condensates with dipole-dipole interactions have been the object of intense experimental and theoretical research over the past years. Dipolar BECs and the formation of supersolids have already been observed theoretically in the quasi-2D regime of a thin spherical shell [79, 80]. Still pending is the study of topological defects and the extension of the model to a truly 2D sphere which needs careful consideration due to the peculiar form of the dipole-dipole potential in spherical coordinates.

Gravity

Gravity constitutes a major roadblock for the experimental realization of spherical Bose gases. We have only briefly touched on this in the beginning, but conveniently never turned on gravity in our theoretical considerations. If gravity is aligned along the z-axis, one can introduce the one-body potential

$$V_G = MGR \cos\theta \,,$$

where G is the local gravitational acceleration. Then, testing the robustness of the system against gravitational sag is an interesting point of inquiry from an experimental standpoint alone.

Bose-Einstein condensation on the surface of a sphere has attracted attention only for a few years. These ideas reveal that there is a wealth of directions that future research could touch upon. This thesis has tried to provide another small piece of the puzzle, but inevitably there is still much more to learn.

References

[1] S. N. Bose. "Plancks Gesetz und Lichtquantenhypothese". In: *Zeitschrift für Physik* 26 (Dec. 1924), pp. 178–181. DOI: `10.1007/BF01327326`.

[2] A. Einstein. "Quantentheorie des einatomigen idealen Gases". In: *Sitzungsberichte der Preussischen Akademie der Wissenschaften* 22 (July 1924), pp. 261–267.

[3] A. Einstein. "Quantentheorie des einatomigen idealen Gases. Zweite Abhandlung". In: *Sitzungsberichte der Preussischen Akademie der Wissenschaften* 1 (Feb. 1925), pp. 3–14.

[4] K. B. Davis et al. "Bose-Einstein Condensation in a Gas of Sodium Atoms". In: *Phys. Rev. Lett.* 75 (Nov. 1995), pp. 3969–3973. DOI: `10.1103/PhysRevLett.75.3969`.

[5] M. H. Anderson et al. "Observation of Bose-Einstein Condensation in a Dilute Atomic Vapor". In: *Science* 269 (July 1995), pp. 198–201. DOI: `10.1126/science.269.5221.198`.

[6] I. Bloch, J. Dalibard, and W. Zwerger. "Many-body physics with ultracold gases". In: *Rev. Mod. Phys.* 80 (July 2008), pp. 885–964. DOI: `10.1103/RevModPhys.80.885`.

[7] S. Lloyd. "Universal Quantum Simulators". In: *Science* 273 (Aug. 1996), pp. 1073–1078. DOI: `10.1126/science.273.5278.1073`.

[8] I. Bloch, J. Dalibard, and S. Nascimbène. "Quantum simulations with ultracold quantum gases". In: *Nature Physics* 8 (Apr. 2012), pp. 267–276. DOI: `10.1038/nphys2259`.

[9] O. Zobay and B. M. Garraway. "Two-Dimensional Atom Trapping in Field-Induced Adiabatic Potentials". In: *Phys. Rev. Lett.* 86 (Feb. 2001), pp. 1195–1198. DOI: `10.1103/PhysRevLett.86.1195`.

[10] D.C. Aveline et al. "Observation of Bose–Einstein condensates in an Earth-orbiting research lab". In: *Nature* 582 (June 2020), pp. 193–197. DOI: `10.1038/s41586-020-2346-1`.

[11] R. A. Carollo et al. "Observation of ultracold atomic bubbles in orbital microgravity". In: *Nature* 606 (May 2022), pp. 281–286. DOI: `10.1038/s41586-022-04639-8`.

[12] N. Lundblad et al. "Perspective on quantum bubbles in microgravity". In: *Quantum Science and Technology* 8 (Feb. 2023), p. 024003. DOI: `10.1088/2058-9565/acb1cf`.

[13] K. Frye et al. "The Bose-Einstein Condensate and Cold Atom Laboratory". In: *EPJ Quantum Technology* 8 (Jan. 2021). DOI: `10.1140/epjqt/s40507-020-00090-8`.

[14] T. van Zoest et al. "Bose-Einstein Condensation in Microgravity". In: *Science* 328 (June 2010), pp. 1540–1543. DOI: `10.1126/science.1189164`.

[15] D. Becker et al. "Space-borne Bose–Einstein condensation for precision interferometry". In: *Nature* 562 (Oct. 2018), pp. 391–395. DOI: `10.1038/s41586-018-0605-1`.

[16] Y. Guo et al. "Expansion of a quantum gas in a shell trap". In: *New Journal of Physics* 24 (Oct. 2022), p. 093040. DOI: `10.1088/1367-2630/ac919f`.

[17] A. Tononi and L. Salasnich. "Bose-Einstein Condensation on the Surface of a Sphere". In: *Phys. Rev. Lett.* 123 (Oct. 2019), p. 160403. DOI: `10.1103/PhysRevLett.123.160403`.

[18] L. Bereta S. J.and Madeira, V. S. Bagnato, and M. A. Caracanhas. "Bose–Einstein condensation in spherically symmetric traps". In: *American Journal of Physics* 87 (Nov. 2019), pp. 924–934. DOI: `10.1119/1.5125092`.

[19] A. Tononi, F. Cinti, and L. Salasnich. "Quantum Bubbles in Microgravity". In: *Phys. Rev. Lett.* 125 (June 2020), p. 010402. DOI: `10.1103/PhysRevLett.125.010402`.

[20] B. Rhyno et al. "Thermodynamics in expanding shell-shaped Bose-Einstein condensates". In: *Phys. Rev. A* 104 (Dec. 2021), p. 063310. DOI: `10.1103/PhysRevA.104.063310`.

[21] A. Tononi. "Scattering theory and equation of state of a spherical two-dimensional Bose gas". In: *Phys. Rev. A* 105 (Feb. 2022), p. 023324. DOI: `10.1103/PhysRevA.105.023324`.

[22] A. C. White. "Triangular vortex lattices and giant vortices in rotating bubble Bose-Einstein condensates". In: *Phys. Rev. A* 109 (Jan. 2024), p. 013301. DOI: `10.1103/PhysRevA.109.013301`.

[23] Y. Xiong and X. Yu. "Hydrodynamics of quantum vortices on a closed surface". In: *Phys. Rev. Res.* 6 (Feb. 2024), p. 013133. DOI: `10.1103/PhysRevResearch.6.013133`.

[24] A. Tononi and L. Salasnich. "Shell-shaped atomic gases". In: *Physics Reports* 1072 (June 2024). Shell-shaped atomic gases, pp. 1–48. DOI: `https://doi.org/10.1016/j.physrep.2024.04.004`.

[25] J.R. Driscoll and D.M. Healy. "Computing Fourier Transforms and Convolutions on the 2-Sphere". In: *Advances in Applied Mathematics* 15 (1994), pp. 202–250. DOI: `https://doi.org/10.1006/aama.1994.1008`.

[26] N. N. Bogoliubov. "On the Theory of Superfluidity". In: *Izv. Akad. Nauk. USSR 11* (1947), pp. 77–90.

[27] E. P. Gross. "Structure of a quantized vortex in boson systems". In: *Il Nuovo Cimento* 20 (May 1961), pp. 454–477. DOI: `10.1007/BF02731494`.

[28] L. P. Pitaevskii. "Vortex Lines in an Imperfect Bose Gas". In: *Sov. Phys. JETP* 13 (Feb. 1961), pp. 451–454.

[29] A. Tononi, L. Salasnich, and A. Yakimenko. "Quantum vortices in curved geometries". In: *AVS Quantum Science* 6 (Aug. 2024), p. 030502. DOI: `10.1116/5.0211426`.

[30] M. Schick. "Two-Dimensional System of Hard-Core Bosons". In: *Phys. Rev. A* 3 (Mar. 1971), pp. 1067–1073. DOI: `10.1103/PhysRevA.3.1067`.

[31] G. Bighin and L. Salasnich. "Finite-temperature quantum fluctuations in two-dimensional Fermi superfluids". In: *Physical Review B* 93 (Jan. 2016), p. 014519. DOI: `10.1103/physrevb.93.014519`.

[32] D. R. Nelson and J. M. Kosterlitz. "Universal Jump in the Superfluid Density of Two-Dimensional Superfluids". In: *Phys. Rev. Lett.* 39 (Nov. 1977), pp. 1201–1205. DOI: `10.1103/PhysRevLett.39.1201`.

[33] P. Cladé et al. "Observation of a 2D Bose Gas: From Thermal to Quasicondensate to Superfluid". In: *Phys. Rev. Lett.* 102 (Apr. 2009), p. 170401. DOI: `10.1103/PhysRevLett.102.170401`.

[34] J. Zhang and T.-L. Ho. “Potential scattering on a spherical surface”. In: *Journal of Physics B: Atomic, Molecular and Optical Physics* 51 (May 2018), p. 115301. DOI: `10.1088/1361-6455/aabc34`.

[35] J. W. Cooley and J. W. Tukey. “An algorithm for the machine calculation of complex Fourier series”. In: *Mathematics of Computation* 19 (1965), pp. 297–301. DOI: `https://doi.org/10.1090/S0025-5718-1965-0178586-1`.

[36] M. A. Wieczorek and M. Meschede. “SHTools: Tools for Working with Spherical Harmonics”. In: *Geochemistry, Geophysics, Geosystems* 19 (2018), pp. 2574–2592. DOI: `10.1029/2018GC007529`.

[37] J. P. Boyd. *Chebyshev and Fourier Spectral Methods.* Second Edition. Dover Books on Mathematics. Mineola, NY: Dover Publications, 2001. ISBN: 9780486411835.

[38] J. A. C. Weideman and B. M. Herbst. “Split-Step Methods for the Solution of the Nonlinear Schrödinger Equation”. In: *SIAM Journal on Numerical Analysis* 23 (June 1986), pp. 485–507. DOI: `10.1137/0723033`.

[39] R.P. Feynman. “Chapter II Application of Quantum Mechanics to Liquid Helium”. In: *Progress in Low Temperature Physics.* Ed. by C.J. Gorter. Vol. 1. Elsevier, 1955, pp. 17–53. DOI: `10.1016/S0079-6417(08)60077-3`.

[40] R. G. Lyons. *Understanding Digital Signal Processing.* Third Edition. Pearson Education International, 2010. ISBN: 9780132119375.

[41] N. G. Berloff. “Padé approximations of solitary wave solutions of the Gross–Pitaevskii equation”. In: *Journal of Physics A: Mathematical and General* 37 (Jan. 2004), pp. 1617–1632. DOI: `10.1088/0305-4470/37/5/011`.

[42] K. Padavić et al. “Vortex-antivortex physics in shell-shaped Bose-Einstein condensates”. In: *Physical Review A* 102 (Oct. 2020). DOI: `10.1103/physreva.102.043305`.

[43] H. Lewy, K. Friedrichs, and R. Courant. “Über die partiellen Differenzengleichungen der mathematischen Physik”. In: *Mathematische Annalen* 100 (1928), pp. 32–74. DOI: `10.1007/BF01448839`.

[44] S. A. Orszag. “On the Elimination of Aliasing in Finite-Difference Schemes by Filtering High-Wavenumber Components”. In: *Journal of Atmospheric Sciences* 28 (1971), p. 1074. DOI: `10.1175/1520-0469(1971)028<1074:OTEOAI>2.0.CO;2`.

[45] A. Arakawa. “Computational design for long-term numerical integration of the equations of fluid motion: Two-dimensional incompressible flow. Part I”. In: *Journal of Computational Physics* 1 (1966), pp. 119–143. DOI: `https://doi.org/10.1016/0021-9991(66)90015-5`.

[46] P. D. Sardeshmukh and B. I. Hoskins. “Spatial Smoothing on the Sphere”. In: *Monthly Weather Review* 112 (1984), pp. 2524–2529. DOI: `10.1175/1520-0493(1984)112<2524:SSOTS>2.0.CO;2`.

[47] N. R. Cooper, N. K. Wilkin, and J. M. F. Gunn. “Quantum Phases of Vortices in Rotating Bose-Einstein Condensates”. In: *Phys. Rev. Lett.* 87 (Aug. 2001), p. 120405. DOI: `10.1103/PhysRevLett.87.120405`.

[48] R. Doran and T. P. Billam. “Numerical method for the projected Gross-Pitaevskii equation in an infinite rotating two-dimensional Bose gas”. In: *Phys. Rev. E* 102 (Sept. 2020), p. 033309. DOI: `10.1103/PhysRevE.102.033309`.

[49] S. K. Adhikari. “Vortex-lattice in a uniform Bose–Einstein condensate in a box trap”. In: *Journal of Physics: Condensed Matter* (Apr. 2019), p. 275401. DOI: `10.1088/1361-648X/ab14c5`.

[50] D. J. Korteweg and G. de Vries. “On the Change of Form of Long Waves Advancing in a Rectangular Canal and a New Type of Long Stationary Waves”. In: *The London, Edinburgh, and Dublin Philosophical Magazine and Journal of Science* 39 (1895), pp. 422–443. DOI: `10.1080/14786449508620739`.

[51] V. E. Zakharov and A. B. Shabat. “Exact Theory of Two-dimensional Self-focusing and One-dimensional Self-modulation of Waves in Nonlinear Media”. In: *Soviet Journal of Experimental and Theoretical Physics* 34 (Jan. 1972), pp. 62–69.

[52] T. Tsuzuki. “Nonlinear waves in the Pitaevskii-Gross equation”. In: *Journal of Low Temperature Physics* 4 (Apr. 1971), pp. 441–457. DOI: `10.1007/BF00628744`.

[53] L. Pitaevskii and S. Stringari. *Bose-Einstein Condensation and Superfluidity.* Oxford University Press, 2016. ISBN: 978 0 19 875888 4.

[54] L. Khaykovich et al. “Formation of a Matter-Wave Bright Soliton”. In: *Science* 296 (2002), pp. 1290–1293. DOI: `10.1126/science.1071021`.

[55] K. E. Strecker et al. “Formation and propagation of matter-wave soliton trains”. In: *Nature* 417 (2002), pp. 150–153. DOI: `10.1038/nature747`.

[56] L. D. Carr et al. “Dark-soliton creation in Bose-Einstein condensates”. In: *Phys. Rev. A* 63 (Apr. 2001), p. 051601. DOI: `10.1103/PhysRevA.63.051601`.

[57] S. Burger et al. “Dark Solitons in Bose-Einstein Condensates”. In: *Phys. Rev. Lett.* 83 (Dec. 1999), pp. 5198–5201. DOI: `10.1103/PhysRevLett.83.5198`.

[58] C. A. Jones and P. H. Roberts. “Motions in a Bose condensate: IV. Axisymmetric solitary waves”. In: *Journal of Physics A* 15 (Aug. 1982), pp. 2599–2619. DOI: `10.1088/0305-4470/15/8/036`.

[59] B. P. Anderson et al. “Watching Dark Solitons Decay into Vortex Rings in a Bose-Einstein Condensate”. In: *Phys. Rev. Lett.* 86 (Apr. 2001), pp. 2926–2929. DOI: `10.1103/PhysRevLett.86.2926`.

[60] Y. S. Kivshar and D. E. Pelinovsky. “Self-focusing and transverse instabilities of solitary waves”. In: *Physics Reports* 331 (June 2000), pp. 117–195. DOI: `https://doi.org/10.1016/S0370-1573(99)00106-4`.

[61] C. A. Jones, S. J. Putterman, and P. H. Roberts. “Motions in a Bose condensate. V. Stability of solitary wave solutions of non-linear Schrodinger equations in two and three dimensions”. In: *Journal of Physics A: Mathematical and General* 19 (Oct. 1986), pp. 2991–3011. DOI: `10.1088/0305-4470/19/15/023`.

[62] N. Meyer et al. “Observation of Two-Dimensional Localized Jones-Roberts Solitons in Bose-Einstein Condensates”. In: *Phys. Rev. Lett.* 119 (Oct. 2017), p. 150403. DOI: `10.1103/PhysRevLett.119.150403`.

[63] M. Baker-Rasooli et al. “Observation of Jones-Roberts solitons in a paraxial quantum fluid of light”. Unpublished. Jan. 2025. URL: `https://arxiv.org/abs/2501.08383`.

[64] H. A. van der Vorst. “Bi-CGSTAB: A Fast and Smoothly Converging Variant of Bi-CG for the Solution of Nonsymmetric Linear Systems”. In: *SIAM Journal on Scientific and Statistical Computing* 13 (1992), pp. 631–644. DOI: `10.1137/0913035`.

[65] Y. Saad and M. H. Schultz. “GMRES: A Generalized Minimal Residual Algorithm for Solving Nonsymmetric Linear Systems”. In: *SIAM Journal on Scientific and Statistical Computing* 7 (1986), pp. 856–869. DOI: `10.1137/0907058`.

[66] L. S. Tuckerman, J. Langham, and A. Willis. “Order-of-Magnitude Speedup for Steady States and Traveling Waves via Stokes Preconditioning in Channelflow and Openpipeflow”. In: *Computational Modelling of Bifurcations and Instabilities in Fluid Dynamics*. Ed. by Alexander Gelfgat. Springer International Publishing, 2019, pp. 3–31. ISBN: 978-3-319-91494-7. DOI: `10.1007/978-3-319-91494-7_1`.

[67] L. S. Tuckerman. “Computational Challenges of Nonlinear Systems”. In: *Emerging Frontiers in Nonlinear Science*. Ed. by P. G. Kevrekidis, J. Cuevas-Maraver, and A. Saxena. Springer International Publishing, 2020, pp. 249–277. ISBN: 978-3-030-44992-6. DOI: `10.1007/978-3-030-44992-6_11`.

[68] A. H. Baker, E. R. Jessup, and T. Manteuffel. “A Technique for Accelerating the Convergence of Restarted GMRES”. In: *SIAM Journal on Matrix Analysis and Applications* 26 (2005), pp. 962–984. DOI: `10.1137/S0895479803422014`.

[69] M. L. Parks et al. “Recycling Krylov Subspaces for Sequences of Linear Systems”. In: *SIAM Journal on Scientific Computing* 28 (2006), pp. 1651–1674. DOI: `10.1137/040607277`.

[70] P. Gravejat. “A non-existence result for supersonic travelling waves in the Gross-Pitaevskii equation”. In: *Communications in Mathematical Physics* 243 (Nov. 2003), pp. 93–103. DOI: `10.1007/s00220-003-0961-y`.

[71] B. B. Kadomtsev and V. I. Petviashvili. “On the Stability of Solitary Waves in Weakly Dispersing Media”. In: *Doklady Akademii Nauk SSSR* 15 (Dec. 1970), pp. 753–75.

[72] S.V. Manakov et al. "Two-dimensional solitons of the Kadomtsev-Petviashvili equation and their interaction". In: *Physics Letters A* 63 (1977), pp. 205–206. DOI: `https://doi.org/10.1016/0375-9601(77)90875-1`.

[73] Y. Liu et al. "From KP-I lump solution to travelling waves of Gross-Pitaevskii equation". Unpublished. Oct. 2021. URL: `https://arxiv.org/abs/2110.15472`.

[74] A.A Minzoni and N.F Smyth. "Evolution of lump solutions for the KP equation". In: *Wave Motion* 24 (Nov. 1996), pp. 291–305. DOI: `https://doi.org/10.1016/S0165-2125(96)00023-6`.

[75] W.-X. Ma. "Lump solutions to the Kadomtsev–Petviashvili equation". In: *Physics Letters A* 379 (Sept. 2015), pp. 1975–1978. DOI: `https://doi.org/10.1016/j.physleta.2015.06.061`.

[76] V.M. Malkin and E.G. Shapiro. "Elementary excitations for solitons of the nonlinear Schrödinger equation". In: *Physica D: Nonlinear Phenomena* 53 (Oct. 1991), pp. 25–32. DOI: `10.1016/0167-2789(91)90161-2`.

[77] H. Terças, J. P. A. Martins, and J. T. Mendonça. "Rossby waves in rapidly rotating Bose–Einstein condensates". In: *New Journal of Physics* 12 (Sept. 2010), p. 093001. DOI: `10.1088/1367-2630/12/9/093001`.

[78] H. Saito and M. Hayashi. "Rossby–Haurwitz Wave in a Rotating Bubble-Shaped Bose–Einstein Condensate". In: *Journal of the Physical Society of Japan* 92 (Mar. 2023), p. 044003. DOI: `10.7566/JPSJ.92.044003`.

[79] M. Arazo, R. Mayol, and M. Guilleumas. "Shell-shaped condensates with gravitational sag: contact and dipolar interactions". In: *New Journal of Physics* 23 (Nov. 2021), p. 113040. DOI: `10.1088/1367-2630/ac37c9`.

[80] J. Sánchez-Baena, R. Bombín, and J. Boronat. "Ring solids and supersolids in spherical shell-shaped dipolar Bose-Einstein condensates". In: *Phys. Rev. Res.* 6 (July 2024), p. 033116. DOI: `10.1103/PhysRevResearch.6.033116`.

Appendices

A

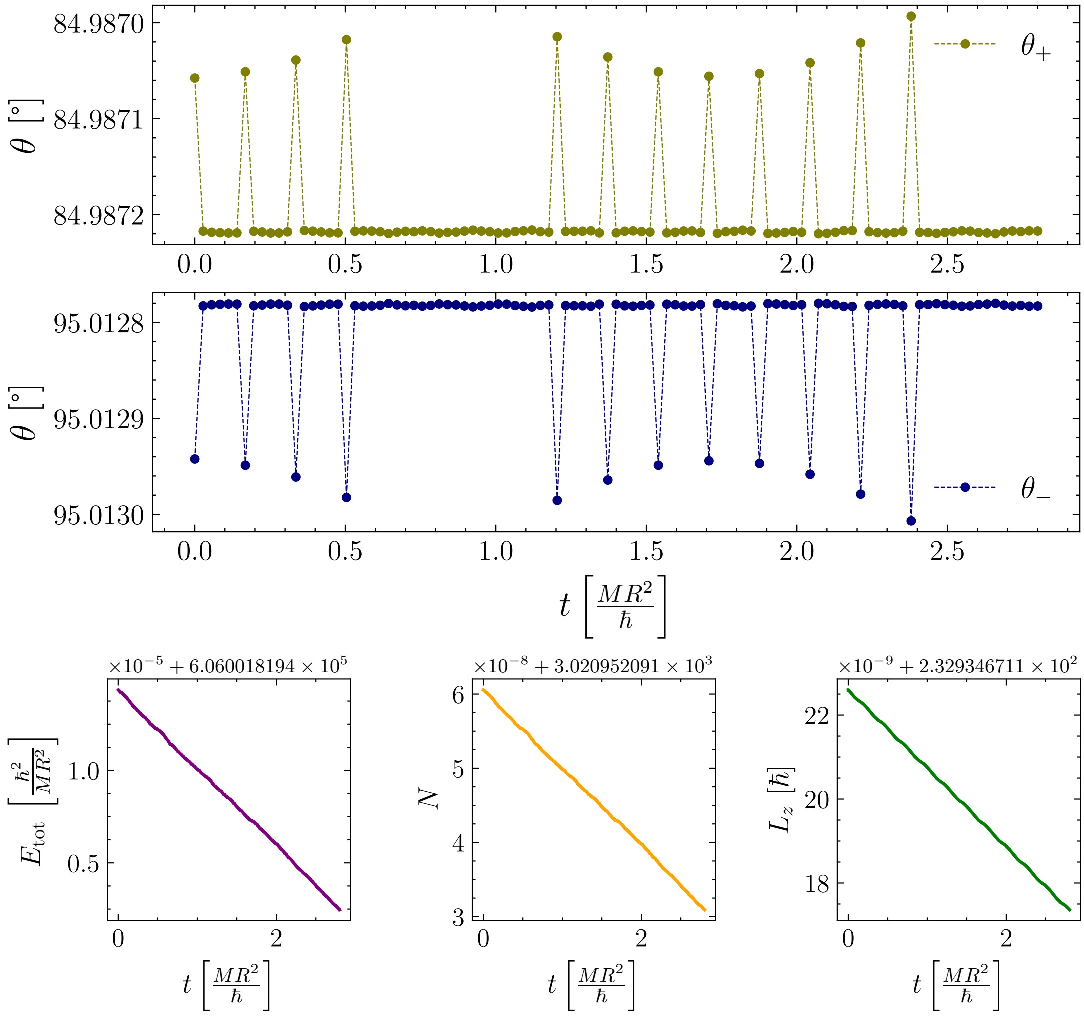

Figure A.1: Time evolution of a JRSW solution for $\tilde{\omega} = -2.2$ and $\tilde{\mu} = 50$. The two top panels show the polar angle of the vortex (in olive) and antivortex (in purple) as a function of time. The three panels in the bottom show the total energy, the particle number and the angular momentum of the wave function.

B

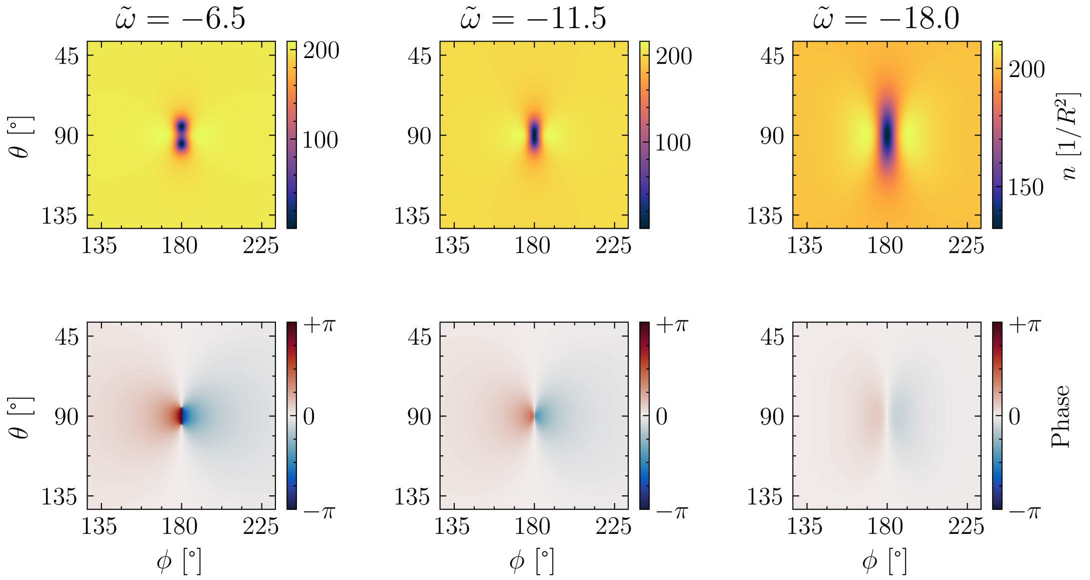

Figure B.1: JRSW solutions for $\tilde{\mu} = 333$ and decreasing $\tilde{\omega}$. The top panels show the density and the bottom panels the phase of the respective wave function in a region around the disturbance.

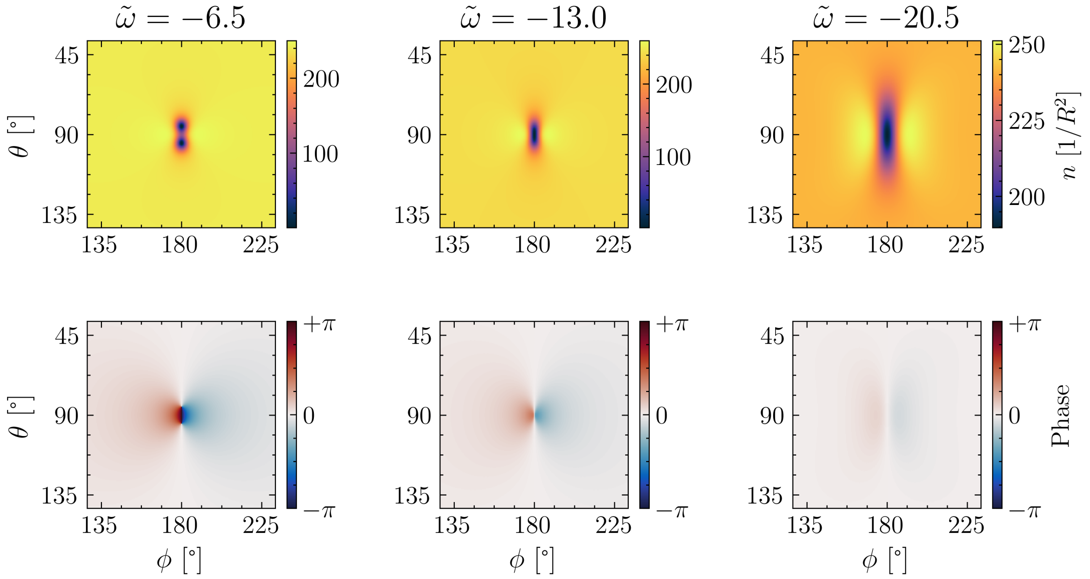

Figure B.2: JRSW solutions for $\tilde{\mu} = 400$ and decreasing $\tilde{\omega}$. The top panels show the density and the bottom panels the phase of the respective wave function in a region around the disturbance.

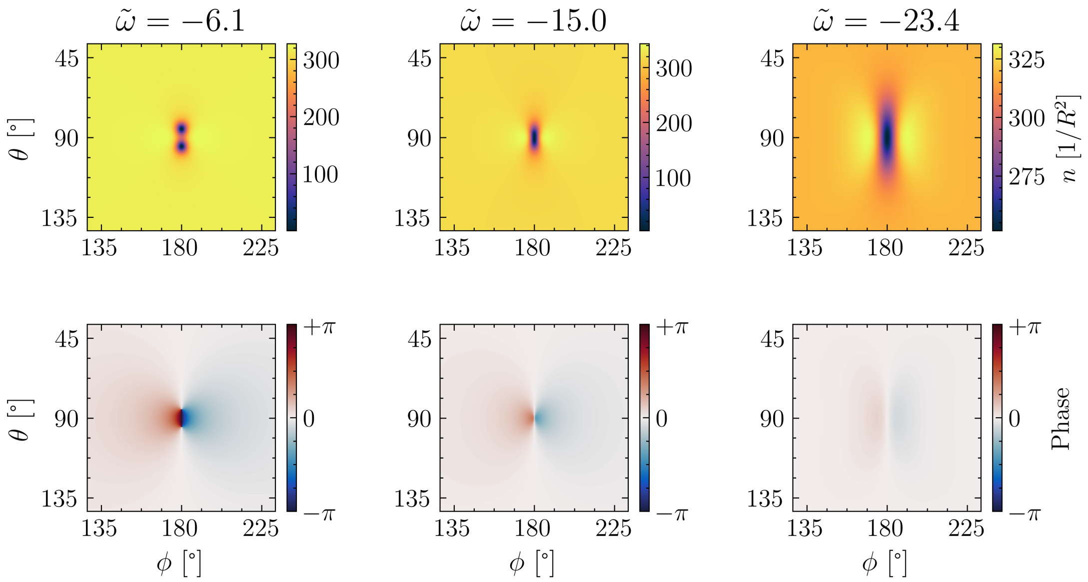

Figure B.3: JRSW solutions for $\tilde{\mu} = 529$ and decreasing $\tilde{\omega}$. The top panels show the density and the bottom panels the phase of the respective wave function in a region around the disturbance.

C

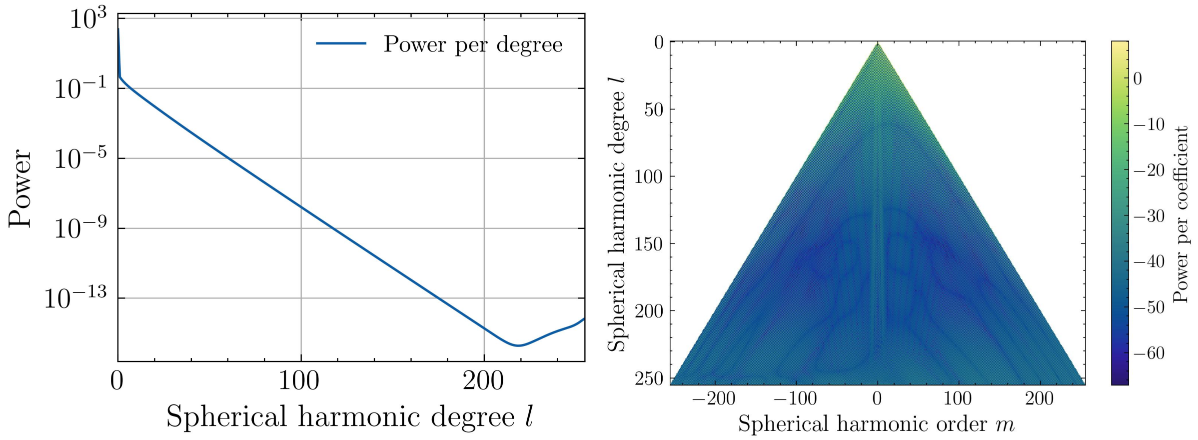

Figure C.1: Line spectrum and 2D Spectrum of a JRSW solution for $\tilde{\mu} = 400$ and $\tilde{\omega} = -15.1$.

Acknowledgments

First and foremost, I would like to thank my two supervisors, Thomas Gasenzer and Davide Proment, for providing me the opportunity to work on this project. I am very grateful for the constant stream of encouraging and motivating advice, fresh ideas when I was stuck, a wealth of technical knowledge and the physical intuition to categorize my findings. My own understanding of the underlying physics has grown immensely during the project and it would not have been possible without them. Furthermore, I would like to thank Alberto Villois for many fruitful discussions and especially his expertise on the Newton-Raphson method and surrounding numerics. I am thankful to Davide and Alberto for kindly inviting me to spend a week at the University of East Anglia in beautiful Norwich to intensify our collaboration.

I must thank Dominik Schramm, Georg Trautmann and Rasmus Kauffeld for helping me during the reviewing process of the thesis. My gratitude goes out to all my friends who have supported me through this endeavor and who have listened to my grievances, especially my roommate Elizabeth for her willingness to hang out on so many evenings with me. I truly appreciate all those who were there for me and despite reoccurring hardships, I greatly enjoyed the research process, the coding, the discussions that eventually led to this thesis.

Erklärung

Hiermit versichere ich, dass ich die vorliegende Arbeit selbstständig verfasst und keine anderen als die von mir angegebenen Quellen als Hilfsmittel benutzt habe.

Heidelberg, 25/05/25

Ort, Datum

Unterschrift